

Spectral decomposition of hot subdwarf binaries

Masterarbeit aus der Physik

vorgelegt von

Simon Kreuzer

am 29.04.2016

Dr. Remeis Sternwarte Bamberg
Friedrich-Alexander-Universität Erlangen-Nürnberg



Betreuer: Prof. Dr. Ulrich Heber

Contents

1	Introduction	1
1.1	Stellar spectra	1
1.1.1	The black body approximation	1
1.1.2	Spectral lines	2
1.1.3	Modification of the stratification of spectral lines	3
1.2	The nature of hot subdwarf stars	4
1.2.1	The importance of hot subdwarfs	4
1.2.2	Classification and observations	6
1.2.2.1	Spectra	6
1.2.2.2	Kiel diagram	6
1.2.3	The evolution of hot subdwarf stars	7
1.2.4	How to form hot subdwarfs	9
1.2.4.1	Interacting binary evolution	9
1.2.4.2	Single star evolution	10
1.3	Hot subdwarfs in binaries	11
1.3.1	Close binaries	11
1.3.2	Wide binaries with composite spectra	12
1.3.3	Composite spectra	13
1.4	The Sloan Digital Sky survey	16
2	The procedure	19
2.1	Project Outline	19
2.2	Spectral libraries	20
2.2.1	non-LTE <i>TLUSTY/SYNSPEC</i> subdwarf grid	21
2.2.2	<i>PHOENIX</i> library	21
2.3	Interpolation in spectral grids	22
2.4	Convolution	25
2.5	Core - Fit algorithm	26
2.5.1	Function minimization	26
2.5.2	Free parameters and physical constraints	26
2.5.3	Downhill Simplex	28
2.5.3.1	Function minimization using the simplex algorithm	28
2.5.3.2	Advantages and disadvantages of the simplex method	31
2.6	Uncertainties	32
2.6.1	χ^2 statistics	32

2.6.2	Determination of the uncertainties	33
2.7	Interstellar extinction and reddening	34
2.8	Technical implementation	37
2.8.1	Spectral grids and memory management	37
2.8.2	Numerical convolution	39
2.8.3	Boundaries of the spectral grid	39
3	Proof of concept	41
3.1	Convolving 2 Gaussians	41
3.2	Convolving spectral lines	42
3.3	Error estimation based on synthetic spectra with artificial S/N	43
3.3.1	Example 1	44
3.3.2	Example 2	48
3.4	Correlations	53
4	Applications	56
4.1	Testcase PG1104+243	56
4.1.1	The Object	56
4.1.2	Spectral Fitting	57
4.2	Stars from the HVS sample	59
4.2.1	The Objects	59
4.2.2	Spectral Fitting	60
4.2.3	Comparison with stellar evolution predictions	64
5	Outlook and Conclusion	70
5.1	Outlook and possible improvements	70
5.1.1	Solving the log g degeneracy problem	70
5.1.2	Genetic algorithm	71
5.1.3	Extended LTE grid for the hot subdwarfs	71
5.1.4	Other possible improvements	73
5.2	Conclusion	73
A	C++ Code	76
A.1	Downhill Simplex Algorithm - The code	76
A.2	Numerical convolution	79
A.3	Golden section search	82
B	Data Analysis	85
B.1	Fit in χ^2 line for Example 1	85
B.2	χ^2 lines of Example 2 for S/N = 75	86
B.3	χ^2 line of candidate SDSS J135057+080110	87

B.4 Spectral Fits	88
List of Tables	95
References	96
Acknowledgements	99
Erklärung	101

Abstract

Binaries consisting of a hot subdwarf and a F/G/K-type main-sequence companion are important to understand the outcome of interacting binary evolution. They show composite spectra and significant excess in the infrared. The spectral analysis is rendered difficult, because the contribution of both stars to the composite spectrum needs to be disentangled. To this end, a numerical code was developed which allows quantitative spectral analysis. Grids of standard stellar spectra for the F/G/K stars as well as a non-LTE subdwarf grid allow to decompose the spectrum of a binary system to be decomposed and hence find the contribution of each star to the combined flux. In order to obtain the best fitting combination of parameters of both stars a standard Chi-square fitting routine is used. The analysis reveals T_{eff} , $\log g$, the helium abundance of the subdwarf and T_{eff} , $\log g$, the metal abundance of the cool companion. Reddening due to interstellar extinction is also taken into account. In order to test the code, it is applied to sets of mock spectra. Quantitative analyses of 5 stars using SDSS and BOSS spectra are carried out. Finally, the high-resolution spectrum of PG1104+243 was analyzed. The long-term goal is to study technical possibilities in the quantitative spectroscopy of multiple-star systems and the development of fast method for their decomposition.

1 Introduction

1.1 Stellar spectra

This work deals with the analysis of binary spectra. Therefore, it is worth to have a close look at the characteristics of stellar spectra in general first. This section describes the fundamental properties as well as the influence of physical parameters on the spectra of stars.

1.1.1 The black body approximation

The shape of the spectrum of a single star can crudely be approximated by the energy distribution of a black body. In the wavelength representation, its well known shape is given by Planck's law, which can be written in the wavelength representation

$$u_{\lambda}(\lambda, T) = \frac{2hc^2}{\lambda^5} \frac{1}{e^{hc/\lambda kT} - 1} \quad (1.1)$$

where u_{λ} is the spectral radiance i.e. the power emitted per emitting area per solid angle and per unit wavelength. Derivating Eq. 1.1 with respect to λ and evaluating the resulting expression to be equal zero yields the wavelength of the emission maximum λ_{max} . The result is called Wien's displacement law.

$$\lambda_{max} = \frac{2897.8 \mu\text{m} \cdot K}{T} \quad (1.2)$$

For higher temperatures, the emission maximum in wavelength space shifts towards shorter wavelengths and therefore higher energies. In order to get a feeling for the shape and the shift of the maximum Fig. 1.1 illustrates black body radiation curves for different temperatures. For hot

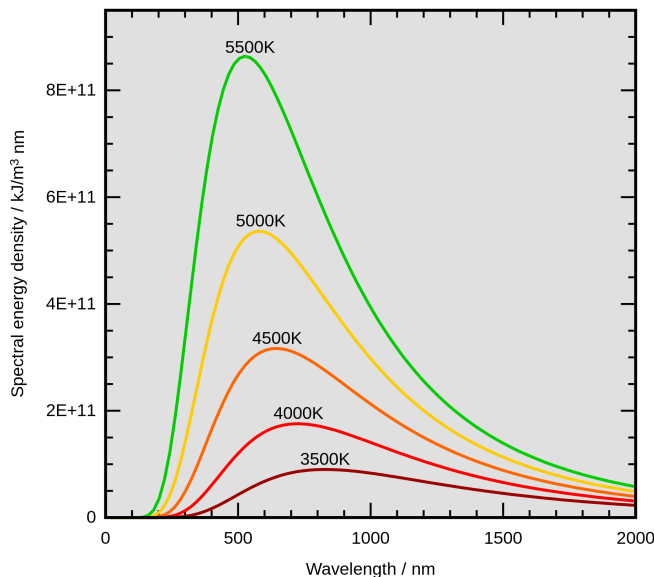


Figure 1.1: u_{λ} plotted for different temperatures to illustrate the shift of the emission maximum in wavelength space according to Wien's law. From en.wikipedia.org.

stars, the optical spectrum lies in the descending part at higher wavelengths than the maximum. In this region the Rayleigh-Jeans approximation of Eq. 1.1

$$u_{\lambda}(\lambda, T) = \frac{2ckT}{\lambda^4} \quad (1.3)$$

describes the shape of the black body spectrum. However, in stars the slope of the continuum is dominated by the Paschen continuum, which changes the shape to be $\propto \frac{1}{\lambda^3}$. Radiation transport in the star modifies it even further.

In the context of stars, we gain the knowledge that the rough shape of the stellar spectrum itself, including the position of the emission maximum, is a good indicator for temperature estimation, which is one of the most fundamental parameters to be derived in spectral analysis.

Furthermore, the continuum of a stellar spectrum can be modified by interstellar matter (ISM) in the line of sight to the star. Since absorption in the ISM increases from the IR to the UV, the star appears to have an increasingly strong IR excess, as the column density of ISM in the line of sight increases. This effect, simply called *interstellar reddening*, is described in more detail in Sec. 2.7.

1.1.2 Spectral lines

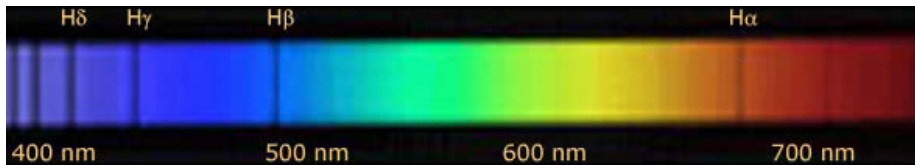


Figure 1.2: Low resolution spectrum of Vega, illustrating the drop in intensity at specific wavelengths. The most prominent lines are the Balmer lines of the hydrogen atom. From <http://www.kcvs.ca/>.

Another feature visible in the spectrum of stars are spectral lines, typically in absorption. That means that at specific wavelengths the intensity drops as illustrated in Fig. 1.2. This is due to atoms being able to absorb photons at specific wavelengths - or energies. In these cases, transitions can be triggered in the atom resulting in a higher energy state. The new energy state is unstable. If the electron jumps again to a lower energy level, a photon of the same wavelength can be emitted again. The time scales of this process are on the order of $\sim 10^{-8}$ s. However, there may also be intermediate energy states allowing the atom to emit more than one photon with different energies at different times. These processes yield the atmosphere of a star to become non-transparent for wavelengths where absorption is possible and therefore, absorption lines are not 'refilled' again - they become observable. The energy of each transition and therefore the line wavelength is different for each element. Thus, analyzing spectral lines yields information about the composition of the star. Since the mean free path for photons in the stellar plasma of the kind of star under study is on the order of 200000 km or less, only the composition of the stellar atmosphere can be observed in the spectrum.

1.1.3 Modification of the stratification of spectral lines

Spectral lines appear to be not as sharp as the natural line width due to the finite lifetime of the excited state suggests. Three effects mainly increase the width of a spectral line.

The most significant broadening of spectral lines is due to thermal motion of the atoms in the stellar atmosphere. Hence, atoms have different velocities with respect to the observer and a particular emission wavelength appears to be smeared. This effect is called *Doppler broadening* and yields a broadening with a Gaussian profile which depends on temperature and atomic weight. In units of velocity, this effect typically yields a broadening on the order of

$$v_d = \sqrt{\frac{2kT}{m}} \approx 13 \left(\frac{T}{10^4\text{K}} \right)^{\frac{1}{2}} \text{ km s}^{-1} \quad (1.4)$$

Gravity and therefore the density of a star has also a direct influence on the shape of spectral lines. The more dense and compact the star, the higher the gravity $\log g$ on the surface. Due to the higher density, electric fields gain more strength. In the rapidly varying electric fields created by neighbouring electrons and ions, the emission lines of atoms are shifted and split up into different energies. This effect, called *Stark broadening*, is most visible in strong lines, for instance the Balmer series and strong helium lines. However, the splitting of lines due to the Stark effect is never observed because of the rapid and locally different changes of the electric field in orientation and strength. The emitted photons of one transition can be emitted at slightly different wavelength (they are red or blue shifted) and the line appears broadened. This effect is superimposed to the Doppler broadening and, hence, the lines visible in the spectrum of stars with higher surface gravity are further broadened. The Stark effect can be interpreted as the electromagnetic analogue to the Zeeman effect, which describes the splitting of spectral lines in magnetic fields. It can be used to determine the surface gravity and therefore the compactness of a star. The atmospheric broadening of a spectral line can be described by a *Voigt profile*, which is the convolution of a Gaussian and a Lorentzian profile where the latter one describes Stark broadening.

As a side note, gravity also affects the intensity of the Balmer jump. This is in general also dependent on the temperature and serves as a good cross-check.

Intrinsic rotation of the star also has an impact on the shape of spectral lines and yields *rotational broadening*. Observing a rotating star means, we see one half of the star approaching us while the other half of the star is receding. This range of regions with different radial velocities on the surface accumulates to broad spectral lines, which can - depending on the rotation velocity of the star - even dominate the Doppler broadening of its spectral lines. The functions which describe rotational broadening have a parabolic shape. They can be rather complex and also depend on other effects like limb darkening.

Of course, all three effects, atmospheric, rotational and Doppler broadening can occur in addition. However, since the shape of the broadening is different in each mechanism they can be distinguished from each other and decomposed using line fitting techniques.

1.2 The nature of hot subdwarf stars

Hot subdwarfs are a unique and somehow peculiar class of stellar objects. From a photometric point of view, hot subdwarfs are similar to typical O- or B-type dwarf stars, which are burning hydrogen on the main sequence. However, hot subdwarf (sdB, sdO) stars are fainter than typical dwarf stars and therefore named subluminoous. The first detection of these subluminoous objects was reported by Humason & Zwicky (1947) in a survey of the north Galactic pole region while looking for new white dwarf candidates. Many stars in their sample did not show the typical white dwarf features in their spectra, for instance wide but shallow absorption lines, but rather looked similar to normal O or B-type dwarfs - spectroscopically as well as in photometry. The estimated distances under the assumption that these objects are ordinary dwarf stars, exceeded 27 kpc. The puzzling mystery at observing these stars at high galactic latitudes was, that massive stars need dense gas clouds to form in. Star forming regions are mostly found in the Galactic disk and especially along the spiral arms. Ejecting stars from there up to high galactic latitudes and huge distances within their relatively short lifetime requires them to travel extremely fast. Since this extreme motion was not observed Humason & Zwicky (1947) concluded that these objects must be closer than expected and therefore fainter than dwarfs. When Greenstein & Sargent (1974) determined surface gravity and temperatures of 189 blue halo objects in the Galactic pole region, their place in the Hertzsprung Russel diagram (HRD) became clear (see Fig 1.3).

Note that hot subdwarfs must not be confused with the cool subdwarfs, another species of stars located directly below the main sequence. Cool subdwarfs are low metallicity main sequence stars, shifted to the blue part of the HRD. The lack of metals causes a lower opacity in the outer layers, decreasing the radiative pressure and therefore resulting in a somewhat bluer and more compact star than its normal metallicity sibling.

The cool subdwarf stars are hence core hydrogen burning stars, whereas hot subdwarfs burn helium, are located on the extreme end of the horizontal branch and are not associated to a somehow special main-sequence population. The extreme horizontal branch (EHB) furthermore divides into 2 different populations, sdB and sdO stars. Note, that most of the sdO stars have already evolved beyond the EHB and are on the white dwarf cooling sequence. The following section deals with their importance for astronomy in general and their special properties is discussed in Sec. 1.2.2.

1.2.1 The importance of hot subdwarfs

The hot subdwarf stars received public interest as Green et al. (1986) showed that this species of faint blue stars does not seem to be a rare occurrence. They found, that especially sdB stars are the most prominent class of objects in their sample of 1715 objects ($\sim 40\%$). sdO stars ($\sim 13\%$), compared to DA white dwarfs ($\sim 21\%$), also seem to be common. Note, that DA white dwarfs are white dwarfs with hydrogen dominated atmospheres, which make up the majority of all white dwarfs (Zhang et al., 2013).

The hot subdwarf population also seems to be a solution for the UV flux excess first observed

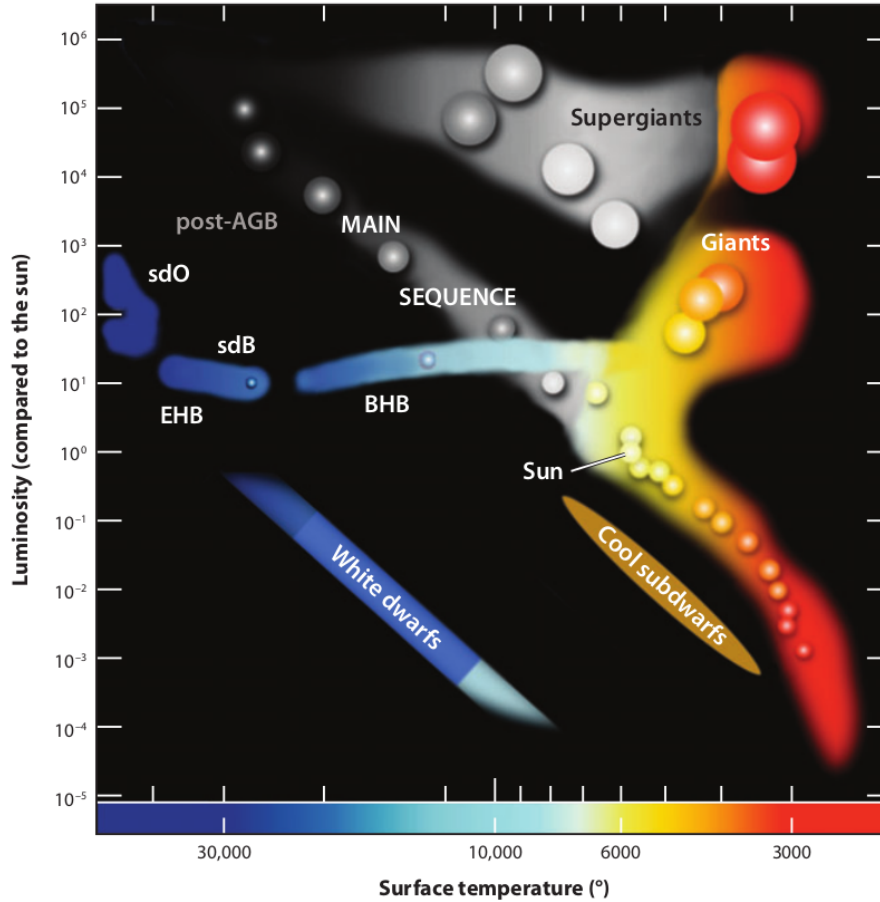


Figure 1.3: Hertzsprung Russell diagram (HRD), illustrating the position of the sdB and the sdO population. Note, that the nature of cool subdwarfs is completely different compared to the hot subdwarfs. Taken from Heber (2016).

in elliptical galaxies in 1969. Han et al. (2007) carried out evolutionary population synthesis and were able to explain the excess with an old population of helium burning stars, similar to the subdwarf population in our Galaxy. Podsiadlowski et al. (2008) have also shown that assuming a similar number density of these stars in elliptical galaxies is enough to explain the mysterious excess in the UV without other assumptions. This fact shows, that hot subdwarfs don't seem to be rare, but rather common.

However, the origin of hot subdwarfs is still wrapped in mystery, but during the last decades several scenarios have been investigated in detail and a consistent picture emerges. The fundamental question is the connection to stellar evolution: Which role do hot subdwarfs play? A major hint came from the identification of hot subdwarfs with helium burning stellar models. Heber & Hunger (1984) demonstrated the connection to the extended horizontal branch (HB) in the $T_{eff} - \log g$ -plane. This type of diagram is also known as the famous Kiel diagram (see Sec. 1.2.2.2).

1.2.2 Classification and observations

1.2.2.1 Spectra

A few attempts have been made to classify subdwarf stars in a way similar to the spectroscopic Morgan–Keenan (MK) classification of normal stars. The most detailed classification has been published by Drilling et al. (2013), but is not generally established in literature yet. They suggested to introduce a helium class, in addition to the spectral and luminosity classes known from the MK system. Details of the spectral classification are given in Tab. 1.1.

Type	Fine type	Luminosity class	Delimiter	Strength of He lines comp. to H
sdO/sdB	0-9.5	I-VIII	:	0-40
sdOC	1	VII	:	He40

Table 1.1: Spectral classification of hot subdwarfs, proposed by Drilling et al. (2013), the second row shows the ranges of the classification itself and the row line gives an example.

The spectral type is subdivided into sdO and sdB stars. An additional 'C' is appended, if the star is rich in carbon and a subtype is indicated by a number $0 < \text{subtype} < 10$, followed by a luminosity class and a delimiter ':'. Up to this point, everything is somewhat familiar, because the definition is very close to the MK system. Additional information about the He abundance is encoded in the last part. The number given there must be between 0 and 40 and is a measure for the line strength ratio of He lines compared to Balmer lines.

1.2.2.2 Kiel diagram

Classifying stars with the use of the HRD suffers one ambiguity: In order to derive the absolute luminosity of a star either the distance or the radius¹ of a star needs to be known. Especially when dealing with exotic objects, like hot subdwarfs, both parameters could in most cases not be measured directly. Only showing parameters which could be directly inferred from spectroscopy is a natural solution to this problem. Therefore, a new

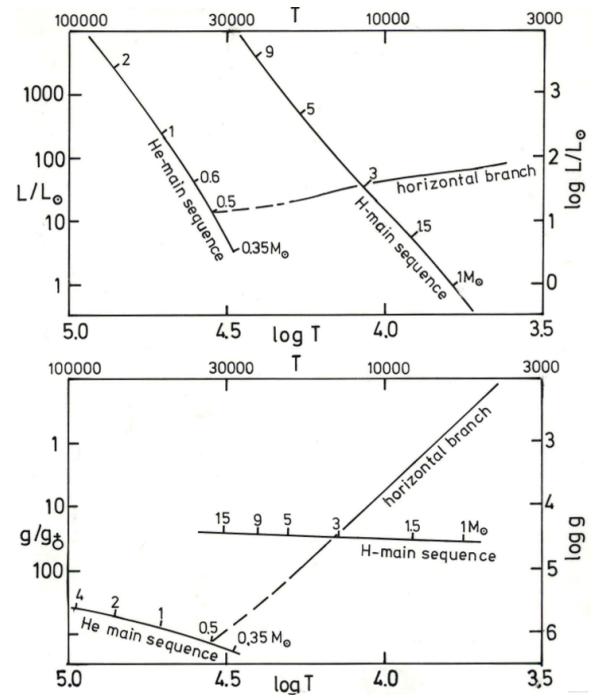


Figure 1.4: Comparison of the standard HRD (top) and the Kiel diagram (bottom), both showing the H and He main sequences and the horizontal branch, from Hunger & Heber (1987).

¹Since $L = 4\pi R^2 \cdot T_{eff}^4$, if the temperature is known for instance via spectroscopy, the absolute luminosity of a star could be determined, if its radius R is known e.g. if eclipses are observed.

diagram was introduced by Albrecht Unsöld², professor at the university of Kiel from 1932 to 1973, as spectroscopy evolved to quantitatively reliable results. The diagram was called *Kiel diagram* afterwards and shows the effective temperature T_{eff} versus the surface gravity $\log g$. It can be interpreted as an advanced or specialized version of the HRD, containing almost the same information. A graphical comparison between both diagrams is given in Fig. 1.4, which is taken von Hunger & Heber (1987). In this publication, a good discussion about the Kiel diagram in comparison to the HRD is given. An example of a sample of hot subdwarfs, plotted into a Kiel diagram is shown in Fig. 1.6.

1.2.3 The evolution of hot subdwarf stars

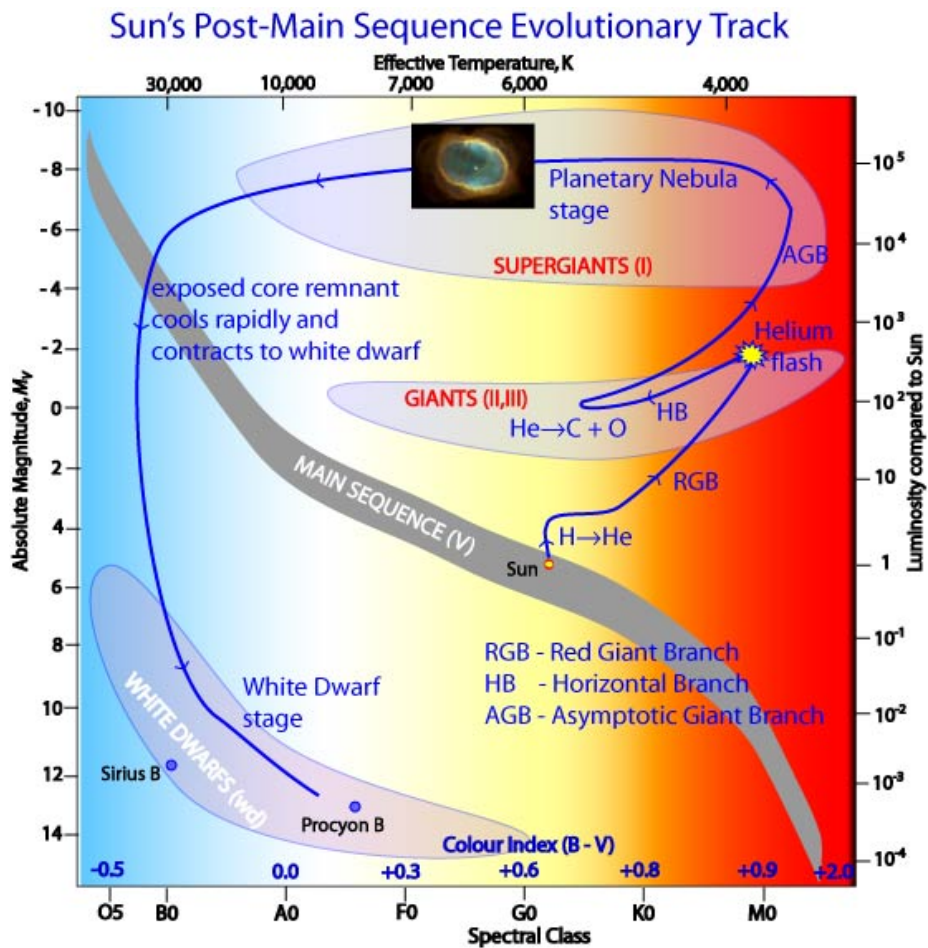


Figure 1.5: Stellar evolution according to the canonical picture for a $1 M_{\odot}$ star. Graphic taken from www.atnf.csiro.au/outreach//education/senior/astrophysics/images/stellarevolution/hrsunplannebwd.jpg.

²Albrecht Unsöld was one of the pioneers in quantitative spectroscopy of stars, considering quantum mechanical processes in their atmospheres; https://de.wikipedia.org/wiki/Albrecht_Unsöld, effective 19.01.2016

Canonical stellar evolution, as depicted in Fig. 1.5, suggests that intermediate mass stars, after their hydrogen burning phase on the main sequence, evolve to the top right corner of the HRD. Since the hydrogen burning shell moves outward and in the center of the star a helium core forms, the star expands with decreasing effective temperature, thus emitting more in the red part of the spectrum. This evolutionary status is called red giant phase and the corresponding position in the HRD is called *red giant branch* (RGB). Igniting the helium core under degenerate conditions results in a run-away process, called the helium flash. Afterwards the star settles again on a sequence which is called the *Horizontal branch* (HB) due to its orientation in the HRD (see Fig. 1.3). HB stars are powered by a helium burning core surrounded by a hydrogen burning shell. The core mass amongst HB stars is almost identical, since the helium flash occurs at the same core mass, irrespective of the total mass of the star for masses less than $2.3 M_{\odot}$. However, the masses of their hydrogen envelopes may differ, which explains the position of a particular helium burning star on the HB. Stars with less massive envelopes are found at the blue end of the EHB. As stated before, in the canonical picture, the star has now a helium burning core, surrounded by a hydrogen burning shell, causing a raise in luminosity and a shift to the red end of the HRD as the C/O core grows. This is called the asymptotic giant branch (AGB). At the extreme blue end of the HB, the EHB, the hydrogen envelope is far too thin to sustain H shell burning, which means that the star cannot undergo a standard AGB shell burning phase. The temperature of the star increases over time and it is entering the white dwarf cooling track, as HE burning terminates. According to Heber (2009) only very few complete calculations of evolutionary tracks are available. Especially the helium flash is not covered in most cases. Tracks covering the phase from the zero-age main sequence to the zero-age horizontal branch can be found in Serenelli & Weiss (2005). Post-EHB evolution tracks are depicted in Fig. 1.6.

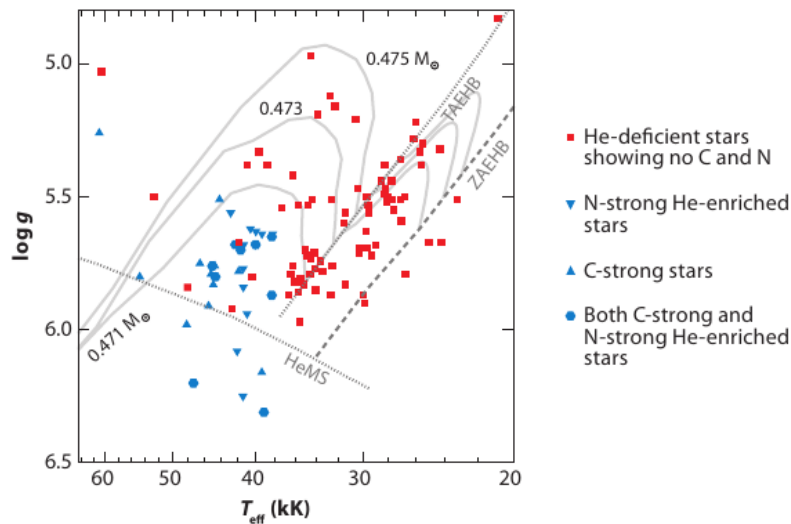


Figure 1.6: Sample of hot subdwarf sample from the Supernova Ia Progenitor Survey (SPY, Lisker et al. (2005), Stroeer et al. (2007)). Evolution tracks for different masses of hot subdwarfs computed by Dorman et al. (1993). Plot taken from Heber (2009).

1.2.4 How to form hot subdwarfs

Several scenarios have been proposed to explain the high mass loss of almost the complete hydrogen envelope. This process must have taken place prior or at the beginning of the core helium burning phase. Due to the high fraction of binaries amongst hot subdwarf stars, interactions with a companion are thought to be important for their formation. However, also single star scenarios have been proposed. These scenarios are discussed in Heber (2016) and will be summarized in the following.

1.2.4.1 Interacting binary evolution

As one star of a binary system comes close to the RGB, it expands significantly. In this evolutionary phase, it can fill its Roche lobe³ and therefore loose matter to its surrounding.

a) Common envelope phase If the mass loss rate is sufficiently high, a common envelope (CE) forms. Due to friction of both components with the gas in the CE, a spiral in takes place, causing the separation between both components to shrink. At the same time, orbital energy is transferred to the CE, yielding an ejection of the CE. The core of the former RGB star forms the subdwarf. The resulting periods are expected to be between 0.1 and 10 days. This scenario nicely explains the fraction of close binaries amongst subdwarfs (see Sec. 1.3.1). If the companion subsequently also reaches the RGB, a second CE phase can yield the formation of a sd + WD binary. Therefore, the existence of high mass companions is indeed expected. However, the physical processes occurring during the CE phase are poorly understood.

b) Roche lobe overflow If the mass loss rate is not high enough to form a CE, Roche lobe overflow (RLOF) is triggered. This means material is slowly transferred to the companion and then accreted. This scenario was first proposed by Webbink (1984). Binary population synthesis conducted by Chen et al. (2013) showed, that - if considering not only standard RLOF, but also atmospheric RLOF - long period binaries with periods up to 1100 days can evolve this way. However, there is a discrepancy, since periods ranging from 700 to 1300 days have been observed by Vos et al. (2012). If subsequent to the RLOF evolution, a CE phase takes place, sd + WD binaries can also form in this formation channel. A graphical overview concerning the outcomes of the CE and the RLOF channel is given in Fig. 1.7.

c) WD merger The orbits of two helium white dwarfs shrink in close binaries over time due to gravitational wave radiation. As it comes to a merger, they are thought to form a hot subdwarf star under special circumstances. Indeed, several progenitor systems are known up to now, which will merge in less than the Hubble time. This scenario could help to explain the existence of single subdwarfs. However, the drawback is that only a few of these systems are known up to now. They can not account for all single subdwarfs

³The Roche lobe describes the region around one component of a binary system, where material is still gravitationally bound to the star.

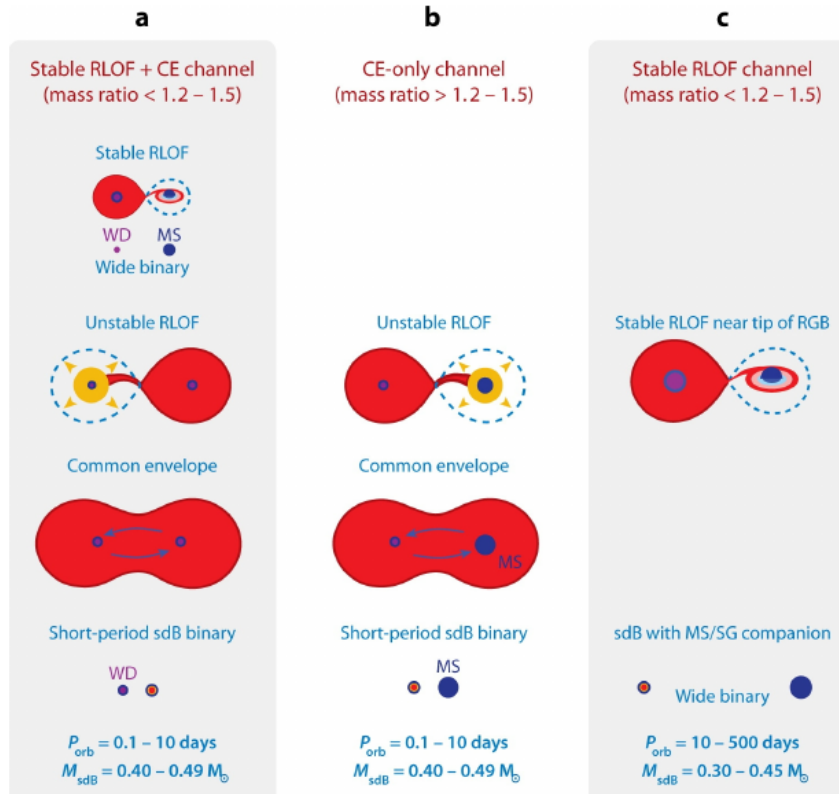


Figure 1.7: Schematic overview over different binary formation channels. a and b produce short period binaries, while c produces long period binaries.

observed. Furthermore, the mass range of the merger product is not restricted to the canonical mass of the subdwarfs, which is $0.48 M_{\odot}$. Unlike predicted by the merger scenario, masses derived from astroseismic analyses of pulsating hot subdwarfs are distributed in an extremely narrow range around this value.

1.2.4.2 Single star evolution

a) Helium mixing During the red giant phase the outer envelope is convective while the convection zone varies in depth during this phase. Convection of the outer envelope can reach as deep as the hydrogen burning shell, yielding helium to be mixed into the outer layers of the star. Hydrogen is transported down from the stellar envelope into deeper regions and is burnt there while the surface gets He enriched. However, usually there is no such deep penetration, because convection is inhibited by a barrier due to the different composition of the stellar layers. Special conditions are necessary to overcome this barrier. This scenario was investigated by Tailo et al. (2015). There are also some contradictions with theory, especially concerning the coupling of the different stellar layers (Heber, 2016). However, rapid rotation can help to solve them and different rotation rates of the hot subdwarf can explain different positions on the EHB.

b) The hot-flasher scenario Typically, the He core flash occurs at the tip of the RGB (see 1.2.3). However, Castellani & Castellani (1993) found that if enough mass is lost before reaching the tip of the RGB the He flash might occur later while the star is already on the way to the WD cooling sequence. Brown et al. (2001) found that the remnants of these so called hot flashers are located close to the extreme end of the HB. During the flash a convection zone evolves due to the high luminosity. This, again, leads to mixing. The exact evolution depends sensitively on when the He flash occurs. One typically distinguishes between the early and the late flashers. The general rule is that the later the flash occurs, the more He, N, and C can be observed in the atmosphere due to deeper mixing. N becomes visible in late flashers while C is only observable in the very late ones. See Miller Bertolami et al. (2008) for details and stellar evolution tracks.

1.3 Hot subdwarfs in binaries

A large fraction ($\sim 50\%$) of subdwarfs is found in binary systems, which is not surprising since the most plausible formation scenarios involve binary evolution. Observationally, there seem to be two different binary populations amongst subdwarfs. The binaries can either be very close ($P < 30$ d) or wide ($P \sim 1000$ d) with a gap between 30 and ~ 500 d. Both types of binaries will be discussed in the following.

1.3.1 Close binaries

As Maxted et al. (2001) found that almost 70 % of the sdB stars in their sample show radial velocity (RV) variability with periods less than 10 days, further RV surveys were triggered. For instance, Morales-Rueda et al. (2003) increased the sample of close sdB binaries with solved orbital parameters to 38 and Copperwheat et al. (2011) solved 18 new systems and provide radial velocity measurements of 108 further subdwarf stars. The most famous survey, the MUCHFUSS (Massive Unseen Companions to Hot Faint Underluminous Stars from SDSS) survey, revealed 1100 subdwarf candidates from the SDSS (Sloan Digital Sky Survey) of which 127 are RV variable⁴ In such close binaries, showing variability on scales down to hours, massive companions (white dwarf, neutron stars and black holes) can be expected (see Section 1.2.4.1). However, in the course of the MUCHFUSS project, Geier et al. (2015) did not find any neutron star or black hole companions, which constrained the fraction of H rich hot subdwarfs with massive companions to be less than 1.3 %. This is consistent with theoretical binary synthesis. (Yungelson et al. 2005; Geier et al. 2010; Nelemans 2010). Furthermore, most formation channels described in 1.2.4 are only possible in close binaries, making these close subdwarf systems plausible outcomes of stellar evolution.

⁴The MUCHFUSS project also revealed about 20 He-sdOs which show significant RV variability (Geier et al., 2011). The reason for this variability remains unknown, they may not be binaries.

1.3.2 Wide binaries with composite spectra

Another binary population of hot subdwarfs has been investigated in more detail. Long period binaries with orbital periods on the order of 1000 days were explored during the last years. 20 - 30 % of the subdwarf population show composite spectra, meaning, that not only the subdwarf (sd) but also its companion star is visible in the spectrum. The companion is identified to be a F/G/K star. The sample may, of course, be contaminated by a selection bias. In order to see a composite spectrum in the optical, the flux ratio of the stars have to match, which is the case in sd + F/G/K systems. Otherwise one component dominates the optical spectrum by far and the second component may not be visible.

The problem in analyzing these long period systems is, that because of low radial velocity shifts a significant coverage of the orbit with high resolution is needed to determine orbital parameters with good accuracy. This requires much observation time. In 2013, 3 sdB + MS systems were solved by Vos et al. (2013) and periods were found between 700 and 1300 days. The subdwarfs in these wide systems seem to form a totally different population, since they challenge the binary evolution channels (see Sec. 1.2.4). Interactions between both components via stable RLOF are possible up to periods of 1100 days only, of course depending on the model. Also some details in the simulations don't match the observations. Which mechanism is responsible for the red giant to lose almost its entire envelope?

If stable RLOF takes place, the orbits are expected to be circular after this phase of stellar evolution. Surprisingly, Vos et al. (2012) and Barlow et al. (2012) both found evidence that there also seem to be systems which have unexpectedly large eccentricities $e > 0.1$. Phase dependent RLOF is considered to be capable to produce such high eccentricities (Vos et al., 2015). However, for shorter periods and therefore smaller orbital separations, the eccentricities are observed to be low while phase dependent RLOF models tend to also produce high eccentricities at lower orbital separations. More theoretical effort is needed to solve this discrepancy.

As previously pointed out, progress in the examination of the population of wide subdwarf binaries is only made very slowly, since a decent coverage of the orbit is necessary to derive orbital parameters. However, in order to address questions like to which stellar population these binaries belong to (e.g. the halo or the disk population) the knowledge of the orbits is not required. Since diffusion processes have altered the chemical composition of the atmosphere subdwarf stars do not show any characteristics in their spectrum which may allow to draw conclusions about the stellar population they are associated to. However, in F/G/K + sd binaries the cool companion still maintained its initial composition in its atmosphere. In some cases, if the fluxes of both the subdwarf and the companion are almost equal, a composite spectrum may allow to directly see spectral lines which originate from its cool companion. Measuring its metallicity, for instance, helps then to have a clue on the formation of those systems. The main goal of this work is to find atmospheric parameters and therefore disentangle sd + F/G/K systems.

Most published investigations are restricted to photometric methods. Girven et al. (2011) modelled, starting from the spectral energy distribution (SED) of synthetic spectra, the outcome of photometric measurements of the corresponding stars. They used this, to fit

SDSS photometry with their models in order to find DA white dwarfs with companion. One advantage of this method compared to disentangling the whole spectrum is the good availability of data from photometric surveys. Furthermore, the calculation times are fast because there are only few photometric data points. Therefore, the SED-fitting method is suitable for huge samples. The downside is that photometry can only very poorly constrain parameters like surface gravity or element abundances. However, combining the two approaches allows to hunt for interesting objects in huge samples using SED-fitting, and then analyzing the interesting objects in more detail using spectral fitting. Currently, Johannes Schaffenroth and Andreas Irrgang work on the SED fitting routine, which will work in close collaboration with the spectral disentangling code developed in the course of this thesis.

A similar spectroscopic approach like in this work was published by Németh et al. (2012). They disentangled spectra of 29 binary systems by quantitative spectral analysis of their optical spectra for both stars simultaneously. They computed their own non-LTE models for hot subdwarfs and found A,F and G type companions. In the meantime, more sophisticated models for subdwarf atmospheres became available, which was the main driver for this thesis to follow a similar approach. In contrast to this project, Németh et al. (2012) calculated their synthetic subdwarf spectra on the fly. Here, pre-calculated libraries will be used to speed up the calculation time. Another difference is that in the former project the spectra have been normalized to arbitrary flux units. In this work, physical units are used throughout the whole data analysis allowing to put physical constraints or constraints from other measurements on the parameters. Furthermore, this project is targeting spectra from SDSS. These spectra cover a broad wavelength range from the UV to the IR, depending on the spectrograph (see Sec. 1.4). They also provide a reliable flux calibration, making it possible to deal with absolute physical values. Using the flux calibration and linking the surface gravities and masses of both components allows to put stronger constraints on the parameters (see Sec. 2.5.2). Furthermore, SDSS removes telluric lines, which are originating in earth's atmosphere and especially present in the IR. The science-ready properties of SDSS spectra and the nature of the method chosen for the disentangling in this work is as simple as possible but as sophisticated as needed. Therefore, this approach is expected to produce reliable values within a relatively short amount of calculation time.

1.3.3 Composite spectra

Since dealing with binary spectra is a central aspect of this work, we shall have a closer look at them. Dealing with spectra of binary systems where each star is totally different from its companion has some special characteristics. In the case of sd + F/G/K binaries the most obvious property is the huge difference in temperature. According to Wien's displacement law (Eq. 1.2) the temperature shifts the emission peak in the spectrum. Fig. 1.8 shows a large part of the spectral energy distribution of a sdO + G5III binary. The temperature of the sdO is around 58500 K, which implies that its emission maximum is located in the UV. Its MS companion has a temperature of 5270 K, hence, its maximum is in the optical. In the region between 3000 and 5000 Å the fluxes are on the same order of magnitude. This

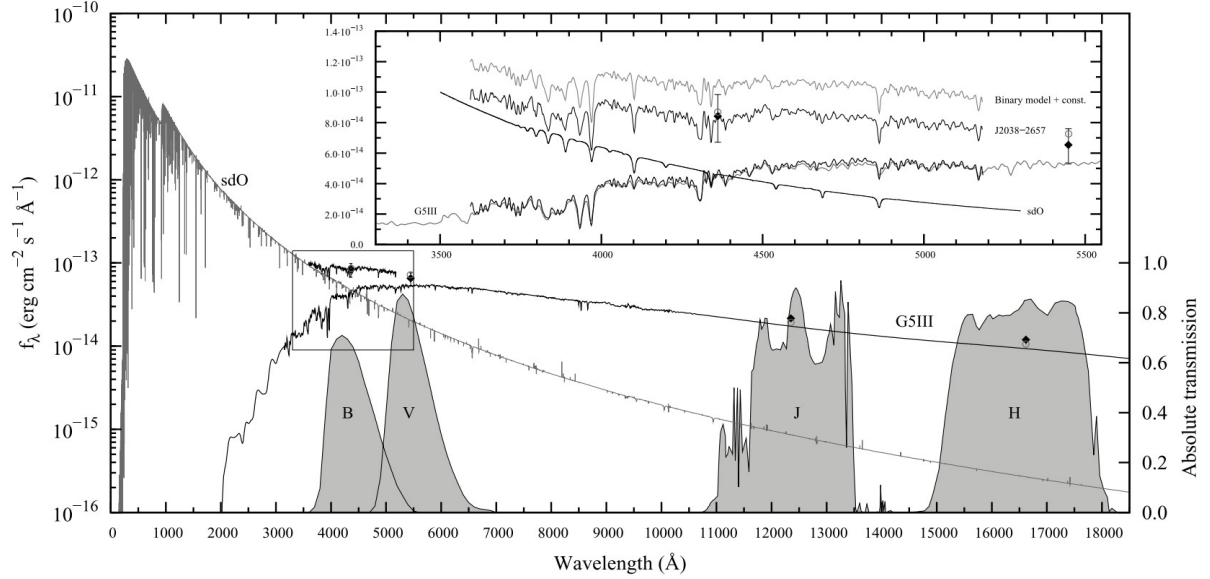


Figure 1.8: Spectral energy distribution of a sdO + G5III star (model spectra). The emission maxima are in the UV (sdO) and optical (G5III), respectively. The existence of a region in the optical where fluxes are almost equal allows to see lines of both stars simultaneously. The transmission function of B, V J and R filter are depicted in grey. The region, where the contribution to the total flux of the binary is almost equal from both components and the decomposition of the binary obtained by model fitting is depicted separately in the box in the top right corner. Lines from the sdO as well as from the MS star are visible in this region. From Németh et al. (2012).

allows to observe lines from the sdO as well as from the cool companion.

Fig. 1.9 shows the observed spectrum of a sd + G binary. In addition to the strong helium features, lines that must originate from a cool companion are visible. Since the subdwarf is typically poor in hydrogen its companion contributes significantly to the H lines even though it may be much fainter. In addition, a magnesium triplet around 5170 Å and a calcium triplet in the IR are visible, which are not observed in single subdwarfs. The G-band around 4300 Å, a CH absorption band in K and a blend of iron group lines in G and F type stars, is an additional persuasive hint on the presence of a cool companion. The Ca II H+K lines at 3968 Å and 3933 Å are likely to be contaminated by interstellar matter. In order to be able to analyze both stars simultaneously, a good measure for each of the companions should be visible in the spectrum. This means, it is by far easier if the spectrum shows lines which originate from one of the stars only. All these important lines are summarized in Tab. 1.2.

The question might arise, whether it is easier to look at both stars separately via taking a UV and an IR spectrum of the object of interest, because in these regimes one of the stars dominates by far. This might allow a separate analysis. However, spectra in the near-UV and near-IR might still show contamination from the second component. Furthermore, it is impossible in UV and very difficult in the IR to take spectra from ground, since

⁵<http://physics.nist.gov/>

F/G/K star		sdB/O		both	
λ [Å]	Transition	λ [Å]	Transition	λ [Å]	Transition
3933.7	Ca II K-line*	4026.2	He I (sdB)	3835.4	Balmer series
3968.5	Ca II H-line*	4101	H+He II	3889.0	Balmer series
4226.7	Ca I	4200	He II (sdO)	3970.1	Balmer series
4290-4310	G-Band	4340	H+He II	4101.7	Balmer series
5167.3	Mg I triplet	4471.5	He I (sdB)**	4340.5	Balmer series
5172.7	Mg I triplet	4541	He II (sdO)	4861.2	Balmer series
5183.6	Mg I triplet	4685.7	He II (sdO)	6562.7	Balmer series
5890.0	Na I*	4713.1	He I (sdB)	8662	Paschen series
8498.0	Ca II triplet	4861	H+He II	8748	Paschen series
8542.1	Ca II triplet	4922	He I (sdB)	8860	Paschen series
8662.1	Ca II triplet	5015.7	He I (sdB)	9012	Paschen series
		5875.6	He I (sdB)**	9226	Paschen series
		6678.2	He I (sdB)	9543	Paschen series
				10046	Paschen series
				10935	Paschen series
				12814	Paschen series
				18745	Paschen series

*Interstellar component may be present

**Also in sdO stars if not extremely hot ($\lesssim 80000$ K)

Table 1.2: Important lines in the spectra of sd + F/G/K binaries. Helium lines occur mostly due to the subdwarf's atmosphere, whereas the MgI and CaII triplets originate from the MS star. Wavelengths are from NIST database⁵ and Drilling et al. (2013).

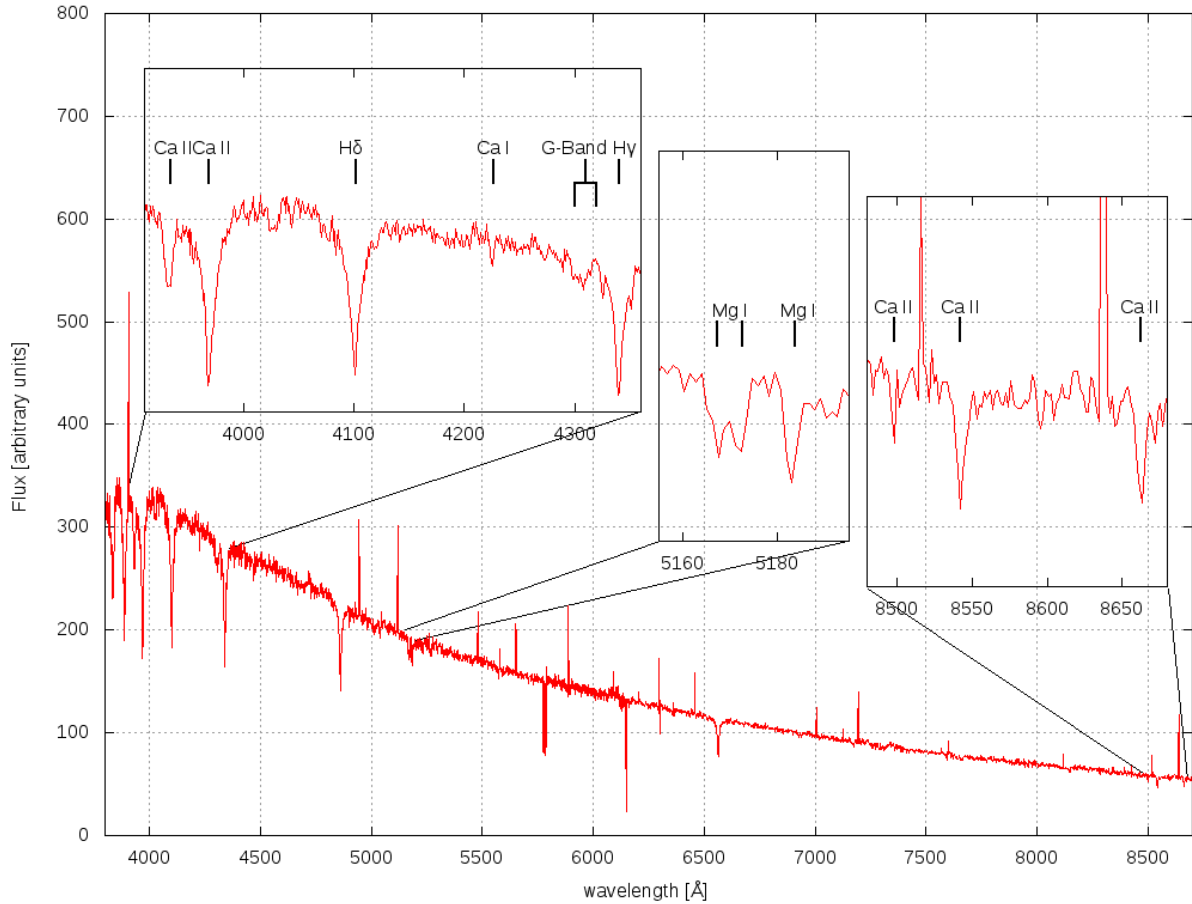


Figure 1.9: Observed spectrum of candidate SDSS J1351-0801 taken from SDSS. Lines that are a hint on the presence of a cool companion are marked.

Earth’s atmosphere is absorbing radiation in these spectral regimes, leaving space telescopes or difficult and sophisticated corrections as the only options. Of course, ground based spectroscopy is much more cost efficient and it is much easier to obtain high resolution spectra in the optical from ground. This justifies the technical effort which must be put in the disentangling of these spectra. The disentangling-problem is addressed in this work.

1.4 The Sloan Digital Sky survey

The Sloan Digital Sky Survey opens a treasure chest full of data to astronomers. This survey uses a 2.5m telescope at the Apache Point Observatory, New Mexico. It contains photometric data for objects on one fourth of the sky down to 20 mag and fainter, originally aiming for high-redshift galaxies. SDSS publishes the data in form of data releases, the current data release is DR12. Objects for spectroscopy are chosen based on the photometric data and spectra with multifibre spectrographs are taken. For each selected object, 3 x

15 min exposures ensure a good signal to noise ratio for the spectrum. Blue stars may be similar to galaxies from a photometric point of view meaning that they are often selected for spectroscopy because measuring galaxy redshifts was the main goal of SDSS. Therefore, the survey database contains many spectra of blue stars.

The former SDSS spectrograph was replaced by a similar but more advanced instrument, the BOSS spectrograph, from DR9 on. Spectra from the SDSS spectrograph are, of course, still available. The characteristics of both instruments are summarized in Tab. 1.3. The given resolution should be taken with care, because it is only a rough number. There is a complex wavelength and fibre dependence which is discussed later in detail (see Sec. 4.2). As discussed before, SDSS provides flux calibrated spectra, also corrected for telluric absorption lines.

Feature	SDSS	BOSS
Fibers per plate	640	1,000
Fiber diameter	3 arcsec (180 μm)	2 arcsec (120 μm)
Wavelength coverage	3800-9200 \AA	3650-10400 \AA
Resolution	both: 1500 at 3800 \AA , 2500 at 9000 \AA	
Wavelength calibration	< 5 km s ⁻¹	

Table 1.3: Technical specifications of BOSS and SDSS spectrograph. BOSS is used since data release 9. The resolution is given in $\frac{\lambda}{\Delta\lambda}$. It is a rough number only, because it depends on the fibre. From SDSS Website⁶.

⁶http://www.sdss3.org/dr9/spectro/spectro_basics.php

Summary

- Hot subdwarf stars are core helium burning stars on the horizontal branch. They subdivide into sdB and sdO stars, which look similar to B and O type main sequence stars from a photometric point of view, but are much fainter.
- Hot subdwarfs stars challenge current stellar evolution models. Binaries consisting of sd + G/F/K and sd + WD are easy to explain with binary evolution. However, the number of single subdwarfs observed is too high to match binary population synthesis predictions.
- The challenge in forming hot subdwarfs is to get rid of almost the complete hydrogen envelope of the star. Binary evolution including mass transfer mechanisms like Roche lobe overflow and common envelope phases are promising formation scenarios. Also mixing inside the star itself can explain the highly He dominated atmosphere, but require special physical conditions for efficient mixing.
- Wide binaries sd + G/F/K with composite spectra have been investigated in the last few years. Their orbits were solved and revealed unexpected high eccentricities and orbital periods of 700-1300 days, which is right at the boarder to be compatible with the RLOF channel of binary population synthesis.
- The spectrum of sd + G/F/K binaries shows in the optical lines from both stars. Thus, this part of the spectrum can therefore be used to derive atmospheric parameters. The knowledge of the metallicity of the cool companion for instance allows the association of the binary to a specific population.
- SDSS contains many spectra of blue stars. The data is science-ready (flux calibrated, corrected for telluric absorption lines). The disentanglement of SDSS spectra is the aim of this project.

2 The procedure

This section describes the way from the first idea, the development of the procedure itself to the final code.

2.1 Project Outline

As previously discussed, this work's targets are sd + F/G/K binary systems - in particular the determination of atmospheric parameters for both components from optical spectra. The motivation of starting this project was the availability of spectra from the SDSS for a list of stars likely to be subdwarfs. Kreuzer (2013) studied a sample of faint blue stars which did neither correspond to the position of the main sequence nor to the horizontal branch (see Fig. 4.3). They showed a strong redshift in a color-color plot. As interstellar reddening could be excluded (for detailed discussion see Sec. 4.2), the only reasonable remaining option was the presence of a cool companion which may provide additional flux in the IR. Visual inspection of their spectra showed indeed the presence of low ionisation lines which cannot originate from the subdwarf but are found in F/G/K stars. But how to disentangle the composite spectra and find the contribution of each star to the combined flux?

Let us have a look on how the observed spectra are produced by nature: A binary system has two sources of radiation which are not resolvable from earth and therefore look like a single source in the spectrum. Each star produces its own emission flux, F_1 and F_2 . Since fluxes are normalized energies (and do for instance not scale in a logarithmic form, like the magnitude scale), they get simply added for large distances:

$$F_{\text{composite}} = F_1 + F_2 \quad (2.1)$$

Fig. 2.1 illustrates this in terms of their spectra. Of course, reddening due to the interstellar medium is ignored here. The code which is developed in the course of this thesis should have the capability to disentangle the composite spectrum again in order to find the contribution of each single star to the combined flux. It searches for the combination of atmospheric parameters for the hot subdwarf and its companion which reproduces the observed spectrum best. This is done by using basic fit techniques, which are described in Sec. 2.5. In order to be able to go the same steps as nature in producing a composite spectrum, a library of pre-calculated spectra is needed for each, the subdwarf and the cool companion. These are discussed in Sec. 2.2.

Since the aim of this project is comparably specific, the code is developed from scratch in C++ following object oriented principles. However, the code should also have some flexibility.

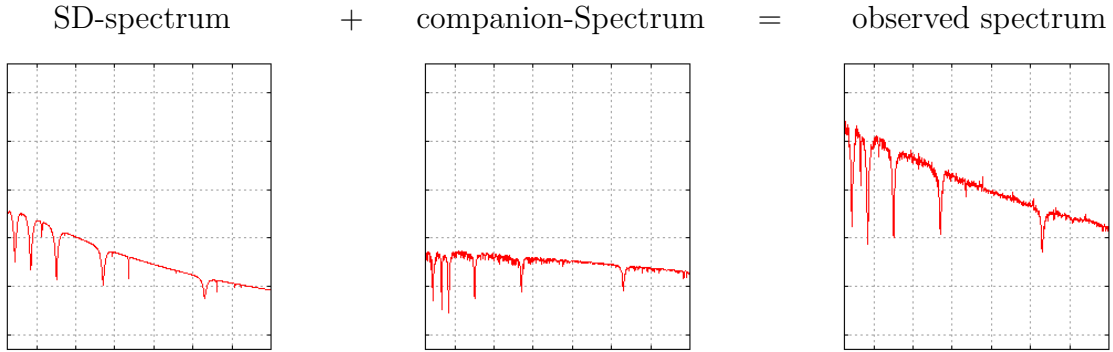


Figure 2.1: Nature produces the observed spectrum by just adding up the flux contributions of each star in a binary. The code developed in this work tries to disentangle the composite spectrum again in order to find the atmospheric parameters of both stars.

Even though it will not be tested in the course of this project, the code should have the capability to disentangle all kinds of binaries based on their spectra in all spectral ranges - as long as suitable libraries are provided. Technical details concerning the implementation and the memory management are discussed in Sec. 2.8.

2.2 Spectral libraries

Spectral libraries (also called *grids*) are needed in order to be able to calculate a spectrum for a given combination of parameters. They consist of pre-calculated synthetic spectra which cover a large part of the physically possible parameter space. In the ideal case, the grid looks like an n -dimensional array of spectra, where n is the number of parameters which are varied and can therefore be fitted using this grid. A suitable grid should fulfil the following properties as good as possible:

- A grid should have at least the resolution of the observation which is to be fitted. Otherwise, information contained in the observed spectrum is wasted.
- The wavelength coverage of each single spectrum in the grid should be at least the same of the observed spectrum. Otherwise, also information is wasted.
- The grid points should be as close as possible to each other in order to have a template available close to any combination of parameters.

Of course, the available memory for storing the grid and the CPU power for calculating the grid are the limiting factors. This makes it necessary to find a good trade-off between the above mentioned points and hardware availability.

In order to be able to fit a binary system, two different grids - one for each component - are needed. Both grids already include the effect of atmospheric broadening described in Sec. 1.1.3 which is necessary to distinguish between different temperatures and surface

gravities. The model grids which came into question for this work are briefly discussed in the following.

2.2.1 non-LTE TLUSTY/SYNSPEC subdwarf grid

This subdwarf grid was calculated by Nemeth et al. (2014). It covers the whole parameter space observed for (He-)sdBs and (He-)sdOs. Nemeth et al. (2014) used the code *TLUSTY*, developed by Hubeny & Lanz (1995) for calculating their model atmospheres and *SYNSPEC* (Hubeny & Lanz, 2011) for the determination of the synthetic spectra.

The grid assumes pure H/He composition of the subdwarf and is calculated in opacity sampling mode. This means that the equation of radiative transfer is only solved for particular wavelengths of interest, in contrast to the treatment via opacity distribution functions. The models also account for non-LTE effects and consider Stark broadening of hydrogen lines. The wavelength range spans from 3120-7520 Å and thus does not allow for using the CaII IR triplet mentioned in Tab. 1.2 in the fits. The parameters and corresponding step sizes of the grid are summarized in Tab. 2.1. The overall library has a size of 8.5 GB.

parameter	lower limit	stepsize	upper limit
λ [Å]	3120	0.01-0.25	7530
T_{eff} [K]	20000	1000	56000
$\log g$ [cgs]	5.0	0.1	6.3
n_{He}/n_H	0.0005	$\times 2$	100

Table 2.1: Parameters and the corresponding ranges covered by the *TLUSTY/SYNSPEC* grid calculated by Nemeth et al. (2014).

2.2.2 PHOENIX library

An extensive grid of *PHOENIX* stellar atmospheres and spectra was calculated by Husser et al. (2013). These high resolution spectra span the whole parameter range observed for F/G/K stars and more. One of the advantages of this library is the huge spectral coverage from 500 Å to 5.5 μm, which makes it suitable for a huge variety of applications, including SED fitting. All spectra are available in an outstanding resolution ($R=500000$ in the optical, $R=100000$ in the IR). In order to shift the wavelength scale from vacuum to air wavelengths, the formula from Ciddor (1996) was used. The grid covers all physically possible combinations of the parameters given in Tab. 2.2. Up to now, it consists of 50000 synthetic spectra, making it a state-of-the-art spectral library. The overall size of the grid (in ASCII-files) is 134 GB.

parameter	lower limit	stepsize	upper limit
T_{eff} [K]	2300	100	700
T_{eff} [K]	7000	200	12000
$\log g$	0	0.5	6.0
$\log [\text{Fe}/\text{H}]$	-4	1.0	-2
$\log [\text{Fe}/\text{H}]$	-2	0.5	+1
$\log [\alpha/\text{Fe}]$	-0.2	0.2	+1.2

Table 2.2: Parameters and the corresponding ranges covered by the *PHOENIX* grid (Husser et al., 2013).

2.3 Interpolation in spectral grids

The grids consist of stellar spectra, arranged in a regular pattern in parameter space. In order to be able to fit the parameters to a higher precision than the step size of the grid, two options remain: Either calculate the required synthetic spectra on the fly (like Németh et al. (2012)) or use an interpolation method to determine the spectrum from surrounding grid nodes. The first option requires much more calculation time because not only one synthetic spectrum has to be calculated in each step, but two of them are required for a binary fit. Therefore the second method is preferred in this work. The interpolation will be done in a linear way. For each star, three parameters can be determined, which means that the interpolation needs to be implemented at least in three dimensions.

Recall the standard linear interpolation in one dimension as illustrated in Fig. 2.2. Suppose, the values of a function $f(x)$ are known at points x_0 and x_1 . In order to estimate the value of $f(x_2)$, if $x_0 \leq x_2 \leq x_1$ holds, the linear interpolation is feasible using the equation

$$f(x_2) = f(x_0) + m \cdot (x_2 - x_0) \quad (2.2)$$

where the slope m can be written as

$$m = \frac{f(x_1) - f(x_0)}{x_1 - x_0} \quad (2.3)$$

Replacing m in Eq. 2.2 by the expression 2.3 and simplifying it yields an equation which can be evaluated numerically.

$$f(x_2) = \frac{f(x_0)(x_1 - x_2) + f(x_1)(x_2 - x_0)}{x_1 - x_0} \quad (2.4)$$

In terms of interpolation in spectral grids, the x_i are the steps in the parameter space, while $f(x_i)$ is the flux of the synthetic spectrum for the corresponding parameter x_i . Expression 2.4 needs to be evaluated for each data point in the spectrum. This approach is valid, if

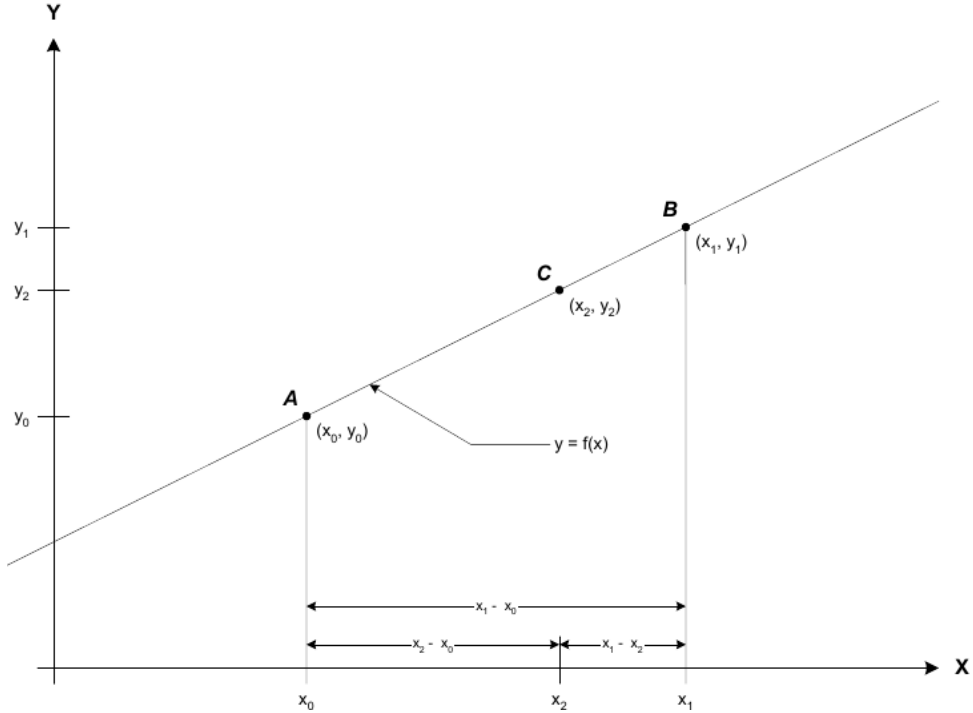


Figure 2.2: Linear interpolation in one dimension. The value of $f(x)$ at point x_2 is estimated from the surrounding points x_0 and x_1 . From Wagner.

the known function values $f(x_0)$ and $f(x_1)$ are not too far apart from each other, i.e. the step size in the grid is small enough.

The procedure described above can easily be generalized to more dimensions. As mentioned before in this work three atmospheric parameters (T_{eff} , $\log g$, $[\text{Fe}/\text{H}]$ or $[\text{He}/\text{H}]$) for each star in the binary will be determined, therefore, we shall have a look at the three-dimensional case.

Fig. 2.3 illustrates the problem: In the parameter space, the surrounding grid nodes A, B, \dots, H are used to determine an estimate for the synthetic spectrum at point I . The procedure is adapted from Wagner.

Drawing planes parallel to the $X - Y$, $X - Z$ and $Y - Z$ planes intersecting each other at point I divides the volume defined by the surrounding nodes into 8 sub-volumes. Firstly, the normalized Volumes N_a, N_b, \dots, N_h of the sub-volumes are being calculated. Normalized hereby means that the absolute value is divided by the full volume V of the cuboid defined by the surrounding grid nodes A, B, \dots, H .

$$V = (x_1 - x_0) \cdot (y_1 - y_0) \cdot (z_1 - z_0) \quad (2.5)$$

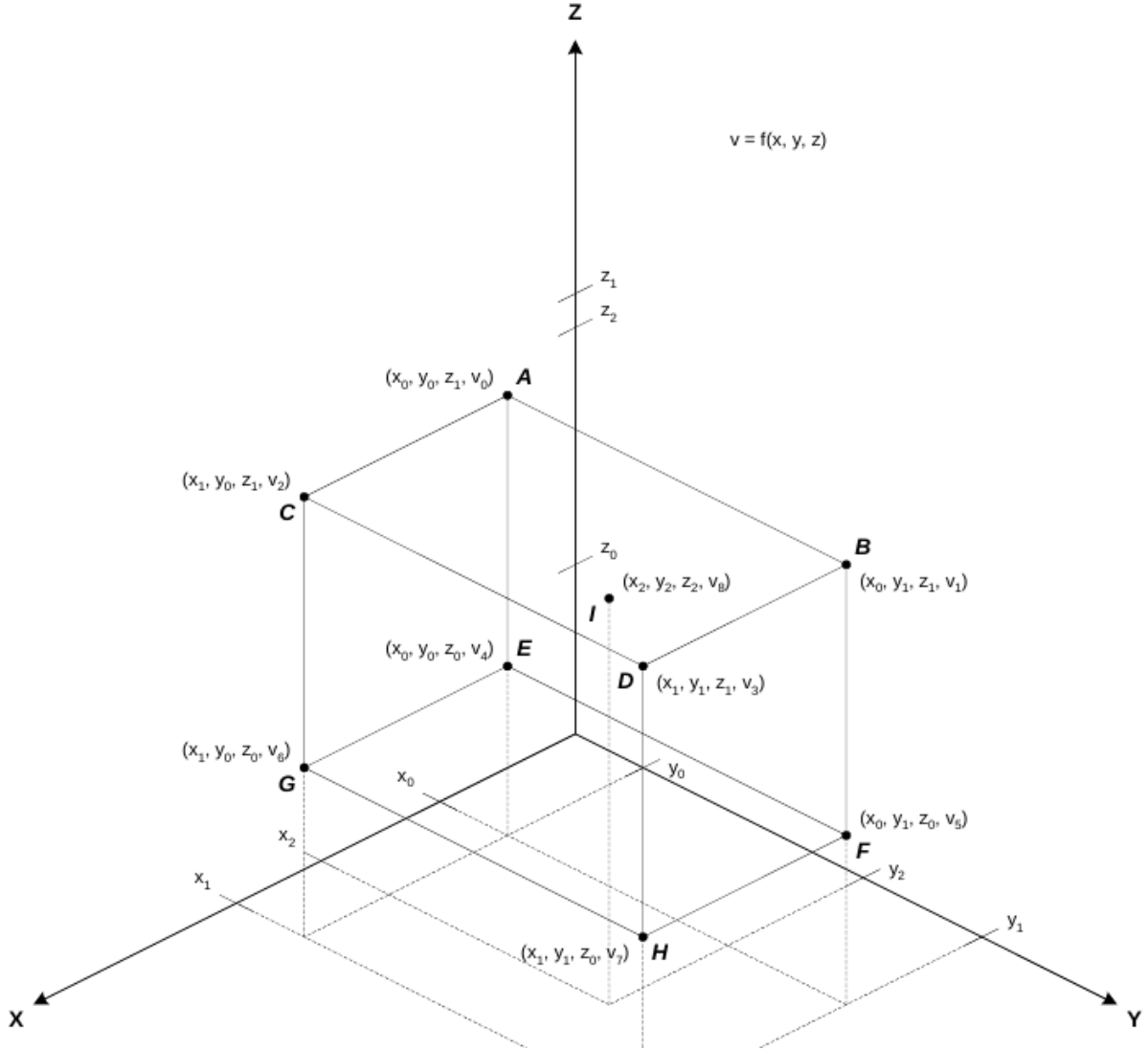


Figure 2.3: Linear interpolation in the grid in 3 dimensions. The figure illustrates, how the spectrum at point I is estimated from the surrounding grid nodes. See text for details. From Wagner.

$$N_a = \frac{(x_1 - x_2) \cdot (y_1 - y_2) \cdot (z_2 - z_0)}{V} \quad (2.6)$$

$$N_b = \frac{(x_1 - x_2) \cdot (y_2 - y_0) \cdot (z_2 - z_0)}{V} \quad (2.7)$$

$$\vdots$$

$$N_h = \frac{(x_2 - x_0) \cdot (y_2 - y_0) \cdot (z_1 - z_2)}{V} \quad (2.8)$$

The function value at point I $f(I) = v_8$ can then be estimated from the function value at the

surrounding grid nodes v_0, v_1, \dots, v_7 by weighting them with the corresponding normalized volume N_i .

$$v_8 = v_0 \cdot N_a + v_1 \cdot N_b + v_2 \cdot N_c + v_3 \cdot N_d + v_4 \cdot N_e + v_5 \cdot N_f + v_6 \cdot N_g + v_7 \cdot N_h \quad (2.9)$$

Again, Eq. 2.9 needs to be evaluated for all data points in the spectra. However, from a numerical point of view interpolating in three dimensions is not much time demanding since it only involves additions and multiplications, which are executed fast. The calculation time scales linearly with the number of data points in the spectrum.

2.4 Convolution

Adding and comparing spectra in a numerical way requires the wavelength of their data-points to match exactly. But not only the wavelength of each data point is important: It is also necessary for all spectra - the libraries as well as the observed spectra - to have the same resolution. Since it is not advisable to modify observations, the resolution of the libraries need to be adapted to that of the observed spectrum. This can be done by applying a *convolution* with a Gaussian function which is a good approximation of the instruments profile.

In mathematics, a convolution is an action which could be applied to two functions and could be described as the "integral of the point-wise multiplication of the two functions as a function of the amount that one of the original functions is translated"¹. It can be written as

$$(f * g)(x) = \int_{-\infty}^{\infty} f(\tau)g(x - \tau)d\tau \quad (2.10)$$

Consider a spectrum taken by a spectrograph. Due to instrumental effects and, most importantly, the finite resolving power, a line is smeared. The same effect must be applied to a spectrum if one wants to compare a library spectrum to observations. This is done by applying a convolution to the spectrum, where the broadening function ($g(x)$ in Eq. 2.10) is chosen to be a Gaussian function where its Full Width at Half Maximum (FWHM) is set to be the FWHM of the spectrograph's instrumental profile.

$$g(x) = \frac{1}{\sigma\sqrt{2\pi}} \exp \left[-\frac{(x - x_0)^2}{2\sigma^2} \right] \quad (2.11)$$

$$\text{FWHM} = 2\sqrt{2 \ln 2} \sigma \approx 2.355 \sigma \quad (2.12)$$

In astronomy, the FWHM of an instrument could be measured for instance by fitting a Gaussian profile to the spectral lines of a reference lamp. The lines of reference lamps are due to an extremely tiny intrinsic broadening clearly dominated by the broadening of the instrument. The numerical treatment of the convolution is described in Sec. 2.8.2. The impact on spectra is shown in Sec. 3.2.

¹<https://en.wikipedia.org/wiki/Convolution>

2.5 Core - Fit algorithm

2.5.1 Function minimization

The problem of finding atmospheric/physical parameters from a stellar spectrum can not be addressed in a direct way. Reading parameters out of an observed spectrum is simply impossible. However, this problem can be rewritten as: Finding a synthetic spectrum with a given set of atmospheric/physical parameters, which is capable of reproducing the observed one as good as possible. In order to allow an algorithm to decide how good a synthetic spectrum fits the observation the "goodness" needs to be quantified. A commonly used measure is the χ^2 , defined as

$$\chi^2 = \sum_i \left(\frac{F_{i,model} - F_{i,observation}}{\sigma_i} \right)^2 \quad (2.13)$$

The index i runs over all data points and σ_i denotes the uncertainty of the data point, given by $F_{i,model}$ divided by the S/N of the spectrum. From Eq. 2.13 it can be seen that the value of χ^2 is lower the better the model fits the data. To judge the goodness of the fit, it is also common to define the reduced χ^2 .

$$\chi^2_{red} = \frac{\chi^2}{n} \quad (2.14)$$

Here, n denotes the number of degrees of freedom, which is defined by the number of data points of the observation minus the free parameters of the fit. This yields n usually being a large value when fitting optical spectra. However, χ^2_{red} should be ~ 1 to denote a good fit. If the value is lower, the uncertainties of the measurement seem to be overestimated, because the data scatters around the model less than the assumed σ . If the value is higher, either the errors were underestimated or the model is not suitable to reproduce the data. How well a synthetic spectrum matches the observation is dependent on the set of chosen parameters \vec{p}_i of the synthetic spectrum. Therefore, χ^2 can be interpreted as a function of these parameters.

$$\chi^2 = \chi^2(p_1, p_2, \dots, p_n) \quad (2.15)$$

With this interpretation in mind, the problem boils down to finding the minimum of a function. Multiple so-called *fit algorithms* are known to numerically solve this problem. Standard minimum bracketing methods or methods which follow the gradient of the function until they reach the minimum can be applied. Also more sophisticated approaches are available, amongst them the simplex algorithm which is used in this work. A detailed description of the latter one is given in Sec. 2.5.3.

2.5.2 Free parameters and physical constraints

The parameters \vec{p}_i to be fitted in this work are summarized in Tab. 2.3. The ranges in which these parameters can be varied are constrained by the available model spectra, see

Tab. 2.1 and Tab. 2.2.

F/G/K star				subdwarf star			
T_{eff}	$\log g$	$\log [\text{Fe}/\text{H}]$	$M [\text{M}_\odot]$	T_{eff}	$\log g$	$\log [\text{He}/\text{H}]$	θ

Table 2.3: Free parameters which will be fitted with the code developed in this work using the simplex algorithm.

Some of these parameters are constrained in a physical way or dependent from each other. It is advisable to make use of this additional information.

c) Surface ratio The flux value in synthetic spectra is usually given in energy emitted from the stellar surface per area, per second and per wavelength

$$[F] = \frac{erg}{s \cdot cm^2 \cdot cm} \quad (2.16)$$

The observed flux F_{obs} of an observed binary can be written as integrals over the visible surfaces of the primary (p) and the secondary (s) component of the binary. The primary component is commonly defined as the more massive one.

$$F_{tot,obs} = \frac{1}{d^2} \int_{A_p} F_p + \int_{A_s} F_s \quad (2.17)$$

F_1 and F_2 are again given in energy emitted from the stellar surface per area, per second and per wavelength and d is the distance to the binary, which is assumed to be the same for both components.

Furthermore, the surface gravity of a star can be expressed in terms of the mass M and the radius R

$$g_i = \frac{GM_i}{R_i^2} \Rightarrow R_i^2 = \frac{GM_i}{g_i} \quad (2.18)$$

The *surface ratio* of both components now becomes a function of the surface gravities and the masses of both stars.

$$\frac{A_p}{A_s} = \frac{R_p^2}{R_s^2} = \frac{M_p}{M_s} \cdot \frac{g_s}{g_p} \quad (2.19)$$

Inserting this into Eq. 2.17 yields

$$F_{tot,obs} = \frac{1}{d^2} (R_p^2 \cdot F_p + R_s^2 \cdot F_s) = \frac{R_p^2}{d^2} \left(F_p + \underbrace{\frac{R_s^2}{R_p^2}}_{\text{surface ratio}} \cdot F_s \right) = \frac{\theta^2}{4} \left(F_p + \frac{A_s}{A_p} \cdot F_s \right) \quad (2.20)$$

Eq. 2.20 will be used in the code to connect the free parameters $\log g_i$ with the masses and the contribution of each star to the combined flux. This makes the fit routine more sensitive to $\log g$ because of the additional constraint due to the flux ratio. The representation of the pre factor θ in Eq. 2.20 has a physical interpretation. Making use of the small angle approximation, θ is the angular diameter of a star and allows the distance to a star to be determined.

$$\frac{\theta}{2} = \frac{R}{d} \quad (2.21)$$

d) Masses In order for Eq. 2.20 to be used in the code, it is necessary to make some assumptions for the masses (see Eq. 2.19). For the mass of the subdwarf the canonical mass of $0.48M_{\odot}$ is assumed. This mass is in agreement with observations and theory. The mass of the cool companion will be fitted. However, it can be constrained to be between 0.7 and $1.5 M_{\odot}$ corresponding to F/G/K dwarfs. In a few cases the companion could be a giant. Such a case will easily be detected from the large surface ratio. If the mass would be lower, the star would not be visible in the optical spectrum. The existence of subdwarf companions with higher masses is not observed and would also be in contradiction to the canonical evolution scenario since higher mass stars evolve much faster.

2.5.3 Downhill Simplex

2.5.3.1 Function minimization using the simplex algorithm

The core of the code is the fit algorithm itself. Several well-known and commonly used fit algorithms are available in literature. Due to reasons which will be discussed at the end of this section the *simplex method* based on Press et al. (2007) is used. This method will be introduced in the following. It was first proposed by Nelder & Mead (1965).

A simplex in n -dimensional space is a volume defined by $n+1$ vertices. In the beginning, these vertices are chosen such that they cover a large fraction of the parameter space. Hereby, each vertex is specified by a set of parameters \vec{S}_i . These sets can be merged into a *Simplex matrix* S . Each row corresponds to the set of parameters for one vertex. In order to ensure that the vertices expand into each direction of the parameter space and thus making them linear independent of each other, a common way is to initialize the simplex by taking the first set of parameters and modifying only one parameter in each row of the matrix by adding $\delta \neq 0$.

$$\vec{S}_i = \vec{S}_1 + \vec{\Delta}_i \quad \Delta_i = \begin{pmatrix} 0 \\ \vdots \\ \delta \\ \vdots \\ 0 \end{pmatrix} \leftarrow i\text{-th row} \quad i = 2, \dots, n+1 \quad (2.22)$$

The goal is now to let the simplex move through parameter space and let it contract more and more, until all points of the simplex are located in the minimum. In order to drive the simplex to lower χ^2 , the χ^2 is evaluated at each vertex in the beginning. Subsequently, in each iteration the point with the highest χ^2 , i.e. the worst combination of parameters \vec{S}_i , is rejected and replaced by better ones. The flowchart in Fig. 2.4 illustrates how this is achieved. The simplex can undergo only specific movements

- a) Reflection of one vertex with respect to all other vertices
- b) Reflection and expansion
- c) Contraction of one vertex
- d) Contraction towards one vertex

Fig. 2.5 shows a graphical illustration of these movements for a three-dimensional simplex. The reflection action (a) allows the simplex to move through parameter space during multiple iterations. Reflection in combination with expansion (b) can help to move faster if the χ^2 landscape is flat. Both contraction actions (c) and (d) yield a smaller simplex, allowing a finer sampling of the parameter space if the simplex has reached the vicinity of a minimum. In addition, both contraction and expansion is also necessary for the simplex to be able to squeeze through steep, narrow valleys in the χ^2 landscape and expand again if the landscape is flat.

In each iteration, the possible movements are checked in the given order. If one of them results in a lower χ^2 than the highest χ^2 present in the simplex the action will be executed. If no lower χ^2 can be found, the simplex seems to be already trapped in a minimum and finer sampling is necessary. In this case, the simplex contracts around the point with the lowest χ^2 .

As a criterion to terminate the procedure, the square root of the sum of the normalized quadratic deviation from the mean χ^2 of each simplex vertex r is compared to a predefined value f .

$$r = \sum_i \sqrt{\frac{(\chi_i^2 - \bar{\chi}^2)^2}{n+1}} \quad (2.23)$$

The sum runs over all $n+1$ simplex vertices. Taking this as a measure for the convergence of the fit was suggested already by Nelder & Mead (1965). The fit is assumed as converged to the minimum, if

$$r < f \quad (2.24)$$

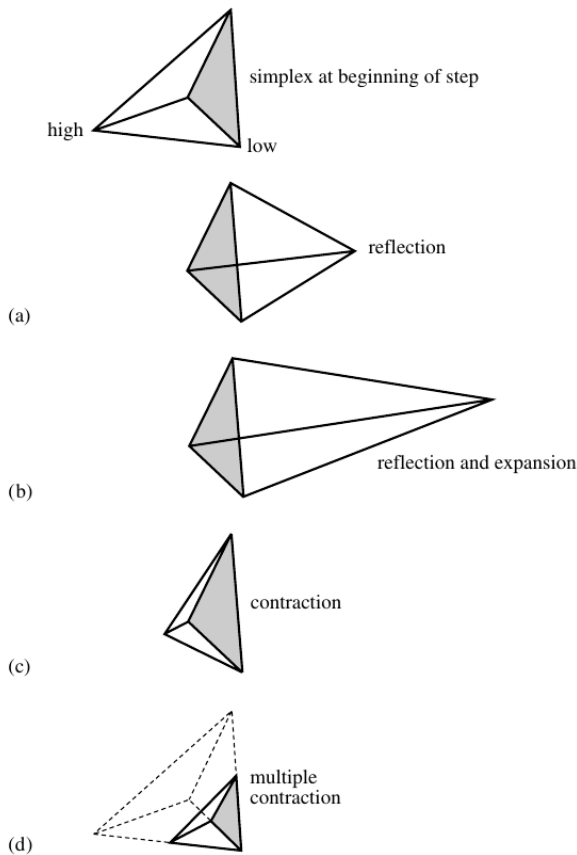


Figure 2.5: Graphical illustration of the possible simplex movements in three dimensions, from Press et al. (2007).

fit is found throughout determining the uncertainties, the whole fit procedure is initiated again, where one of the start vertices is chosen to be this better fit. If no better fit will be found any more, this vertex will survive the fit and the uncertainty determination because the simplex method always tries to get rid of the worst vertex only or contracts towards the best one.

2.5.3.2 Advantages and disadvantages of the simplex method

One major disadvantage of choosing the simplex algorithm is the complexity of the procedure. There are in fact methods that are easier to implement. Simple minimum bracketing methods for instance can be packed into just a few lines of code and even methods following the steepest descent are usually less complex. In addition, gaining insight into the fit procedure and the function itself is more difficult, which makes it tricky to find flaws and bugs in the code.

Most common function minimization algorithms follow the idea of moving through the χ^2 landscape in the direction of the steepest descent, i.e. the lowest gradient. In order to be able to follow the gradient, at least two points need to be evaluated in each step to be able

Of course, the choice of the value of f is crucial. If f is chosen too high, the fit has probably not yet reached the global minimum but is just squeezing the simplex through a local, narrow region in the χ^2 landscape. If f is too low, too many iterations and therefore calculation time is wasted, because the fit has already reached the global minimum, but the routine still has to push the simplex smaller. It turned out, that reasonable values are on the order of $f = 1 \cdot 10^{-5}$. This value was used for all fits which were carried out throughout the work on the project.

At some point, when the algorithm claims to have found a minimum, the simplex should be re-expanded and the fit procedure should be started again, while the vertex with the lowest χ^2 in the minimum is kept as one vertex of the new simplex. This is to ensure, that the minimum which was found is not only tiny local, but a global one. However, restarting is in some cases not enough to locate the global minimum. In order to calculate the uncertainties, several fits with different initial conditions are made (see Sec. 2.6.2), yielding a good coverage of the χ^2 map. If a better

to determine the derivative of the function. The simplex algorithm does not require any derivatives and therefore only requires one function evaluation at a time. This is good, because the function evaluation is the most expensive part of the whole code.

However, the probably most favourable argument for choosing the simplex algorithm to address the problem of this thesis is that the simplex algorithm is less likely to get stuck in local minima since vertices are distributed across the parameter space. Following only the gradient of a function would fail immediately if the χ^2 landscape is complex and full of tiny local minima. The fit would get stuck in one of them since gradients are increasing in each direction. Unfortunately, the simplex algorithm is also not 100% fail safe in this case, even though it is much more stable against local minima. However, as previously mentioned, determining the uncertainties requires a good sampling of the parameter space. If the fit got stuck in a local minimum, it is very likely to recognize the global one during this sampling.

2.6 Uncertainties

2.6.1 χ^2 statistics

Using χ^2 for judging the goodness of a fit allows the toolbox of χ^2 statistics to be used. The great advantage is that determining confidence limits for the resulting parameters is fairly straightforward. Consider a vector of parameters \vec{p} resulting in the best fit (and therefore in the ideal case $\chi^2_{red}(\vec{p}) = 1$). Moving away from \vec{p} increases χ^2 again by $\Delta\chi^2$. One can now define a *confidence region* where the true parameters are located inside with a given probability. If this probability is, for instance, chosen to be 68.3% (also known as "1 σ confidence level"), the confidence region confines the part of the parameter space where 68.3% of the total probability distribution is in. This region depends on the number of parameters in \vec{p} which are varied.

The cumulative probability distribution function $F_{\chi^2}^n$ can be interpreted as a function giving the accumulated probability that the true value is located at a higher χ^2 as a function of χ^2 for n free parameters. It is plotted in Fig. 2.6 for the single parameter and the two parameter case. In order to find the 1 σ confidence interval in terms of χ^2 , one needs to find the point, where $F_{\chi^2}^n$ has decreased by 68.3%. The resulting values are $\Delta\chi^2 = 1$ for the single parameter case and $\Delta\chi^2 = 2.296$ for the two parameter case. Note, that this approach is only valid, if $\chi^2_{red} \approx 1$. The same procedure can be applied to find the corresponding χ^2 for more parameters and for other confidence levels. The 99% confidence criterion would correspond to $\Delta\chi^2 \approx 6.63$.

In the one dimensional case, the confidence region in the higher dimensional parameter space needs to be projected onto just one dimension. To summarize, in order to calculate confidence intervals in practice one needs to explore the χ^2 landscape by keeping the parameters of interest fixed while fitting all other parameters. Then points of the $\Delta\chi^2$ corresponding to the desired confidence level may be connected. For only one single parameter $\Delta\chi^2 = 1$ corresponds to a 1 σ confidence interval and $\Delta\chi^2 \approx 6.63$ confines the

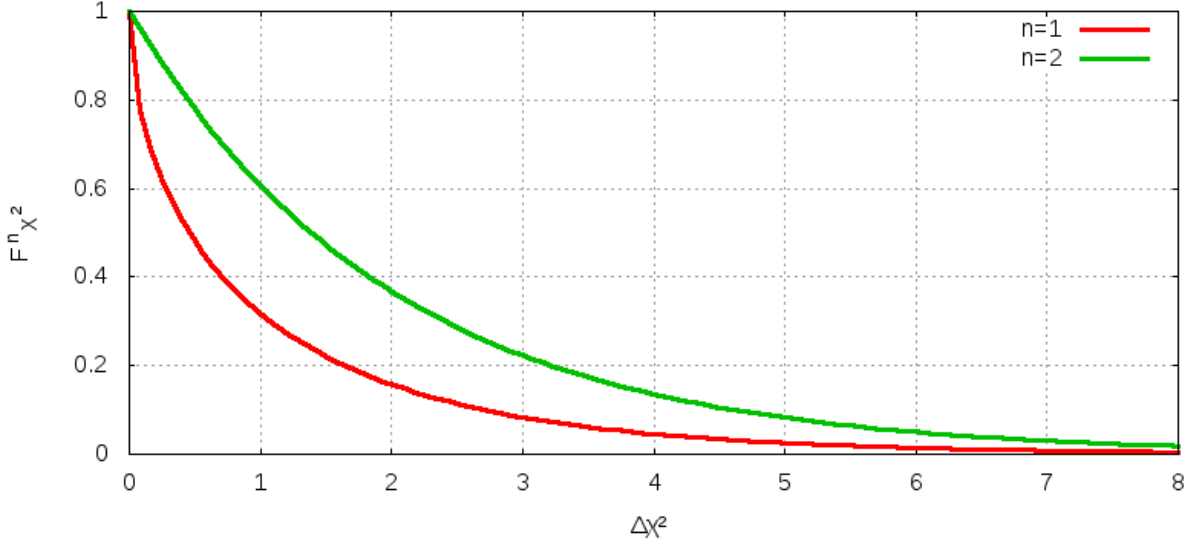


Figure 2.6: Cumulative probability distribution functions of the χ^2 distribution for $n = 1$ and $n = 2$.

99% confidence region.

2.6.2 Determination of the uncertainties

In order to calculate the confidence intervals mentioned above in the code, beginning from the position of the best fit $p_{best}^{\vec{}}$ each parameter is stepped through parameter space and kept fixed throughout the fit at every step. This means, that if a number of $m = 20$ steps around the minimum are made for each parameter,

$$N_{fits} = m \cdot \#\text{parameter} = 20 \cdot 8 = 160 \quad (2.25)$$

fits are initialized and are to be executed. 20 steps around the minimum allow a reasonable good sampling of the χ^2 landscape. The $\Delta\chi^2$ is expected to locally increase in a quadratic manner around the best fit for each parameter. Therefore, a parabola is fit to the sampled points in the $\Delta\chi^2$ landscape:

$$f(x) = a(x - b)^2 \quad (2.26)$$

where b is set to be the position of the best fit for each parameter. Due to the $\Delta\chi^2$ being taken into account here, there is no offset present in the quadratic Eq. 2.26. The only left free parameter a is found via a simple *golden section search* algorithm to fulfil $f(x) \approx 6.63$ in order to find the 99% confidence limits. There is no need for very efficient minimization because this step is not time consuming and only executed twice for each free parameter in the binary fit in order to calculate the asymmetric uncertainties. See appendix A.3 for details on the golden section search algorithm.

As a side effect, because of the different fits with different start values, the χ^2 landscape is scanned extensively. If, throughout determining the uncertainties, a χ^2 which is 0.05 lower

than the χ^2 of the already known best fit is found, the whole procedure is initiated again, starting with the new best fit. The difference required between both χ^2 values is chosen to allow the fit to improve, but avoid useless restarts of the whole procedure if the better χ^2 is only very slightly below the old one. This could be caused by the finite numerical precision or if the χ^2 map of two parameters is extremely degenerate. The minimum which survives the uncertainty determination is therefore likely to be the global one. Note, that the high number of fits to be executed make this part of the code very time consuming. However, the single fits are independent of each other. Therefore, this procedure could easily be parallelized in future implementations.

2.7 Interstellar extinction and reddening

Most astronomical objects are not seen directly but interstellar matter is in the line of sight towards the object. Interstellar matter mostly consists of dust grains which are less than 1 μm , often just a few molecules, in size. As light from an observed object passes through a cloud of interstellar dust, a part of the radiation is absorbed and re-emitted into a random direction. Thinking about the electro-dynamical law of the "half-wavelength dipole" and interpreting the grains as dipoles, it is not surprising that absorption increases towards the UV due to typical dust grain sizes. In energy distributions like spectra, the blue part is therefore stronger damped by interstellar extinction than the red part - it appears to be reddened. This reddening due to interstellar extinction therefore modifies the slope of the spectrum significantly. It is important to also take this effect into account when fitting spectra.

In flux calibrated binary spectra, the slope of the spectrum helps significantly to constrain the effective temperature of both stars. Therefore, interstellar reddening can have a direct influence on the inferred atmospheric parameters. In order to not produce degeneracies between temperatures and reddening and avoid more free parameters for the fit, the reddening will not be fitted to the observation. The reddening maps published by Schlegel et al. (1998) together with the new calibration coefficients from Schlafly & Finkbeiner (2011) provide reliable values which can simply be applied during the fit procedure. Instead of applying an artificial reddening to all synthetic binary spectra which are used throughout the fit, it is more time efficient to remove the reddening from the observation. The wavelength dependence of the interstellar extinction $A(\lambda)$ has been determined by Fitzpatrick (1999). An overview of this method will be given in the following.

Interstellar reddening can be described by the scalar quantity

$$R = \frac{A(V)}{E(B - V)} = \frac{A(V)}{A(B) - A(V)} \quad (2.27)$$

which describes the ratio of the total extinction $A(V)$ and the selective extinction $A(B) - A(V)$ in the V-band. V and B denote the corresponding filters in the UBV photometric system (also called *Johnson system* (Johnson & Morgan, 1953)). $E(B - V)$ is called the *reddening parameter*. The parameter R is dependent on the medium which causes the

extinction. It can vary between 2.2 and 5.8, while 3.1 is appropriate in most cases because it well describes diffuse interstellar matter in the Galaxy. Fitzpatrick (1999) calculated anchor points for an extinction curve of different values of R from 2700 Å up to infinity in terms of extinction at different wavelengths $A(\lambda)$ up to infinity. Their extinction curve for the $R = 3.1$ case is shown in Fig. 2.7.

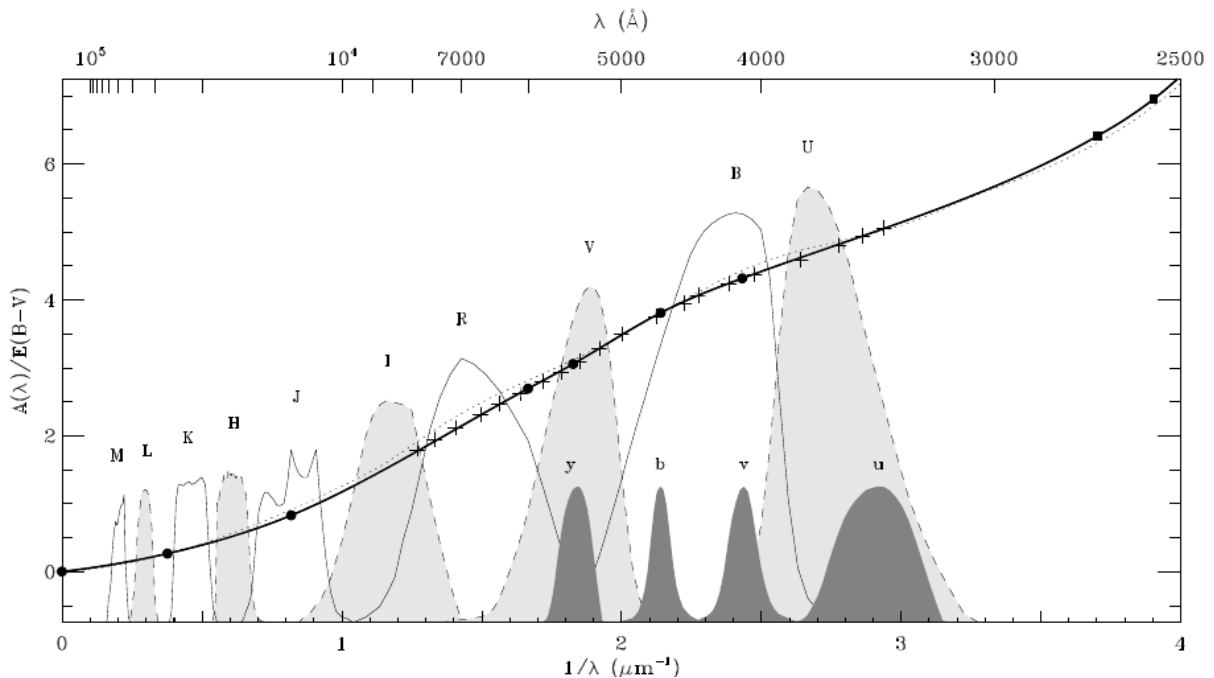


Figure 2.7: Interstellar extinction for different wavelengths. Note that the bottom scale is in inverse microns. The solid line denotes $R = 3.1$, corresponding to diffuse interstellar matter, derived from a cubic spline interpolation, using their anchor points (dots and squares). Commonly used photometric filter systems are over-plotted with arbitrary normalization. From Fitzpatrick (1999).

The Figure 2.7 shows, that in the IR and optical, the extinction curve of Fitzpatrick (1999) has no strong curvature in $1/\lambda$ -representation. Cubic spline interpolation between the anchor points in Fig. 2.7 is sufficient to derive data points in between. This is necessary in order to compute the reddening for each data point in a spectrum and therefore to be able to redden/deredden a spectrum. For the cubic spline interpolation, a C++ code published by Tino Kluge² is used.

In the UV-part of the spectrum (< 2700 Å), interpolation is not necessary, but a set of equations is available to calculate the value of $A(\lambda)/E(B - V)$ directly for all wavelengths. The parameters for these equations were developed and calibrated by Fitzpatrick & Massa (1990). According to them, in $x \equiv 1/\lambda$ representation, the extinction curve can be written as a superposition of a linear term (Eq. 2.28), a Lorentzian-like profile (Eq. 2.29) which describes the UV-bump and a term for far-UV curvature (Eq. 2.30).

²<http://kluge.in-chemnitz.de/opensource/spline/>

$$\frac{A(\lambda)}{E(B - V)} = c_1 + c_2x + c_3D(x) + c_4F(x) + R \quad (2.28)$$

$$D(x) = \frac{x^2}{(x^2 - x_0^2)^2 + x^2\gamma^2} \quad (2.29)$$

$$F(x) = \begin{cases} 0.5392(x - 5.9)^2 + 0.05644(x - 5.9)^3 & \text{for } x \geq 5.9\mu\text{m}^{-1} \\ 0 & \text{for } x < 5.9\mu\text{m}^{-1} \end{cases} \quad (2.30)$$

In this work, only the $R = 3.1$ case is considered. The $E(B - V)$ value is taken from the Schlegel et al. (1998) maps.

Fig. 2.8 shows the application of the procedure described above to a solar-like spectrum ($T_{eff} = 5700K$, $\log g = 4.7$, solar metallicity). The flux in the UV is strongly damped, which especially modifies the shape of the spectrum. The reddening of objects in the galactic disk can be even larger than the ones of the depicted spectra ($E(B - V) \sim 10$). However, this work does not deal with strong reddening since SDSS mostly contains objects at high galactic latitudes which show only a slight reddening ($E(B - V) < 0.1$). In order to achieve the most accurate estimates for the atmospheric parameters, reddening is nevertheless taken into account.

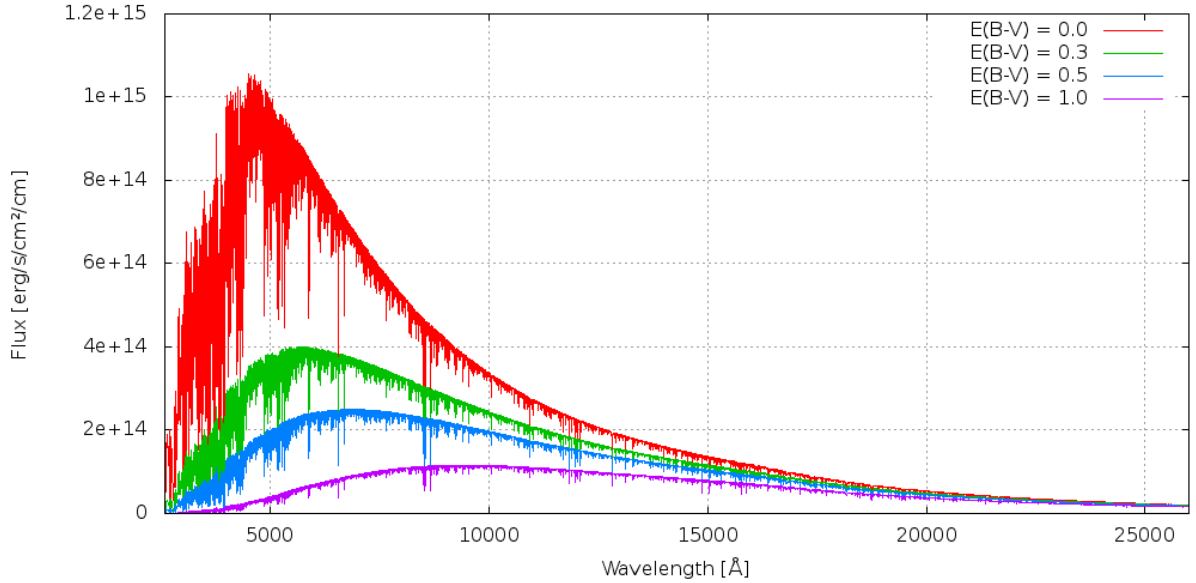


Figure 2.8: The effect of interstellar extinction on a solar-like spectrum ($T_{eff} = 5700K$, $\log g = 4.7$, solar metallicity) for different values of $E(B - V)$ using the reddening procedure according to Fitzpatrick (1999). The flux in the UV is strongly damped.

Note, that modifying observations should usually be avoided. However, it makes no difference whether the extinction curve is used to redden the synthetic binary spectra in every iteration or to deredden the observation. Therefore, in order to optimize the computation time, the latter option is implemented.

2.8 Technical implementation

Putting together all building blocks described above is essentially enough for the fit routine to work as desired. However, some parts, like the convolution for instance, need to be adapted to be numerically efficient. Furthermore, even though computers are getting faster, it is necessary to think about the execution time of a piece of code and how to improve it. Also the management of the finite memory is an important task. These rather technical issues are discussed in this chapter. Fig. 2.9 gives a complete overview of the process.

2.8.1 Spectral grids and memory management

When the code is started, both grids are scanned for available spectra. In the course of this, the libraries are initiated in the code. Note, that at this point the spectra themselves are not read, but only their parameters. Both grids span over more than a few gigabytes, which cannot be stored in the RAM-memory³ available on a current desktop computer. Subsequently, the simplex fit routine is started. As the fit routine requests the synthetic composite spectrum of a given combination of parameters in order to compare it to the observation, both library instances receive a request to produce a single-star spectrum with the given parameters as described in Sec. 2.3. All spectra required for this are read into the RAM and convolved numerically (see Sec. 2.8.2) to match the resolution of the observed spectrum. Also, the wavelength data points are taken from the observed spectrum. This is, not to touch and process the observational data but only the synthetic spectra. Subsequently, a synthetic binary spectrum is composed by combining both single-star spectra. The fluxes are added according to Eq. 2.20.

The spectra of all surrounding grid nodes are now stored readily convolved in the RAM. If, in some of the next iterations, one of the spectra is requested again, the library instance recognises that the grid node is already stored in the RAM. Therefore it is redundant to read and convolve the spectrum again. The spectrum is immediately available for grid interpolation.

This means, that over time, a huge fraction of both libraries is available for fast access in the RAM. However, this does not mean that tenths of gigabytes of RAM is necessary in order to run the code since only the convolved synthetic spectra but not the high-resolution templates are stored. Therefore, in order to fit a typical low-resolution observation (FWHM $\sim 1 \text{ \AA}$) only approximately 0.5-1 gigabytes of RAM are necessary.

Going one step further considering processing larger samples from the same instrument in an automated way, the availability of large fractions of the grids in the RAM yields an extensive time boost.

³The RAM (random access memory) is available for active jobs on the computer to store data for fast access. Also the writing speed in the RAM is significantly faster than on a standard hard drive or even a solid state drive. The amount of RAM available on a current computer is a few gigabytes.

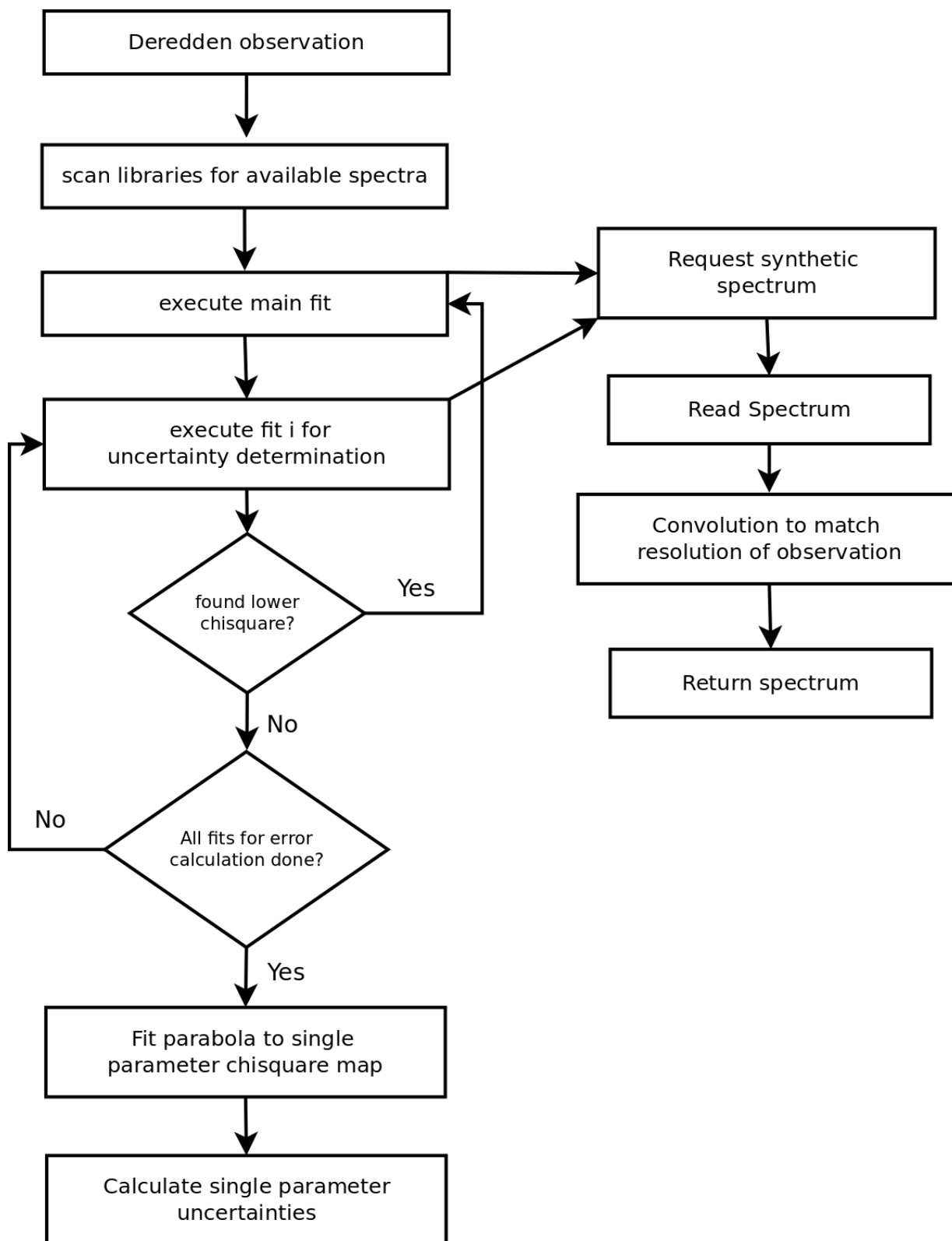


Figure 2.9: Flowchart of the binfit-code, including error calculation and the access to the spectral libraries (right column).

2.8.2 Numerical convolution

The convolution is defined as a continuous integral (see Eq. 2.10). This can also be written in form of a discrete sum, thus making the problem solvable in a numerical way. The indices i denote the data points in the spectrum.

$$(f * g)[i] = \sum_{j=-\infty}^{\infty} f[j] \cdot g[i - j] \quad (2.31)$$

In order to apply this, also the broadening function $g(x)$ has to be discretized. Remember, that $g(x)$ was chosen to be a Gaussian function, having the width of the instrument's intrinsic profile. First, $g(x)$ is sampled in 81 data points (denoted by j). These are evenly spaced within the 3σ region of $g(x)$. Only 0.26% of the Gaussian are not in this region. Therefore, this outer part does not contribute significantly to the convolution. The number of 81 data points was found to be a good trade-off between precision and computing speed (see Sec. 3.1).

Note, that we do not want to modify observations, therefore, the library spectra are convolved onto the wavelength scale and the resolution of the observation. Subsequently, for each wavelength data point $\lambda[i]$ in the observed spectrum ("target wavelength scale") Eq. 2.31 is evaluated at $f[i]$ in the synthetic spectrum.

$$(f * g)[i] = \sum_{j=-40\cdot\text{inc}}^{40\cdot\text{inc}} f[j] \cdot g[i - j] \quad (2.32)$$

"inc" denotes here the increment which is necessary to cover the 3σ region of $g(x)$. Typically, the sampling of $g[i - j]$ is finer than the sampling of the data points in the synthetic spectrum $f[j]$. Therefore, linear interpolation is applied between data points of the synthetic spectrum in order to calculate the corresponding $f[j]$ to match the sampling of $g[i - j]$. The numerical convolution code used in this project can be found in App. A.2.

2.8.3 Boundaries of the spectral grid

Since the parameter coverage of the grids is not infinite, the routine needs a mechanism to prevent the fit algorithm from moving the simplex into regions not covered by the grids. This should be done in a smooth way. Throwing an error is not an option, since the fit would then stop immediately and needs to be restarted by hand.

A nice way to prevent the simplex from moving into forbidden regions is to use intrinsic properties of the fit algorithm. If the χ^2 gets worse in this region, the simplex would automatically omit moving further into this direction but will reject or not accept the vertex outside the boundaries. Therefore, the spectrum of one of the components is modified if one of the parameters are out of the grid boundaries: the flux of the spectrum immediately drops to zero. The spectrum of its companion is still non-zero. This yields a smooth but steep increase in the χ^2 map without any discontinuities at the boundaries of the grid.

Summary

- The aim of this project is to disentangle sd + F/G/K binaries making use of the techniques of quantitative spectral analysis.
- The code makes use of the pre-calculated spectral libraries for both components in order to reduce calculation time. Three dimensional linear interpolation is used to explore the regions in between gridpoints.
- Function minimization is performed by a standard downhill simplex routine, making use of χ^2 as a measure of the goodness of the fit. The uncertainties are determined by χ^2 statistics.
- In order to improve the expected bad convergence of the surface gravities, the gravities are linked to the surface ratio and the masses of both stars. The mass of the subdwarf is fixed to the canonical mass 0.48, the mass of the cool companion is treated as an additional fit parameter, but restricted to the range between 0.7-1.5 M_{\odot} .
- For given interstellar extinction $E(B - V)$, the code is able to correct for reddening due to interstellar extinction during the fit.
- The parts of the spectral grid which have been used during the fit are stored in the RAM as long as possible. They are, if needed again later, available in a readily convolved manner, yielding an extensive boost in computing time.
- If the fit tries to overcome the boundaries of one of the spectral grids, the χ^2 is driven to bad values in order to prevent the fit from leaving the parameterspace. This is achieved, by setting the corresponding spectrum to zero flux.

3 Proof of concept

The development of a code from scratch without the use of any external packages requires extensive testing, because even though as much care as possible is taken during the process of writing the code, some bugs and failures only show up at runtime. It is also important to estimate the calculation times and search for possible optimizations. The convolution routine, one of the most crucial parts for the calculation time, is tested in Sec. 3.1. Sec. 3.2 illustrates the impact of the convolution function on spectral lines. Furthermore, it is important to investigate how the code performs. Therefore, a synthetic spectrum of a mock binary with known parameters was fitted and the impact of the signal to noise level (S/N) of the spectrum on the results was studied. This is presented in Sec. 3.3.

3.1 Convolving 2 Gaussians

Converting operations which are mathematically defined as continuous integrals to discretized, numerical functions can lead to inaccuracies. In the case of the convolution, as described in Sec. 2.8.2, this could be caused by choosing too rough a sampling of the functions. As stated before, the numerical convolution is expensive with respect to calculation time and therefore a trade-off between accuracy and efficiency has to be made. This section shows, that the accuracy achievable with the chosen number of 81 data points is sufficiently high to be used to convolve spectra.

As an example, the convolution of two Gaussians is calculated with the code. Mathematically, the convolution of two Gaussians $g_1(x, \mu, \sigma_1)$ and $g_2(x, \mu, \sigma_2)$ is again a Gaussian, although not normalized.

$$g_1(x, \mu, \sigma_1) * g_2(x, \mu, \sigma_2) = G\left(x, \mu, \sqrt{\sigma_1^2 + \sigma_2^2}\right) \quad (3.1)$$

In order to estimate the accuracy of the convolution, two Gaussians $g_1(x, 0, 1)$ and $g_2(x, 0, 2)$ are convolved with the convolution code. g_1 is sampled with 1000 data points from -10 to 10. g_2 is sampled with 81 data points within its 3σ range, as described in Sec. 2.8.2. The result is then fitted using a standard Gaussian function with *gnuplot*¹. Fig. 3.1 shows the result. The expected σ of the convolution is 2.236, according to Eq. 3.1. According to the fit, the resulting σ is 2.234, which is close to the expected value. This shows, that the sampling rate of g_2 is sufficient. In order to achieve a higher accuracy, the sampling needs to be improved which has a huge impact on the computing time.

¹<http://www.gnuplot.info/>

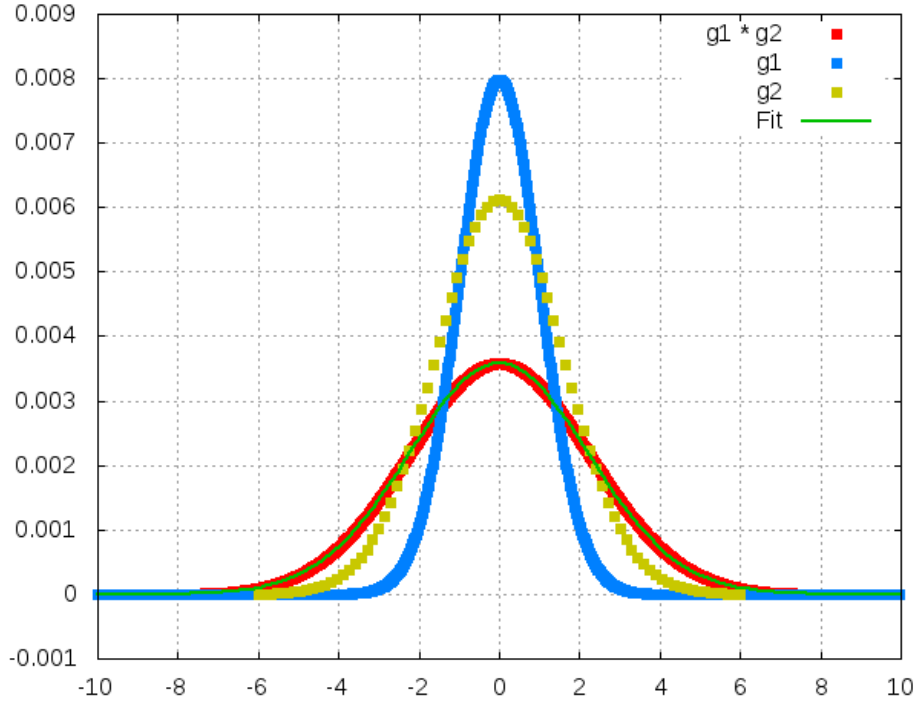


Figure 3.1: Convolution of two Gaussian functions (blue $\sigma = 1$ and brown, $\sigma = 2$). The fit gives $\sigma = 2.234$ which is sufficiently close to the expected $\sigma_{exp} = 2.236$. All Gaussian functions are plotted with arbitrary normalization.

Thinking about the application of this method to spectra a Gaussian function will be convolved with the spectrum itself. Therefore, this proof is only valid if a sufficiently large number of data points of the spectrum are located within the 3σ range or the 81 data points around the maximum of the Gaussian, respectively. In this code, the high resolution spectral libraries (Phoenix: $R = 500000$ in the optical) are convolved to a lower resolution, which means that the Gaussian function is wide compared to the sampling of the spectrum and, therefore, the criterion mentioned above is fulfilled.

3.2 Convoluting spectral lines

Applying a convolution with a Gaussian of given width σ to a spectrum can from a physical point of view be interpreted as taking a spectrum with a spectrograph where the instrument's broadening profile is a Gaussian with width σ . This simulates therefore the instrument's finite resolving power. In order to demonstrate the impact of the convolution on the spectrum Fig. 3.2 shows a part of a synthetic spectrum from the Phoenix library (see Sec. 2.2.2) convolved with Gaussians of different width.

The line shape changes strongly between the different resolutions. For lower resolutions, the lines get smeared. They appear broader and less deep. The $\Delta\lambda = 2.5 \text{ \AA}$ example is

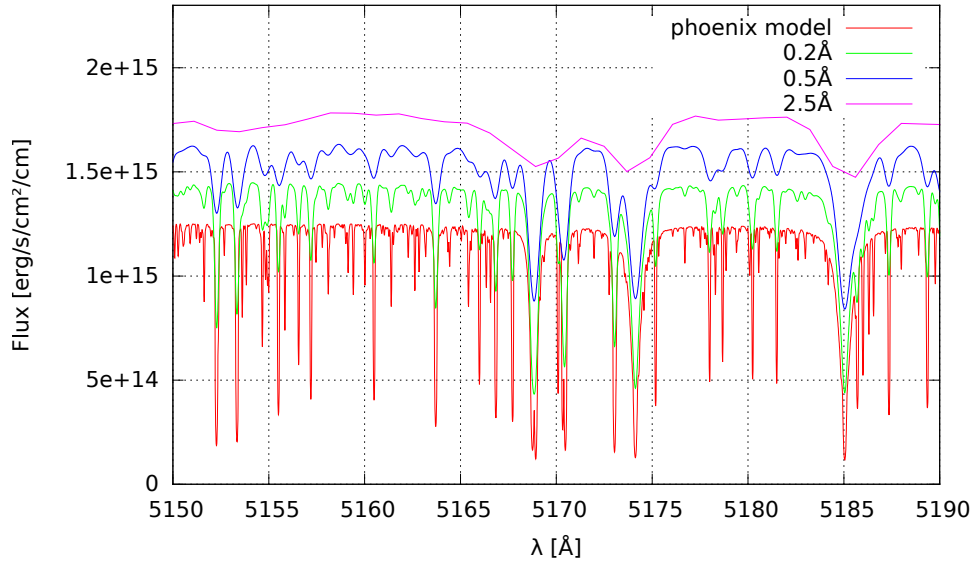


Figure 3.2: Phoenix model spectrum convolved to different FWHM. The figure shows the Mg triplet of a $T_{eff} = 6100\text{K}$, $\log g = 4.0$ star. The metallicity is solar. Especially the comparison between the original spectrum (red) and a spectrum convolved to a Gaussian with FWHM close to SDSS spectra (magenta) shows that many features are smeared out due to the detector’s finite resolution.

plotted in addition, because it is close to the resolution of SDSS spectra. Many narrow features cannot be used directly for fitting due to the detector’s finite resolution. They are in principle still present in the spectrum but smeared out strongly. This example shows that the convolution is a very crucial part in fitting spectra.

Some types of spectrographs (like Echelle spectrographs) have a wavelength independent resolution $R = \frac{\lambda}{\Delta\lambda}$. Especially spectra from the SDSS and BOSS spectrographs can have wavelength dependent R . This needs to be taken into account as precisely as possible. See Sec. 4.2.2 for details on the SDSS resolution pattern and the treatment of the wavelength dependent resolution.

3.3 Error estimation based on synthetic spectra with artificial S/N

In order to test the functionality of the code, the spectrum of a mock binary system was fitted. The binary system was chosen such that both components contribute significantly to the flux in the chosen wavelength range. Reddening was neglected. The binary spectrum was generated with a completely independent code in order to serve as an independent test case. The template spectra for the mock binary system are taken from the same libraries which were used to fit the spectrum. The spectral range is chosen as large as possible and is therefore restricted by the spectral coverage of the subdwarf grid of synthetic spectra (3120-7530 Å, See Sec. 2.2.1).

The spectrum was convolved to a constant resolution of $\Delta\lambda = 2.5 \text{ \AA}$ to be close to the planned application of the code, that is fitting low resolution spectra from SDSS. Furthermore, random noise was artificially added to the spectrum to mimic different S/N, using the equation

$$F_i^{\text{noise}} = F_i + \frac{r \cdot F_i}{\text{S/N}} \quad (3.2)$$

where r is a random number between 0 and 1. Different S/N values were used to estimate the achievable accuracy and to estimate the impact of the S/N on the results. This method was carried out on two examples, one example with many lines ("Example 1") and one more sophisticated case with less lines ("Example 2") and therefore higher degree of degeneracy.

3.3.1 Example 1

The parameters chosen for both components are given in Tab. 3.1. The surface ratio is set to 20.8, the inferred mass of the cool companion is expected to be $0.96 M_{\odot}$ and the resolution is $\Delta\lambda = 2.5 \text{ \AA}$. Note, that due to the chosen solar metallicity, many metal lines are present in the spectrum of the cool companion. Also, a low temperature for the hot subdwarf in combination with a high helium content allows the fit routine to use more lines to fit the subdwarf spectrum. The spectrum and the fit is depicted in Fig. 3.3 for the S/N = 100 case.

MS			sdB		
T_{eff}	$\log g$	$\log [\text{Fe}/\text{H}]$	T_{eff}	$\log g$	$\log [\text{He}/\text{H}]$
6000 K	4.5 dex	0 dex	25000 K	5.5 dex	-1.5918 dex

Table 3.1: Parameters used for the generation of the mock binary spectrum before adding artificial S/N.

The reduced χ^2 of all fits should be close to 1, because the added S/N is exactly known and can be used as an input to the fitting routine. The values are summarized in Tab. 3.2. The reduced χ^2 increases slightly, as the S/N of the spectrum increases. This can be interpreted as the quality of the data and therefore the S/N has been overestimated for the fit, but since the spectrum was self-generated, we should know the exact value of the S/N. A possible explanation for this effect is the high sensitivity of the reduced χ^2 to slight deviations for high S/N spectra, because the fit did not reach the exact position of the minimum (the termination criterion prevented the fit from reaching it). Remember, that the criterion introduced in Sec. 2.5.3 only depends on the quadratic deviation of the χ^2 values at each simplex vertex from the mean χ^2 . Furthermore, the accumulation of errors due to the finite numerical precision and the slightly different methods for creating and analyzing the spectrum may play a role in this context. Of course, the latter effect is expected to be most visible in high S/N data.

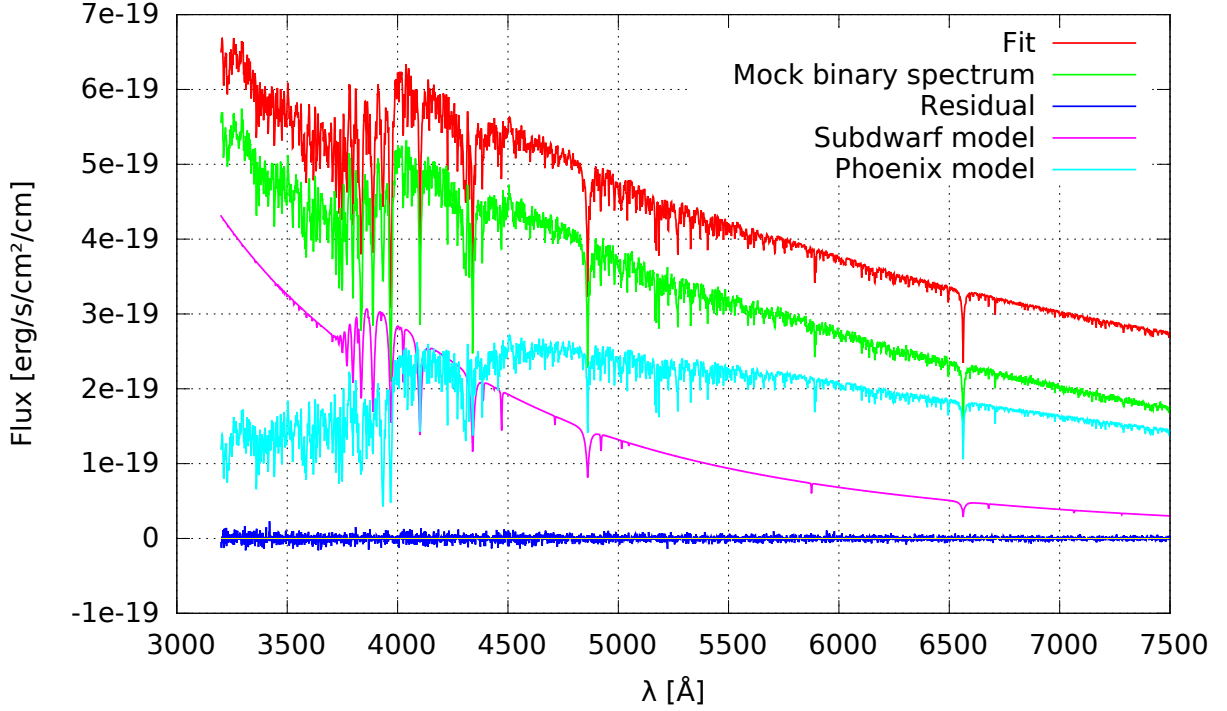


Figure 3.3: Spectrum and the corresponding best fit for the $S/N = 100$ case of Example 1. The fitted spectrum is shifted up for clarity. $\chi^2_{red} = 1.1323$.

S/N	25	75	50	100
χ^2_{red}	1.0327	1.0465	1.0823	1.1323

Table 3.2: χ^2_{red} of all fits for Example 1. The deviation from $\chi^2_{red} = 1$ for high S/N can be explained by the high sensitivity of χ^2_{red} to slight deviations for higher S/N due to the application of slightly different methods for generating and analyzing the spectrum.

Since the parameters of the mock binary system are known well they can be directly compared to the results in Fig. 3.4. For all parameters, there is good agreement with the determined values, independent of the S/N.

The most important lesson learned from Fig. 3.4 is, however, the size of the errorbars for different S/N ratios. Basically, in this test case the size of the errorbars is affected by

- S/N
- Spectral resolution
- Degeneracies between parameters
- Numerical precision

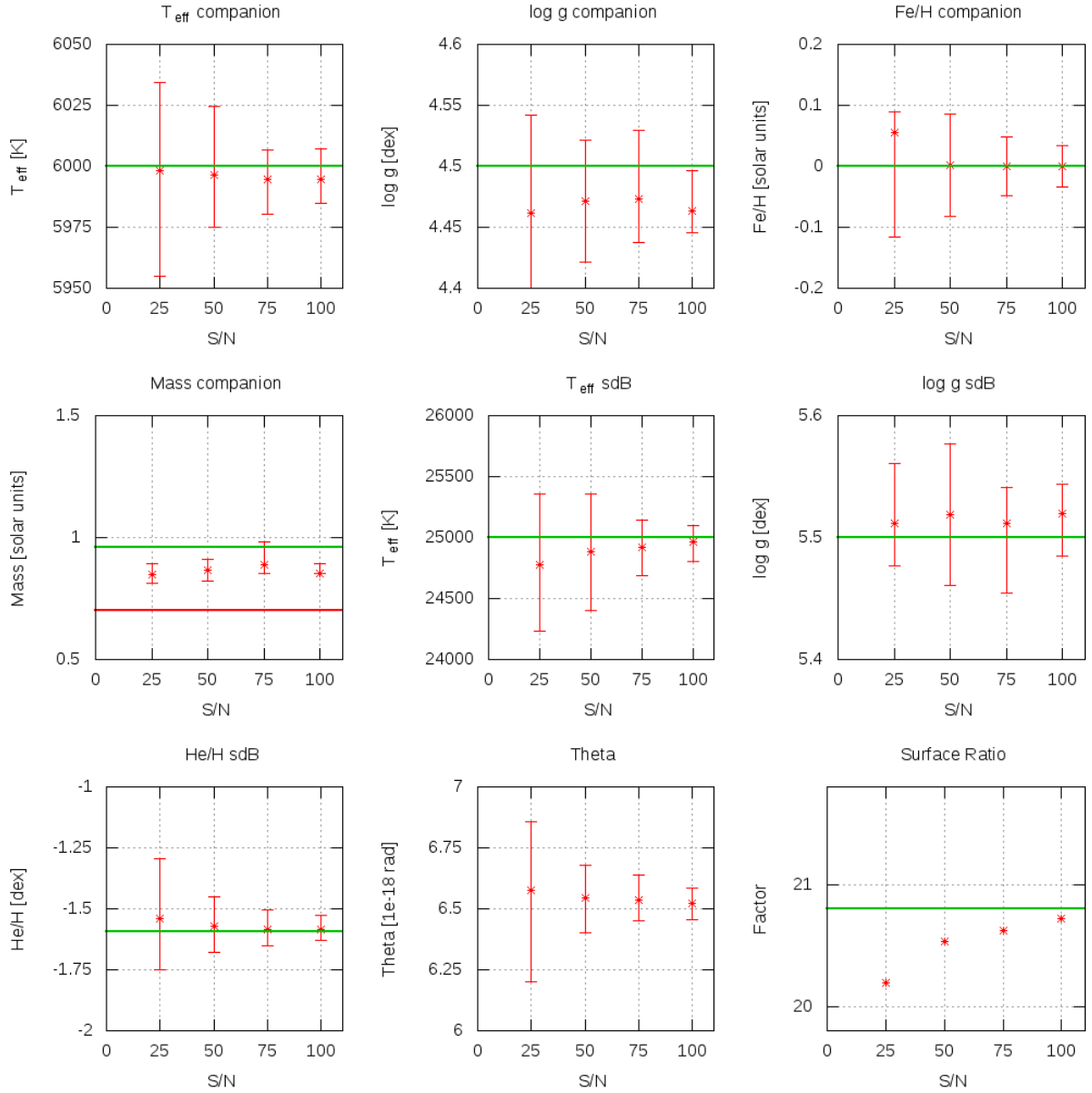


Figure 3.4: Parameter and uncertainty determination on the mock binary spectrum (Example 1) with different artificial S/N ($S/N = 25, 50, 75, 100$) added. The spectrum was convolved to $\Delta\lambda = 2.5 \text{ \AA}$. The true parameters of the mock binary system are given in Tab. 3.1. Green lines show the value which was used to generate the synthetic spectrum, red lines show constraints for the parameters. The graphic shows uncertainties in terms of 99% confidence limits. See text for discussion.

, where the latter one is almost negligible. The higher the S/N, the more features should be recognized by the fit routine. The uncertainty should therefore drop with increasing S/N. This general trend can be observed in all panels of Fig. 3.4. However, the uncertainties drop significantly faster for some parameters than for others. The temperatures as well as the angular diameter θ and the helium abundance are well constrained for high S/N, while

surface gravities remain unconstrained. This effect is due to a strong correlation between the surface gravities of both components, yielding a flat valley in the χ^2 landscape (see Sec. 3.4). The mass of the cool companion is not consistent with the expected value, even within the 99% confidence limits. However, this is not unexpected since the mass as a free parameter and was introduced to put constraints on the surface gravities of both components by linking them via the surface ratio (see Sec. 2.5.2). The use of the mass restriction was not necessary in this example, as seen in Fig. 3.4, where the mass range limit is indicated by a red line in the corresponding panel. A slight change in surface gravity $\log g$ has a huge impact on the inferred mass due to the logarithmic scale. Therefore, the outcome for the mass is not expected to be very precise.

The distribution of $\Delta\chi^2$ around the best fit which is determined by keeping one parameter fixed and fitting all others is shown in Fig 3.5 for the S/N = 100 case. It was used to determine the uncertainties. However, it is also instructive to look at it in detail in order to get a feeling for the complexity of the problem. Looking at the temperature, metallicity, helium abundance panels reveals a nicely behaving χ^2 landscape which is well approximated by the quadratic fit. However, the surface gravity panels show two very steep minima. In between those minima, χ^2 raises to high values (> 1000 for the S/N 100 case). This effect is observed independent of the S/N. Close investigation of the best-fitting spectra for fixed gravities in the region in between the minima revealed a problem close to the Balmer jump region and in some Balmer lines (see App. B.1). Fitting the spectra excluding the problematic region reduced the height of the wall in between both minima but it was still present in the data. As the simplex algorithm is also not fail-safe regarding local minima, one of the reasons for the steep increase in χ^2 might be a local minimum, which is reached from special starting conditions (specific values of $\log g$) only. However, from a physical point of view the existence of two minima is also explainable. Pressure broadening of spectral lines can either be modeled in the spectrum of the subdwarf or in the spectrum of its cool companion. Therefore, a symmetric but mirrored χ^2 distribution around the best fit for both surface gravities as observed is not unlikely, because either a higher $\log g$ of the subwarf and a lower $\log g$ of its companion or the vice versa combination may produce similar results. Another possibility may also be artefacts in one of the spectral libraries which do not necessarily have to show up while stepping through different surface gravities. The fit for each of the data points in the χ^2 lines may drive the fit far away from the best fit, because each but the stepped parameter can change freely. The fundamental reason for this effect remains unclear and has to be investigated in the future. If the effect is due to the simplex getting stuck in local minima using other fit algorithms or switch to genetic codes might help (see Sec. 5.1.2).

Nevertheless, the panels show explicitly, that the procedure described in Sec. 2.8 is able to find the global minimum and that the simplex did not get stuck in the second, local one. This is ensured by stepping the χ^2 landscape around the best fit while determining the uncertainties as described in Sec. 2.6.2. Remember, that the curves depicted in Fig. 3.5 are used to estimate the uncertainty of the parameters of the fit by evaluating where $\Delta\chi^2_{red} = 6.63$ - this is corresponding to the 99% single parameter confidence interval. The shapes in Fig. 3.5 justify the choice of fitting a parabola to the depicted lines in order

to derive the value where $\Delta\chi^2 = 6.63$ and, thus, to find the uncertainty. Just stepping through the $\Delta\chi^2$ distribution until $\Delta\chi^2 = 6.63$ would especially for the surface gravities yield a wrong estimate for the uncertainty and prevent the routine from recognizing the second minimum. The stepped region and the number of steps which are plotted in Fig 3.5 and used for the uncertainty calculation are chosen by hand.

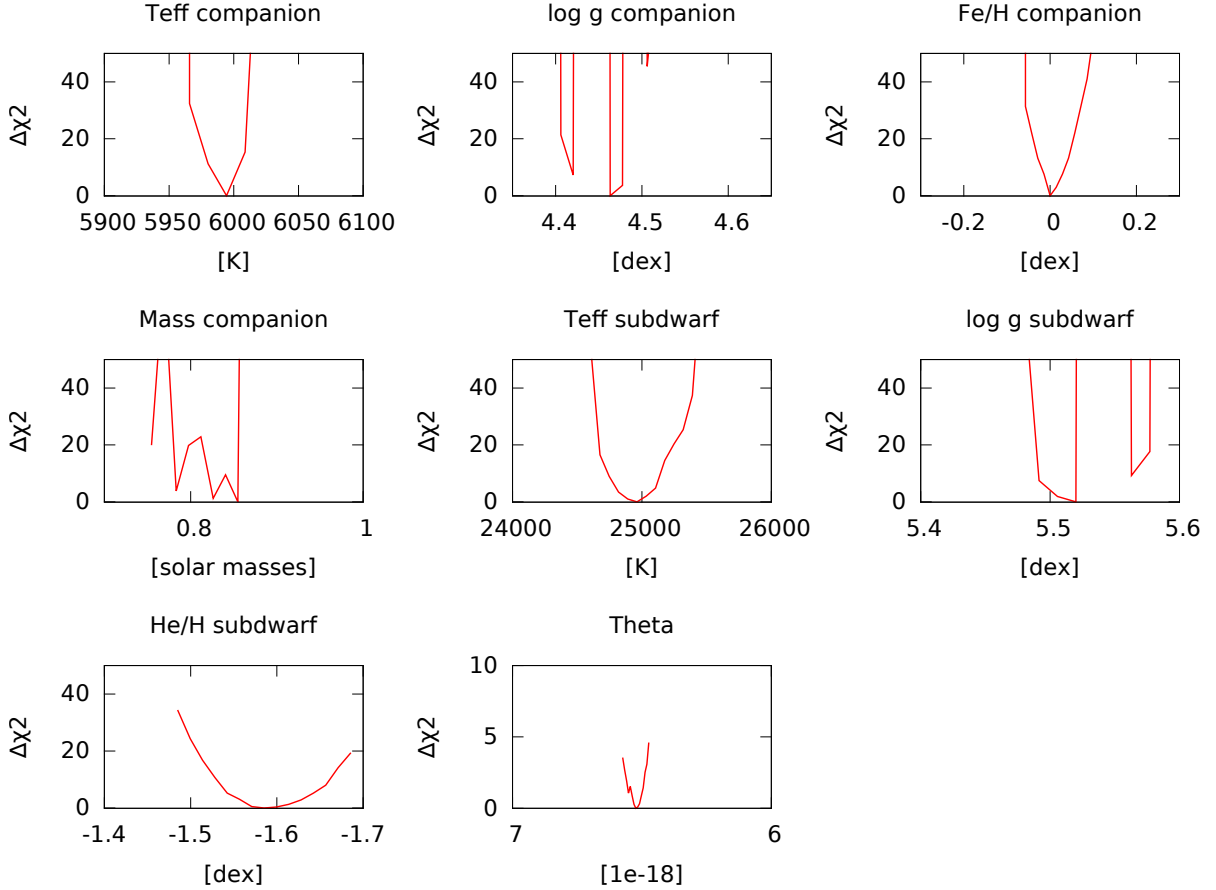


Figure 3.5: $\Delta\chi^2$ single parameter lines around the best fit for Example 1. Some of the parameters show a highly complicated pattern in their $\Delta\chi^2$ line with several local minima. The steep raise in the $\log g$ lines may have physical or numerical reasons. See text for discussion.

The given uncertainty ranges can be interpreted as estimates of the achievable accuracy using the code developed in the course of this project. However, this may depend on the physical parameters of fitted binary systems, as seen in Example 2.

3.3.2 Example 2

The parameters chosen for both components are given in Tab. 3.3. The surface ratio was set to 30, the inferred mass of the cool companion is expected to be $1.44 M_{\odot}$. The lower metallicity of the cool companion compared to Example 1 yields less and weaker lines to be

present in the spectrum. Furthermore, the temperature of the subdwarf was increased and its helium content decreased. The subdwarf spectrum, therefore, also has less and weaker lines than in the previous example. Due to possible degeneracies it is more challenging to fit this binary spectrum, because it has less features. The spectrum and the corresponding fit is depicted in Fig. 3.6 for the $S/N = 100$ case.

MS			sdB		
T_{eff}	$\log g$	$\log [Fe/H]$	T_{eff}	$\log g$	$\log [He/H]$
6000 K	4.5 dex	-1.5 dex	35000 K	5.5 dex	-2.7959 dex

Table 3.3: Parameters used for the generation of the synthetic binary spectrum before adding artificial S/N.

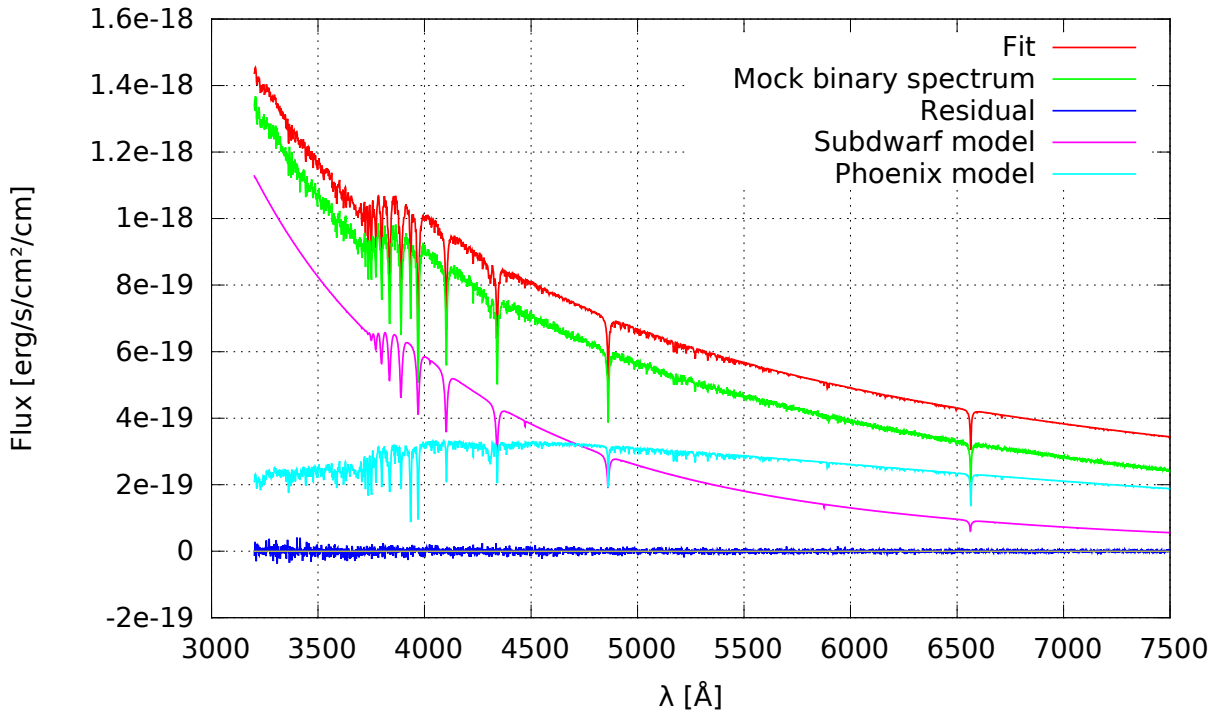


Figure 3.6: Spectrum and the corresponding best fit for the $S/N = 100$ case of Example 2. The fitted spectrum is shifted up for clarity. $\chi^2_{red} = 1.03978$.

Looking again at the evolution of χ^2_{red} with increasing S/N, no behaviour like in Example 1 can be observed (See Tab. 3.4). However, here the values don't raise to the high values in Example 1 for high S/N. The reason for this might be that there are fewer lines in the spectrum and therefore the differences between the fit of the continuum and the mock binary spectrum are in average smaller. This yields a lower χ^2 and therefore also a lower

S/N	25	50	75	100
χ^2_{red}	1.02906	1.0465	1.03229	1.03978

Table 3.4: χ^2_{red} of all fits for Example 2.

χ^2_{red} compared to the case with many spectral lines when the stopping criterion is fulfilled. Furthermore, numerical differences between generating and analyzing the spectrum mostly show up in spectral lines and, therefore, this example is not expected to be as affected as Example 1.

Again, the general trend observed in Fig. 3.7 is that the higher the S/N, the smaller the errorbars. It turns out that due to the less intense and abundant features in the spectrum the metallicity and the helium abundance have larger uncertainties. However, the temperature of the cool companion is constrained as well as in Example 1. Interestingly, the temperature of the subdwarf as well as its surface gravity differ from the expected values for higher S/N. For some datapoints, even the uncertainties are too low. If this is due to a degeneracy, the uncertainties are expected to reflect this fact by appearing to be larger. However, the surface gravities showed also a similar behaviour as in Example 1. There may be a correlation between surface gravities and temperatures. Therefore, it is instructive to again have a look on the $\Delta\chi^2$ distribution around the best fit.

This is shown in Fig. 3.8. We again see complicated patterns, but also wider distributions compared to Example 1. In addition to the depicted S/N = 100 case, App. B.2 also shows the S/N = 75 case for inspection. Especially the helium abundance is completely unconstrained at these low values in combination with the low resolution. Looking at the panels for the surface gravities reveals a similar behaviour than in Example 1. However, the corresponding values for the S/N 75 and S/N 100 case in Fig. 3.7 were clearly off. This may be due to the existence of the two local minima which are clearly visible in Fig. 3.8. Furthermore, the determination of the uncertainties might also be affected by the artefacts where the χ^2 increases dramatically. Since values with too high $\Delta\chi^2$ are not used for the parabola fit during the uncertainty determination ($\Delta\chi^2 > 100$ is ignored) this parabola fit is quite uncertain due to a lack of data points. This is most probably the reason for the uncertainties in Fig. 3.7 being underestimated. Probably a better sampling of the χ^2 in combination with a lower cut-off for the χ^2 data points included in the parabola fit might produce better results.

Comparing both examples shows the expected behaviour. The fit does not improve significantly for S/N values larger than 75 and even the S/N = 25 case produces reliable results for most parameters at least in Example 1. The uncertainties of Example 2 are, of course, much larger. That means, that an observed spectrum with a S/N = 25 is - depending on the physical parameters of the binary - sufficient to constrain parameters. The higher the S/N of the spectrum, the lower the uncertainties. Furthermore, these examples are chosen to be as close to SDSS data as possible, especially regarding the resolution. Fortunately, SDSS typically provides spectra with $25 < S/N < 50$ for 16-18 mag objects.

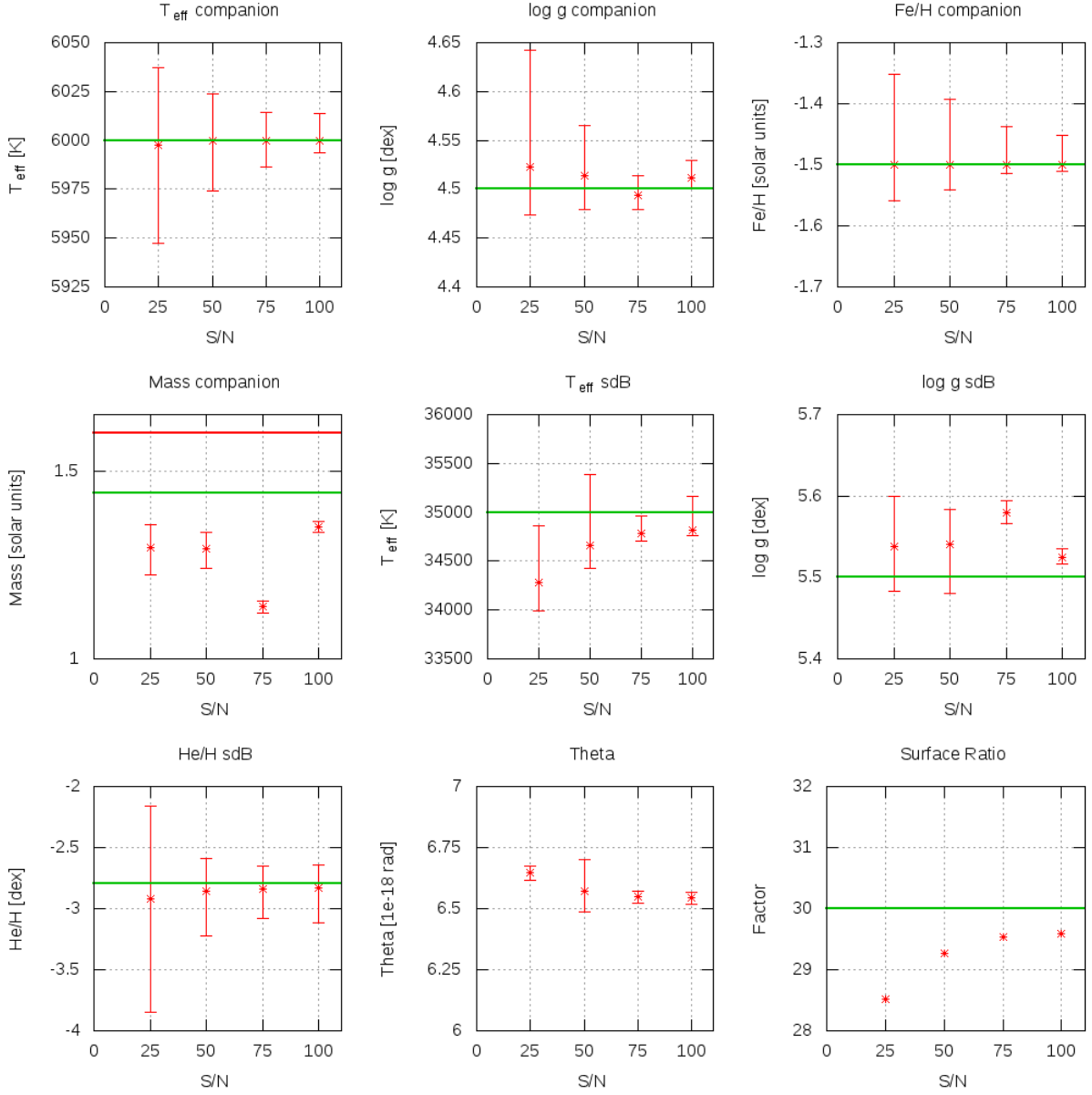


Figure 3.7: Parameter and uncertainty determination on the mock binary spectrum (Example 2) with different artificial S/N ($S/N = 25, 50, 75, 100$) added. The spectrum was convolved to $\Delta\lambda = 2.5 \text{ \AA}$. The true parameters of the mock binary system are given in Tab. 3.3. Green lines show the value which was used to generate the synthetic spectrum, red lines show constraints for the parameters. The graphic shows 99 % confidence intervals. See text for discussion.

Therefore, SDSS spectra are sufficient to find the atmospheric parameters of a hot subdwarf binary with the code developed in the course of this thesis. Working with higher resolution spectra will decrease the errorbars further.

Note, that the given uncertainties are statistical uncertainties. Especially the uncertainty introduced by calculating the model grids is not considered because it is, due to its nature,

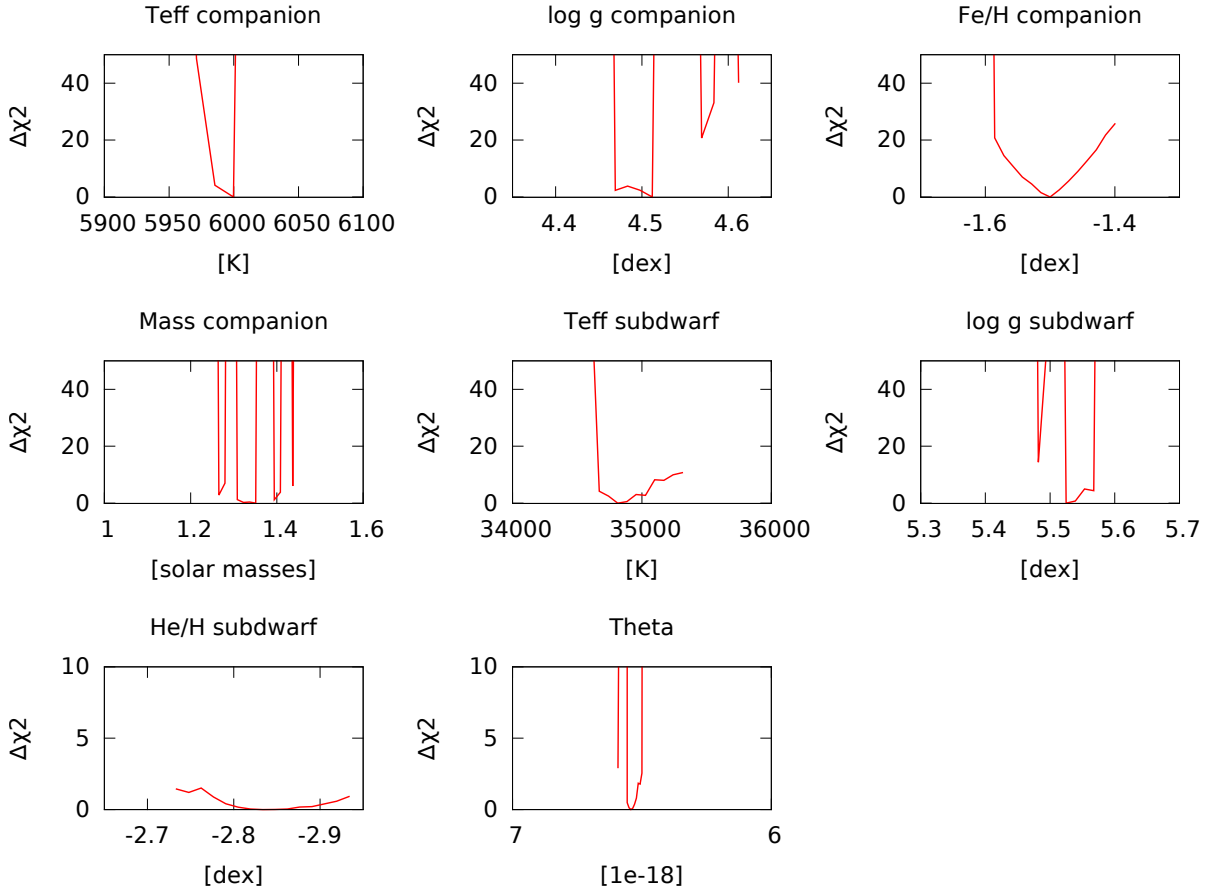


Figure 3.8: $\Delta\chi^2$ single parameter lines around the best fit for Example 2 for the S/N = 100 case. Some of the parameters show a highly complicated pattern in their $\Delta\chi^2$ line with several local minima.

unknown. In literature, often a constant uncertainty on the order of a few per cent is added to the statistical uncertainty of the fit. In this work, systematic errors are neglected.

Another interesting quantity is the amount of computing time needed. One single fit with the given resolution including the uncertainty calculation is below 24 hrs on one single core of a state-of-the-art desktop computer. This is of course depending on the CPU but also on how often the uncertainty calculation is restarted, because a lower χ^2 and therefore a better fit was found (See Sec. 2.6.2). The number of restarts is usually between 0 and 10, yielding a wide range of possible computing times from a few hours up to the 24 hours already mentioned as upper limit for the fits in the example above.

It should be emphasized that this section presented a test of the complete code (without accounting for reddening) using an independently generated mock binary spectrum. It therefore shows the internal consistency of the code and serves as a proof of concept. The application to real targets is discussed in the next section.

3.4 Correlations

Some of the parameters are expected to be correlated. This means, that changes in the fit caused by stepping one parameter during the uncertainty calculation can be compensated by another parameter to some extent. Increasing one may lead to an increase or decrease of another parameter while χ^2 is still close to the value at the best fit. This effect yields flat valleys in the χ^2 landscape and leads to degeneracies of parameters. Fig. 3.9 shows the χ^2 landscape around the best fit for the S/N 50 case of Example 1 from Sec 3.3 for all pairs of parameters in terms of $\Delta\chi^2_{red}$. Each panel was generated by stepping the 2 parameters of interest and fitting all others.

The maps show that the χ^2 landscape is not smooth at all but contains several small minima and maxima. It, furthermore, reflects the uncertainties determined in Sec. 3.3. Correlations between two parameters show up in Fig. 3.9 in form of diagonal valleys in the χ^2 landscape. Only horizontal or vertical connections are due to the uncertainty of just one of the parameters. Some parameters, like the mass of the cool component for instance, is almost unconstrained. Correlations can be seen between both temperatures and the angular diameter θ . The cooler the stars, the closer they have to be in order to provide the observed flux and therefore the larger θ . Another strong correlation is seen between the surface gravities of both stars. Note, that the resolution of the χ^2 maps is probably too rough to be able to recognize the huge drops in χ^2 in the case of the surface gravities as seen in Sec. 3.3.

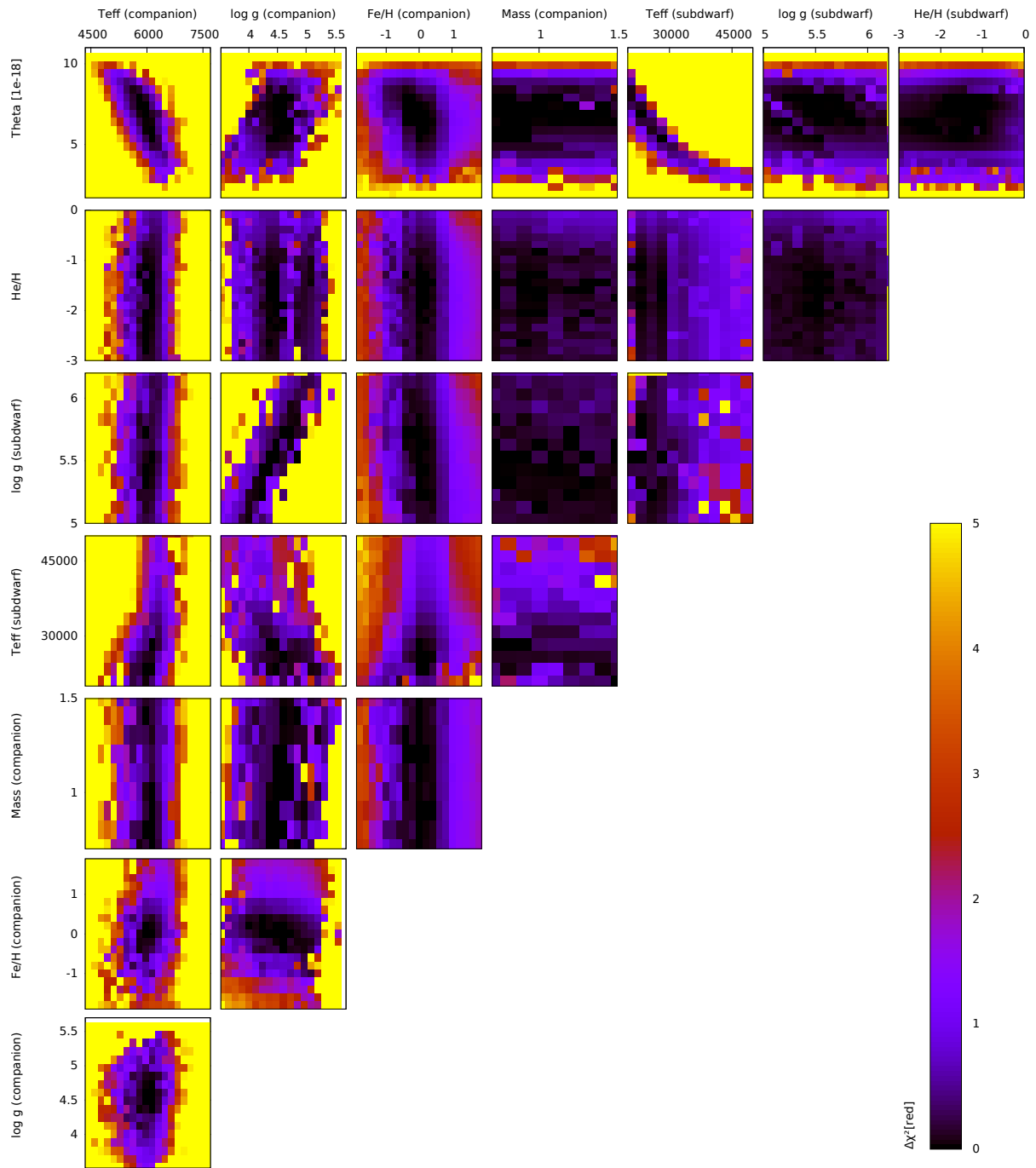


Figure 3.9: $\Delta\chi^2_{red}$ maps for the S/N = 50 case of Example 1. Some parameters show strong correlations, note especially the correlation between the surface gravities of both stars.

Summary

- The chosen implementation of the convolution is a good trade-off between accuracy and computation time.
- Fits of synthetic spectra produce the expected results for the free parameters. $\Delta\chi^2_{red}$ is sufficiently close to 1 in all cases.
- The uncertainty-S/N dependence shows that $S/N \sim 25$ is sufficient to constrain parameters - depending on the physical properties of the system. This shows, that it is possible to disentangle spectra provided by SDSS ($S/N > 25$) with the code developed in the course of this thesis.
- In the case of the surface gravities χ^2 shows two minima separated by a wall in between them. Whether the reason is a physical or a numerical discrepancy remained unclear.
- The calculation time for one single fit including the uncertainty calculation is below 24 hrs on one single core for $\Delta\lambda = 2.5 \text{ \AA}$ using the full available wavelength coverage.
- The χ^2 landscape of the problem turns out to be not smooth but contains several local minima. Most prominent is a strong correlation between the surface gravities of both stars and correlations between the temperatures and the angular diameter θ .

4 Applications

4.1 Testcase PG1104+243

In order to be able to compare the results achieved with the code to other approaches, the candidate PG1104+243 which was extensively investigated by Vos et al. (2012) was fitted.

4.1.1 The Object

Vos et al. (2012) found in the course of a long-term monitoring program of composite subdwarf binaries, that PG1104+243 is a sdB + G0 system. They used 38 spectra taken over a two years baseline with HERMES at the Mercator telescope (La Palma) to solve the orbit and provided accurate atmospheric parameters. The latter ones were determined by fitting the spectral energy distribution (SED). All parameters are summarized in Tab. 4.1. PG1104+243 is one of the first long period sdB binaries analyzed in detail.

		sdB	
P [d]	753 ± 3	T_{eff} [K]	33520 32400-34800
e	< 0.002	$\log g$ [dex]	5.81 5.77-5.85
K_{sdB} [km s ⁻¹]	6.9 ± 0.2	He/H [dex]	-1.52 (fixed)
K_{G0} [km s ⁻¹]	4.42 ± 0.08	G0	
q	0.64 ± 0.01	T_{eff} [K]	5931 5769-6095
		$\log g$ [dex]	4.29 4.26-4.32
		Fe/H [dex]	-0.58 (-0.47)-(-0.61)

Table 4.1: Left: Orbital solution, obtained in 5000 Monte-Carlos simulations from spectroscopy. K is the radial velocity amplitude, q is the mass ratio of the binary system. Right: Atmospheric parameters of the stars, determined by SED fitting. The radius of both components was determined from $\log g$ and the masses. 95% probability intervals are given. From Vos et al. (2012).

The surface gravity $\log g$ in Tab. 4.1 could only be constrained when Vos et al. (2012) computed the radius and therefore the surface ratio of the stars from their masses and surface gravities, since photometry puts almost no constraints on the surface gravities. Their approach is also implemented in this project, as described in Sec. 2.5.2. Vos et al. (2012) also fitted the reddening of the binary using the SED. They determined a low value ($E(B-V) < 0.012$).

4.1.2 Spectral Fitting

This section presents the results of the spectral fitting of PG1104+243 using the code developed in the course of this project.

The reddening maps by Schlegel et al. (1998) with the correction from Schlafly & Finkbeiner (2011) give $E(B - V) = 0.0128 \pm 0.0006$ for the coordinates of PG1104+243. This is within the uncertainties of the freely fitted value of Vos et al. (2012) ($E(B - V) = 0.000 - 0.100$). The Schlegel-value is applied to deredden the spectrum before fitting.

A high-resolution spectrum based on 82 HERMES spectra (Raskin et al., 2011) was available. The high resolution of this spectrum confronted the code not only with a higher resource consumption but also with new physical effects, that were not taken into account up to now. One of the most obvious differences between the synthetic spectra and the observation was the presence of rotation ($\sim 10 \text{ km s}^{-1}$), which can be recognized easily by over-plotting the observation (which is in the rest-frame of the cool component) with synthetic spectra convolved to the corresponding resolution. Since the code is not able to deal with rotational broadening at this stage of development, two options remain: Either model the influence of rotational broadening by an additional Gaussian convolution (which is physically incorrect) or convolve the observation to lower resolution where rotational broadening is less visible. The latter option simulates that the spectrum was taken with a spectrograph with lower resolving power and is therefore the preferred approach from a physical point of view. However, both approaches were carried out and produce similar results. Therefore, only the lower resolution approach is presented in the following in detail.

Even though the available spectrum covers the wavelength range between 3800 and 8000 Å, the parts between 5500 and 8000 Å were ignored during the fit. This part of the spectrum is significantly contaminated by telluric absorption lines ($> 6800 \text{ Å}$) which are originating in Earth's atmosphere. A reliable correction for this effect is difficult but possible (see for instance Moehler et al. (2014)). However, difficulties are introduced because the spectrum is composed out of 82 single exposures which lead to a complex behaviour of the telluric lines. Therefore, the region in which the telluric lines are strong is excluded from the fit. In addition, between 5500 and 6800 Å problems regarding the flux calibration became clearly visible and therefore the corresponding region was also excluded from the fit. The S/N is expected to be 50.

Unfortunately, the flux units are not known. This means, that the parameter θ has no physical meaning for this fit but is rather a scale factor to compensate for the flux units.

Fig. 4.1 shows the best fit for PG1104. Not each parameter of the spectral fit is in agreement with the results published by Vos et al. (2012) obtained by SED fitting (see Tab. 4.2. The temperature of the cool companion and its surface gravity are overestimated. However, if one part of the spectrum suffers a reliable flux calibration, other parts may also be affected, but the effect may not be as obvious. Furthermore, the helium content of the subdwarf is overestimated compared to the analysis of Vos et al. (2012). Vos et al. (2012) fixed this value for their SED fit. Even in the spectral fit, the number should be taken with care because the helium fraction has influence on very few lines only and is therefore often highly degenerate. The metallicity of the cool companion is much lower in the spectral analysis.

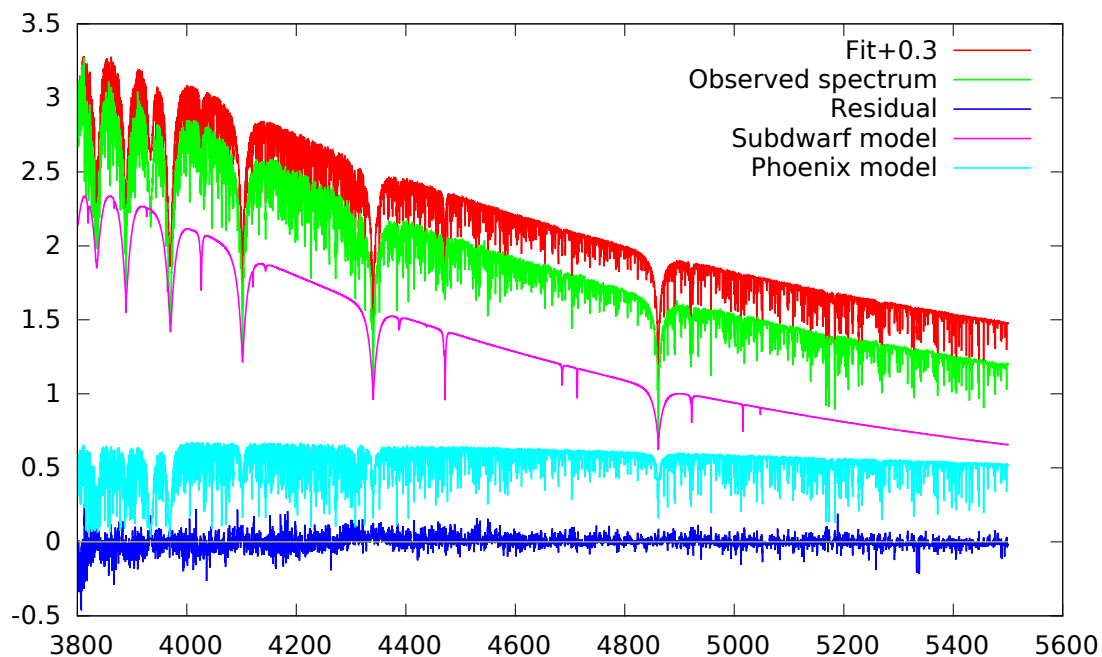


Figure 4.1: Spectral fit for candidate PG1104+243. The spectrum was convolved to $\Delta\lambda = 0.2 \text{ \AA}$ resolution. Problems regarding the flux calibration and contamination with telluric lines restricted the fit to the depicted region.

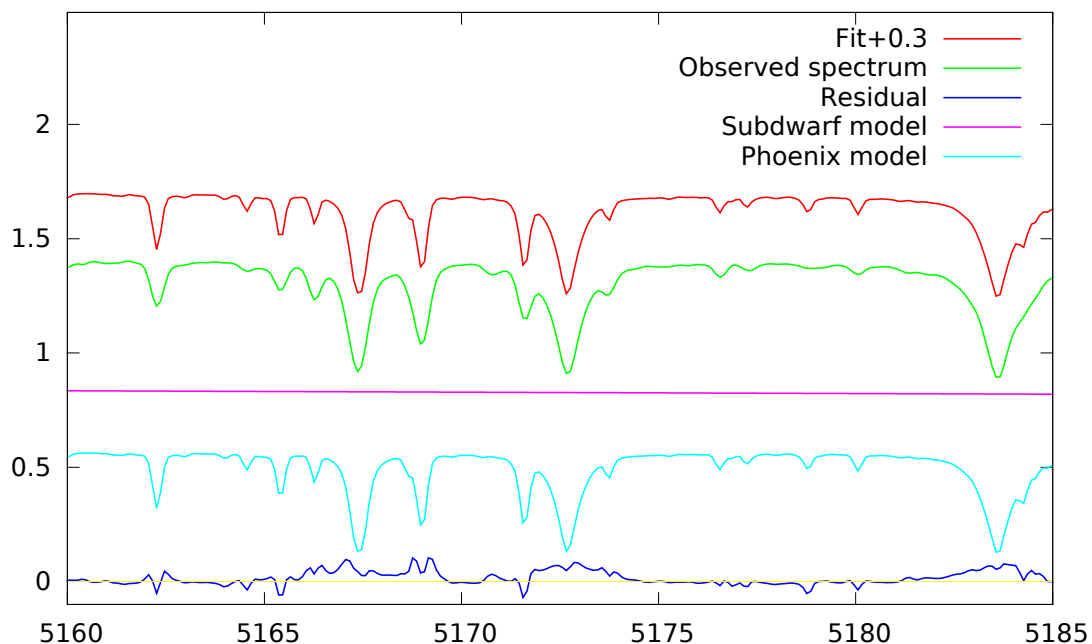


Figure 4.2: Spectral fit for candidate PG1104+243. The spectrum was convolved to $\Delta\lambda = 0.2 \text{ \AA}$ resolution. The region around the Mg triplet is shown in detail. There is good agreement between the fit and the observed spectrum.

Cool companion				Hot subdwarf			
T_{eff} [K]	$\log g$ [dex]	Fe/H [dex]	m [M_{\odot}]	T_{eff} [K]	$\log g$ [dex]	He/H [dex]	θ [$1 \cdot 10^{-5}$]
6269^{16}_{-17}	$5.08^{+0.03}_{-0.04}$	$-0.14^{+0.04}_{-0.03}$	$0.871646^{+0.08}_{-0.06}$	33968^{72}_{-67}	$5.84^{+0.02}_{-0.02}$	$-1.78^{+0.03}_{-0.04}$	$40.19^{+0.25}_{-0.25}$

Table 4.2: Fit results for PG1104+243. $\chi^2_{red} = 0.991256$ for S/N= 50. The surface ratio is 10.74. Note, that θ has no physical meaning here but is rather a scale factor. The temperature of the companion as well as surface gravities are higher if they are determined by spectral fitting compared to the SED fit procedure. However, due to the different data and analysis methods, the results can not be directly compared to the values from Vos et al. (2012).

However, it is much more difficult to determine the metallicity from the SED since single lines do not participate in the χ^2 . It is instructive to have a closer look at a part of the fit in order to see how single lines behave and how the code can treat high resolution data. Fig. 4.2 shows the region around the Mg triplet at 5170 \AA in detail. This example demonstrates that the code is able to reproduce quite small features and therefore the metallicity should be nicely constrained. It suggests that the deviations from the values from Vos et al. (2012) are most probable due to the data itself and not due to numerical artefacts. All in all, the spectral class of the cool companion is of type F, according to the spectral analysis and not G, as published by Vos et al. (2012). However, the high surface gravity is suspicious and may be a hint on an incorrect flux calibration. It should be emphasized again, that the spectrum is different from the observation Vos et al. (2012) used for their analysis and they also used other techniques to determine their parameters. Therefore, direct comparison is difficult.

This testcase shows that the routine is able to also reproduce high resolution spectra. The calculation time for the fit was below 4 days. However, it also emphasizes that reliable flux calibration is an important issue for the decomposition method to work. In addition, more effort needs to be put into solving the problem of degeneracies (See also Sec. 3.4). A possible solution for this is presented in Sec. 5.1.1). Furthermore, effects only visible in high resolutions spectra, stellar rotation for instance, need to be implemented in the code.

4.2 Stars from the HVS sample

As mentioned in Sec. 2.1, the main driver of this project was the occurrence of reddened stars in a color-color plot. These objects became suspicious to be binary systems already throughout the work on my Bachelor's thesis (Kreuzer, 2013). In the following, their properties are briefly revisited.

4.2.1 The Objects

The aim of my Bachelor's thesis (Kreuzer, 2013), was to find new candidates for hypervelocity stars (HVS), which are stars travelling with a velocity exceeding the Galactic escape velocity.

They are perfect probes to constrain the shape and mass of the Galactic dark matter halo. Blue stars in the halo are good candidates, because they have only short lifetimes. Therefore, they might have to travel fast in order to reach their present day position in the halo, because star formation is only possible in the Galactic disk. In order to predict their true space velocity, it is necessary to estimate their distance. This was done using photometric measurements from the SDSS survey and dividing the sample into different temperature regimes. This is shown in a color-color plot in Fig. 4.3.

Some of the stars do not fit the models for constant surface gravity and temperature depicted. They are red shifted, which means they have an excess in the IR. This might be due to interstellar extinction. However, the complete sample consists of halo stars which are not expected to be significantly affected by interstellar extinction. Probably, a cool component might add some flux in the IR. Visual inspection of their spectra revealed indeed the presence of a cool companion for most of them. Because cool stars are typically much fainter than hot stars, they should not be visible in the spectrum if the primary is a massive O/B-type star. This is different if the hot component is a subdwarf star, which is much fainter and therefore closer. In this case, they might have almost equal fluxes in the optical and both components become visible in the spectrum. This sample of reddened stars was the main driver for initiating this work on disentangling subdwarf binaries as a Master's project.

4.2.2 Spectral Fitting

The spectra for the candidates presented in the following are taken from SDSS DR10. SDSS provides spectra in which wavelengths are given as vacuum values, not corrected for any radial velocity value but the barycentric correction. In order to prepare the spectra for the fitting procedure, first the spectrum will be shifted by the radial velocity value determined by the automated analysis of SDSS and subsequently the vacuum wavelengths will be converted to air wavelengths. Even though the result of changing the order of the two wavelength conversions is negligible, this chronological order is adapted from nature. First, the spectrum gets shifted by the relative movement of the star. Then, the light travels through vacuum and hits Earth's atmosphere before the detector measures the spectrum. In order to shift the wavelength scale from vacuum to air wavelengths, the formula from Ciddor (1996) was used, which was already used to convert the *PHOENIX* grid to air wavelength. Wavelength shifts due to radial velocity are implemented by applying the well known relation

$$\frac{\delta\lambda}{\lambda} = \frac{v_{rad}}{c} \quad (4.1)$$

Due to the design of the SDSS and BOSS spectrographs as multi-fibre instruments (see Sec. 1.4) the resolution may be a rather complex function of the wavelength. In addition, this function is different for every fibre and also depends on the observing conditions. SDSS provides spectra in FITS¹ format which contain in addition to the wavelength and flux

¹FITS = Flexible Image Transport System, a file format developed by NASA to contain multidimensional

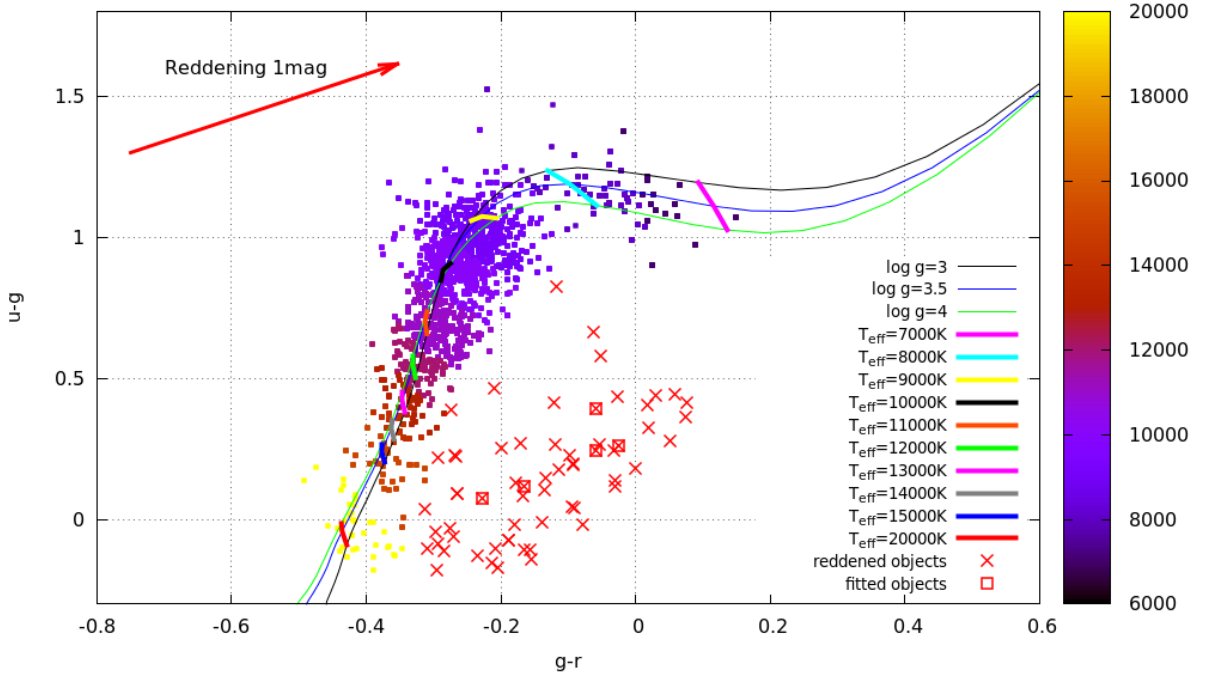


Figure 4.3: Color-color-diagram of a hot star sample, over-plotted with lines of constant $\log g$, and $\log g$ for constant temperature, according to Castelli & Kurucz (2004). The sample is divided 'by eye' into temperature intervals of 1000 K. The reddening vector corresponds to a reddening of 1 mag due to interstellar extinction, according to Kim & Lee (2007). Objects marked as red asterisks seemingly show strong reddening, but interstellar extinction is unlikely to be the cause of the IR excess. Visual inspection of their spectra revealed that most of them have a cool companion. Plot taken from Kreuzer (2013), with additional marking (squares) for the objects which were fitted in the course of this project (red boxes).

information also the wavelength dispersion at each pixel σ_{disp} . This is given in terms of the pixel size and must therefore be converted to units of wavelength. Following the principle discussed in Lee et al. (2015), the resolution R at each pixel can be calculated using the following equation.

$$R = \sqrt{8 \cdot \ln \cdot \ln 10} \cdot 1 \times 10^{-4} \cdot \sigma_{disp} \quad (4.2)$$

Now, the FWHM $\Delta\lambda$ can be calculated.

$$\Delta\lambda = \frac{\lambda}{R} \quad (4.3)$$

This needs to be done for each pixel separately. Fig. 4.4 shows the wavelength dependence of $\Delta\lambda$ for all SDSS spectra of which the result of the fit is presented in this thesis. It shows, that the resolution is strongly depending on the fibre. The steep rise at 6000 Å occurs due to the overlapping of the blue and the red arm of the spectrograph. Since these curves

arrays.

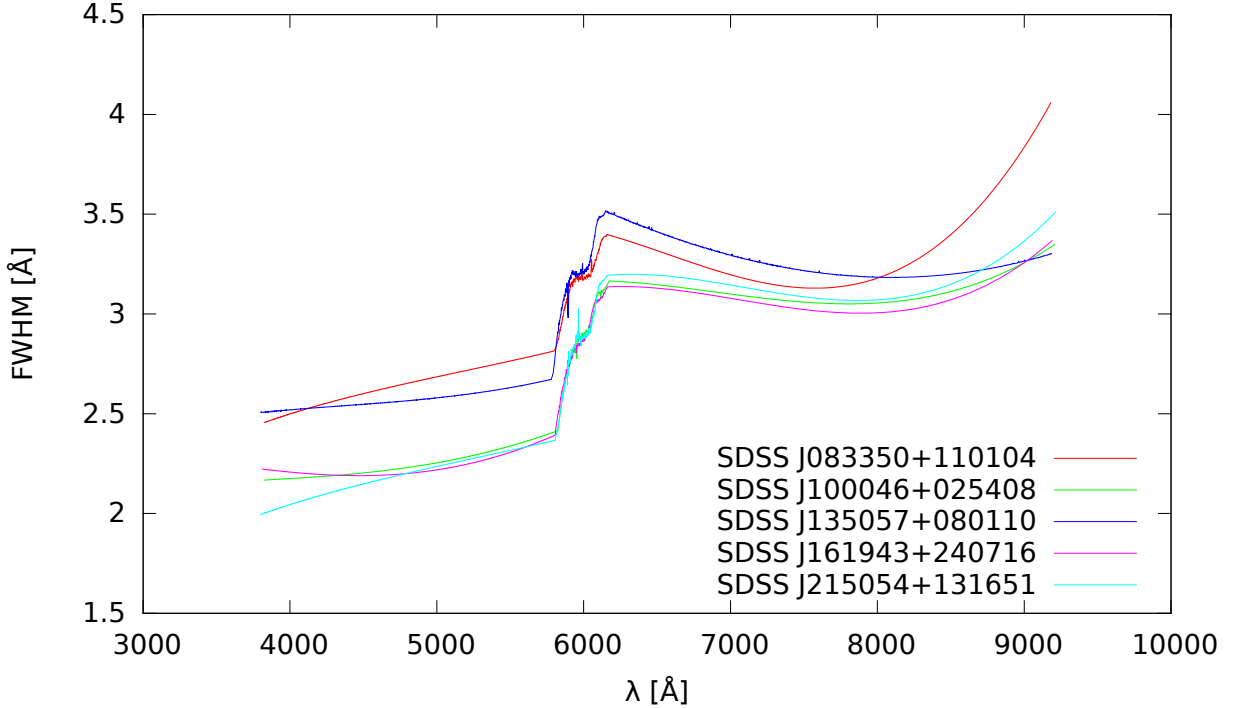


Figure 4.4: Wavelength dependence of the resolution of the SDSS spectra which were fitted. The steep rise at 6000 Å is the overlap region of the red and the blue arm. All spectra are taken by the SDSS spectrograph. The resolution also depends on the fibre.

cannot be modelled easily, the convolution code was modified slightly in order to use a different broadening profile for each pixel (See App. A.2).

Five candidates were fitted with the code. Fig. 4.3 shows that these candidates are evenly dispersed throughout the region of reddened stars (red boxes). The fit routine was running in complete automatic mode, meaning that the input consists only of the following quantities and the start values were chosen automatically close to the middle of the parameter ranges of the corresponding grids. Towards the IR, the wavelength range is constrained by the subdwarf grid.

- Observation (from SDSS DR 10)
- Wavelength range (3820-7500 Å)
- Radial velocity (from SDSS DR 10)
- S/N (from SDSS DR 10)
- Resolution (from SDSS DR 10)
- Reddening (from (Schlegel et al., 1998), (Schlafly & Finkbeiner, 2011))

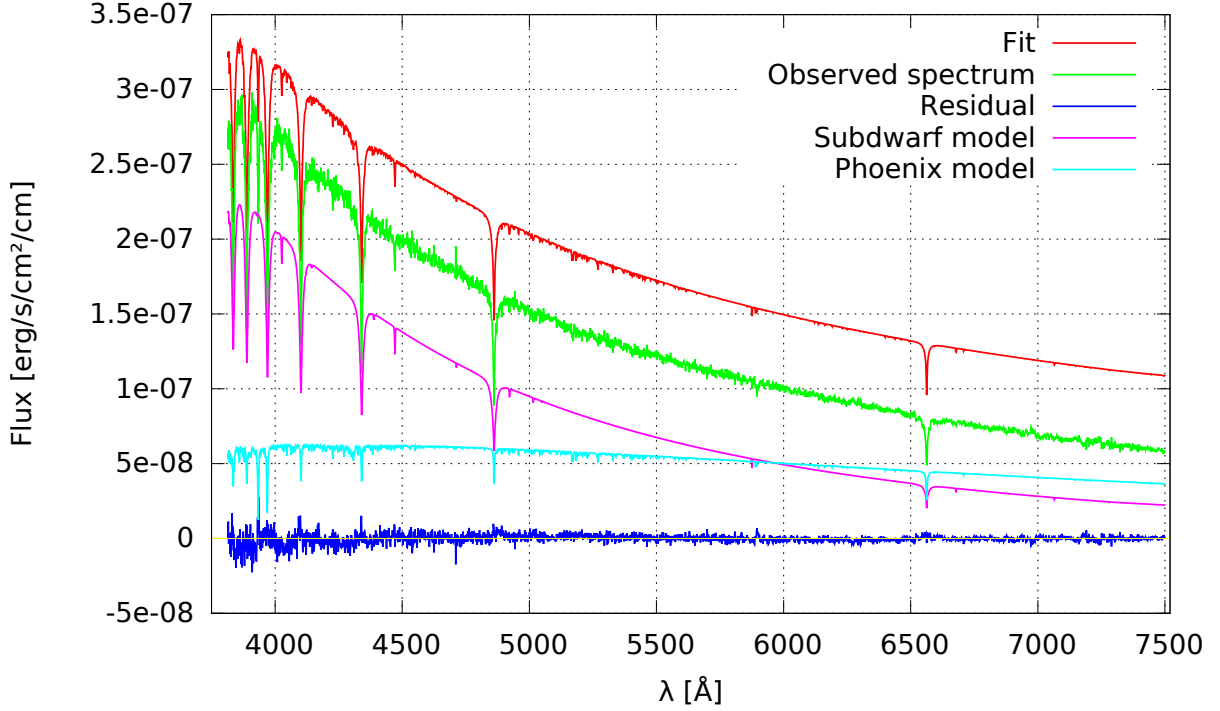


Figure 4.5: Fully automatized spectral fit for candidate SDSS J161943+240716.

- Maximum number of iterations allowed (2000)
- Subdwarf grid (see Sec. 2.2.1)
- Phoenix library (see Sec. 2.2.2)

The input data of the five candidates are summarized in Tab. 4.3. Uncertainties on radial velocity as well as on the reddening parameter $E(B - V)$ and the S/N are not considered here. They are on the order of ± 0.001 for $E(B - V)$ and $\pm 5 \text{ km s}^{-1}$ for v_{rad} and therefore negligible.

The summary of the fit results for all five stars is given in Tab. 4.4, the corresponding spectral fits can be found in Fig. 4.5 for candidate SDSS J161943+240716 and in App. B.4 for all other candidates. All cool companions show temperatures consistent with those of the expected variety of F/G/K stars (3500-7300 K). Except of one star, the metallicities are subsolar in each case. For two candidates, SDSS J100046+0254408 and SDSS J135057+080110, the surface gravities of the cool companion are unexpectedly large (> 5.4), which is physically unrealistic as we will see in the following section where they are compared with stellar evolution tracks. The hot subdwarf stars reside all in the regime of sdB stars ($< 35000 \text{ K}$). Their gravities and helium content is plausible.

	$E(B - V)$	v_{rad} [km s ⁻¹]	S/N
SDSS J083350+110104	0.0271	+247.42	37.64
SDSS J100046+025408	0.0163	+121.11	39.57
SDSS J135057+080110	0.0208	+112.28	48.86
SDSS J161943+240716	0.0580	-222.22	46.57
SDSS J215054+131651	0.1209	-95.28	35.49

Table 4.3: Input values for the fit routine for five SDSS candidates. $E(B - V)$ values are taken from Schlegel et al. (1998) and Schlafly & Finkbeiner (2011), v_{rad} and S/N values are determined by the automated data analysis of SDSS.

4.2.3 Comparison with stellar evolution predictions

The fitted data is now confronted with theoretical predictions on the evolution of hot subdwarfs. Three different evolutionary model predictions are available up to now and frequently used in literature. The tracks were calculated by Dorman et al. (1993), Han et al. (2002) and Bloemen et al. (2014). The latter one is the most sophisticated approach where atomic diffusion due to radiative levitation, gravitational settling, concentration diffusion as well as thermal diffusion is taken into account.

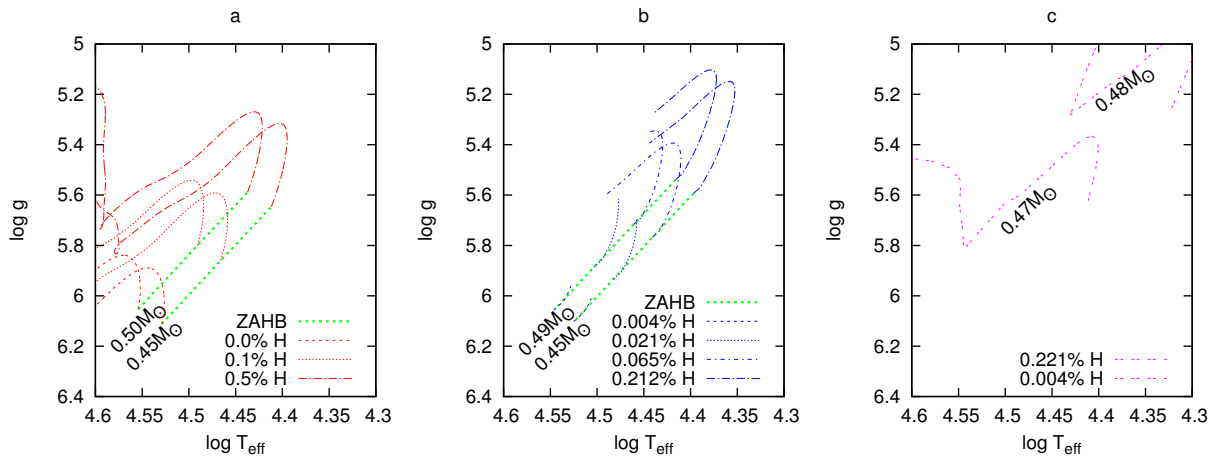


Figure 4.6: Comparison of different evolution tracks for hot sdB stars. a: Tracks from Han et al. (2002), plotted for different H mass fractions, for 0.45 (bottom) and 0.49 M_{\odot} (top). All models shown have solar metallicity. b: Tracks from Bloemen et al. (2014), plotted for different H mass fractions, for 0.45 (bottom) and 0.50 M_{\odot} (top). Solar metallicity. There is agreement between these tracks and the Han et al. (2002) tracks. c: Tracks from Dorman et al. (1993) for 0.47 (bottom) and 0.48 M_{\odot} (top). These models differ from both, the Bloemen et al. (2014) and the Han et al. (2002) predictions. See text for discussion.

First, the models should be compared against each other in order to find systematic

cool companion				
	T_{eff} [K]	$\log g$ [dex]	Fe/H [dex]	M [M_{\odot}]
SDSS J083350+110104	5810^{+164}_{-122}	$4.35^{+0.13}_{-0.08}$	$-2.01^{+0.44}_{-0.17}$	$0.70^{+0.29}_{-\infty}$
SDSS J100046+025408	7169^{+33}_{-43}	$5.42^{+0.03}_{-0.14}$	$0.50^{+0.04}_{-0.08}$	$1.57^{+\infty}_{-0.08}$
SDSS J135057+080110	6565^{+43}_{-27}	$5.50^{+0.03}_{-0.03}$	$-0.49^{+0.12}_{-0.03}$	$1.17^{+0.05}_{-0.06}$
SDSS J161943+240716	5930^{+58}_{-39}	$4.47^{+0.05}_{-0.05}$	$-1.43^{+0.11}_{-0.09}$	$0.74^{+0.07}_{-0.02}$
SDSS J215054+131651	4375^{+77}_{-67}	$4.77^{+0.09}_{-0.06}$	$-1.50^{+0.30}_{-0.23}$	$1.31^{+0.21}_{-0.24}$

hot subdwarf				
	T_{eff} [K]	$\log g$ [dex]	He/H [dex]	θ [$1 \times 10^{-17.5}$]
SDSS J083350+110104	24753^{+542}_{-477}	$5.22^{+0.08}_{-0.10}$	$-3.81^{+0.86}_{-0.99}$	$59.09^{+0.96}_{-0.24}$
SDSS J100046+025408	34516^{+201}_{-612}	$6.05^{+0.07}_{-0.03}$	$-1.77^{+0.08}_{-0.23}$	$27.80^{+0.11}_{-0.08}$
SDSS J135057+080110	29636^{+330}_{-119}	$6.18^{+0.02}_{-0.04}$	$-2.13^{+0.02}_{-0.04}$	$49.99^{+0.12}_{-0.14}$
SDSS J161943+240716	23802^{+278}_{-198}	$5.15^{+0.04}_{-0.05}$	$-2.59^{+0.16}_{-0.20}$	$57.80^{+0.12}_{-0.22}$
SDSS J215054+131651	29415^{+351}_{-400}	$5.42^{+0.08}_{-0.08}$	$-2.33^{+0.13}_{-0.14}$	$47.31^{+0.98}_{-0.67}$

	Surface Ratio	χ^2_{red}	calculation time [hr:min]	memory [MB]
SDSS J083350+110104	4.005	0.83105	01:56	140
SDSS J100046+025408	14.00	1.10953	05:36	235
SDSS J135057+080110	11.84	1.22222	09:07	162
SDSS J161943+240716	7.746	0.95060	08:23	235
SDSS J215054+131651	12.51	1.02882	03:08	165

Table 4.4: Fit results for five SDSS-candidates. Memory gives the peak of the amount of virtual memory used during the fit. For uncertainties denoted by " ∞ " the uncertainty calculation was not possible because the parameter value was too close to the grid edge / the allowed parameter space.

differences. A direct comparison of the part of the grids which is of interest is shown in Fig. 4.6, where evolutionary tracks are plotted into a Kiel diagram. It shows, that there are some minor differences between the Han et al. (2002) and the Bloemen et al. (2014) models. They differ especially for small hydrogen envelopes where the rise in the Han et al. (2002) evolutionary tracks is much steeper. However, the tracks from Dorman et al. (1993) show a strong dependence on the stellar mass. Their tracks are not explicitly stepped in envelope mass, but this quantity can be derived from their published tracks roughly. The given envelope mass for their track corresponds to the envelope mass at the zero age horizontal branch (ZAHB) but, of course, decreases over time due to the hydrogen shell burning. For all other tracks, the envelope mass is explicitly given and does not decrease throughout evolution. Therefore, they cannot be compared directly.

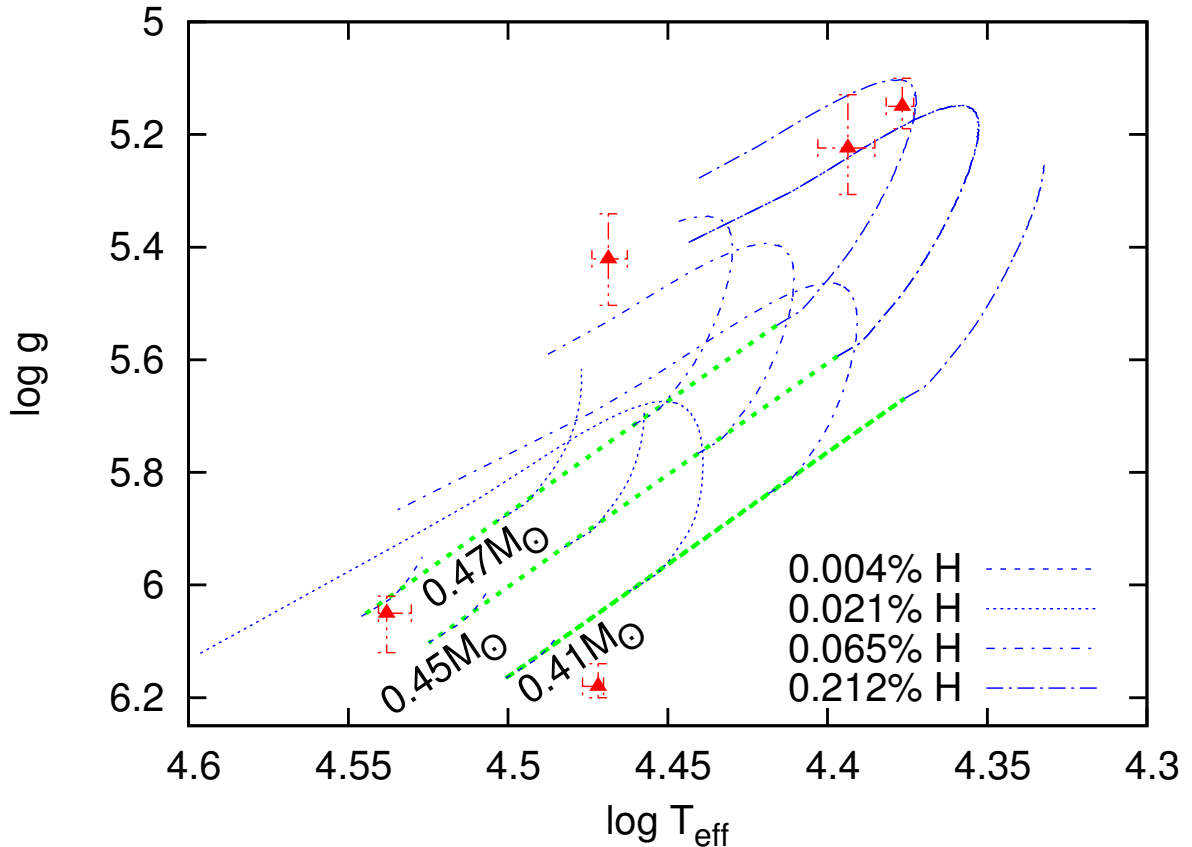


Figure 4.7: Fitted parameter of the hot subdwarf of five candidates from the SDSS sample, overplotted with the evolutionary tracks from Bloemen et al. (2014). All stars are within the theoretically predicted parameter ranges.

The Bloemen et al. (2014) models are consistent with all hot subdwarf observations and their calculation follows the most complex and modern approach. Therefore, they are taken into account for comparison with the fitted values. Fig. 4.7 shows the evolutionary tracks

overplotted with the fitted parameters of the five SDSS candidates. All data points are located within the region covered by the models and are therefore consistent with theory. However, two of the objects show relatively high surface gravity and are located at the top end of the possible parameter range. The cool companions of the two outliers also show high surface gravity (see below) which might be an indicator for either a strong degeneracy in the fit or a physical problem. Furthermore, the fits of the most extreme candidates also show the highest χ^2_{red} and the worst residuals in the fits (see App. B.4).

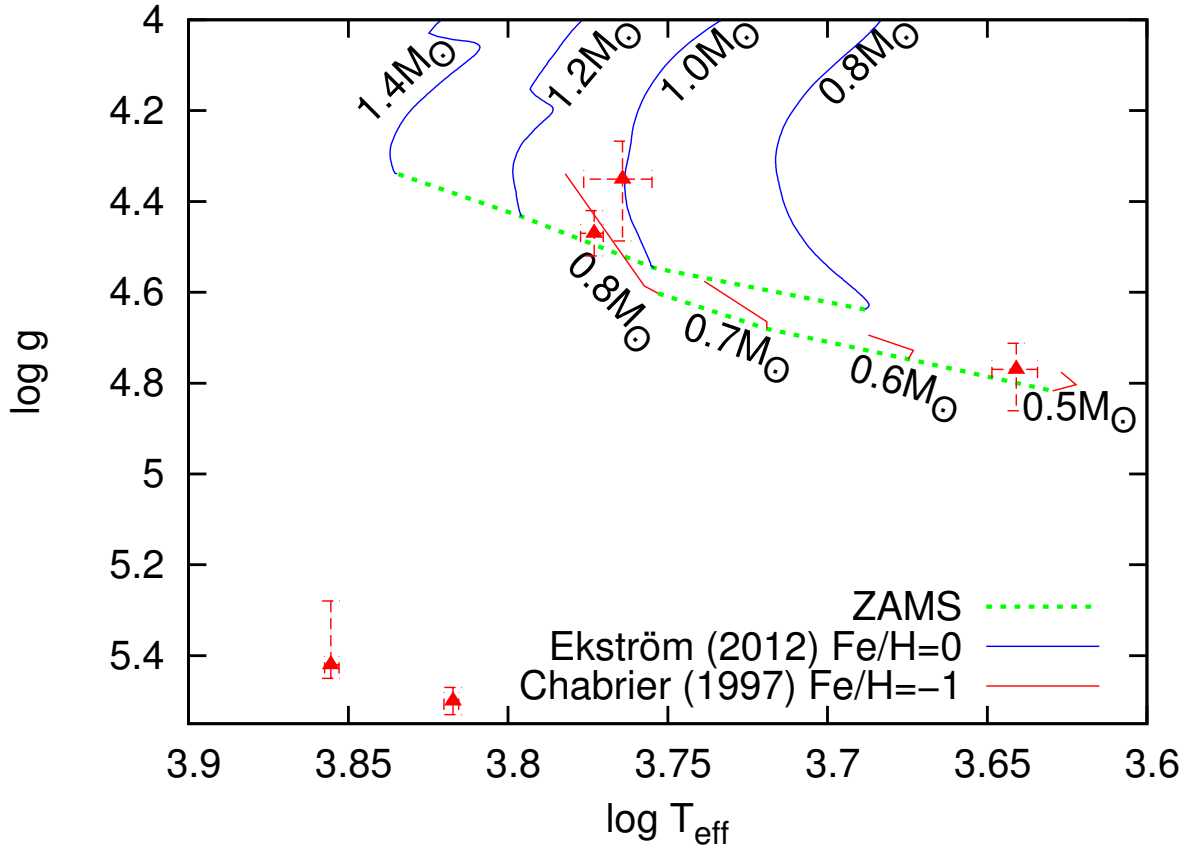


Figure 4.8: Fitted parameters of the cool companion of five candidates from the SDSS sample, overplotted with the evolutionary tracks from Chabrier & Baraffe (1997) (sub-solar metallicity) and Ekström et al. (2012) (solar metallicity). Even though the ZAMS shifts towards higher gravities and temperatures for lower metallicity, two of the candidates show too high gravity and reside outside of the allowed region.

Also, the values for the cool companions can be compared with evolutionary tracks. Fig 4.8 shows the data points overplotted with evolution tracks derived by Chabrier & Baraffe (1997) ($\leq 0.8M_{\odot}$) and Ekström et al. (2012) ($\geq 0.8M_{\odot}$). Again, the gravity for at least two of them turns out to be overestimated by the fit. Note, that the two stars with the highest surface gravities correspond to the outliers in the Fig. 4.7. They also show high surface gravities for the subdwarf companion. If these systems are not binary but triple

systems, the third component might be almost invisible in the spectrum. Assuming this third component to be a compact object, like for instance a white dwarf, which would be too faint to contribute significantly to the spectrum, yields additional pressure broadening in the spectral lines and therefore higher $\log g$ in the binary fit. This effect may not only affect the hot subdwarf model but also the fit of its companion. The different slope of the spectrum can in special cases be corrected via an appropriate combination of temperatures and distance - and therefore θ . Another explanation for this effect might be the presence of the artefacts in the χ^2 landscape of the surface gravities already observed in Sec. 3.3. App. B.3 shows the χ^2 lines around the minimum for candidate SDSS J135057+080110. Two Minima are clearly visible, but there is no secondary local minimum for values of $\log g < 5$. Even though higher metallicity might shift the zero age main sequence for cool stars to higher T_{eff} and $\log g$, as seen in Fig 4.8 when comparing both $0.8M_{\odot}$ tracks, three of the stars reside clearly out of the theoretically allowed region. As discussed above, this might be due to the presence of a third companion not clearly visible in the spectrum or degeneracies in the fit. As shown in Sec. 3.4 there is a strong correlation between the surface gravities of both star. If a numerical problem is the reason for the shape of the χ^2 line around the best fit in $\log g$, this problem might be solved by applying another method in order to find the best fit. An alternative is discussed in Sec. 5.1.2.

Summary

- The fit routine is able to fit the high resolution ($\Delta\lambda = 0.2 \text{ \AA}$) data of candidate PG1104+243. Comparing it with the results from previous publications yields similar results. However, the observation is different from the one used in the publication and probably the spectrum suffers reliable flux calibration.
- SDSS provides spectra with variable resolution and a strong wavelength dependence. It also depends on the observing conditions, and especially the fibre. The code fully accounts for this.
- The fit of five SDSS candidates from a samples of blue stars showing excess in the IR was executed. The computation times were just a few hours.
- Comparing the results with evolutionary tracks reveals consistency but a shift towards higher gravities for both companions of two objects. This can either be explained by a strong correlation between the surface gravities or the presence of a third component.
- Again, two minima are observed for the surface gravities. In order to exclude this to be a numerical artefact one could introduce different fit algorithms and switch in between them.

5 Outlook and Conclusion

5.1 Outlook and possible improvements

This section gives an overview of ideas which might yield further improvements for the code developed in the course of this project. In particular, degeneracies amongst surface gravities and a more advanced subdwarf grid which may replace the standard grid already in use are discussed. In the end, general short ideas for more accurate fit results are given.

5.1.1 Solving the $\log g$ degeneracy problem

As seen in Sec. 3.4, the degeneracy between the surface gravities is a severe problem. Sec. 4.2.2 revealed, that this can also be the reason for the fit drifting to higher values for both parameters in SDSS spectra. One approach in order to be able to achieve a better fit is to reduce the number of degrees of freedom, meaning that other parameters should be kept fixed and iterated later on.

This could for instance be implemented by first fitting the parameters of the star which contributes most of the flux, afterwards iterating the parameters of its component. The efficiency of this procedure can be increased by specifying wavelength regions, in which only one component contributes significantly to the lines while the other component is only visible in the continuum. The list of important spectral lines in Sec. 1.1.2 may serve as a proxy for the splitting of the spectrum in parts. After alternating between the two stars, a global fit of all parameters simultaneously may help to find the global minimum.

Another approach would be to put constraints on other parameters using SED fits like carried out in Németh et al. (2016). θ and T_{eff} are well constrained by photometry. Especially constraints on T_{eff} are expected to improve the results for the surface gravity. As θ is the angular diameter of the star and therefore also encodes the distance, additional constraints can be put on θ if the distance is known. The Gaia mission¹ (Perryman et al., 2001) will provide accurate parallax measurements which will be released within the next years. The first data release covers already 2 million distances out of 1 billion stars observed by Gaia. Their results are eagerly awaited.

Furthermore, the list of important spectral lines in Sec. 1.1.2 hosts a number of lines which are crucial for the problem. Therefore, tiny regions in the spectrum may be able to constrain single parameters better than using the whole continuum. A solution to be more sensitive to the deviation in important spectral lines rather than to the whole continuum could be the introduction of different weights of specific spectral regimes in the determination of the

¹<http://www.esa.int/Gaia>

χ^2 . Giving for instance the Balmer series, the Mg I triplet and some He lines more weight would yield a faster increase in χ^2 when stepping away from the best fit. Therefore, the degeneracy may be reduced.

5.1.2 Genetic algorithm

In order to deal with the complex χ^2 landscape in this particular fit problem one may use the combination of different fit algorithms, alternating between them in order to find the best fit. Another idea for future implementation would be to follow a completely different approach by not doing a fit but rather following the principles of nature. So called *genetic algorithms* tend to find the global best fit also in complex χ^2 landscapes. The idea behind these algorithms is that the first generation of spectra is randomly distributed over the whole parameter range. As only the best adapted individuals of a species survive in nature, also only the spectra which reproduce the observation best survive. This set of spectra is used to breed the next generation. Important in this step is, that the breeding takes place with a random number involved. These steps are executed several times and therefore the overall ability of the spectra to reproduce the observation improves over time. Additionally, with some probability mutations should occur during the breeding process. This is the equivalent of ensuring that the iteration does not get stuck in a local minimum while scanning the χ^2 landscape during a fit routine.

Using a genetic algorithm is promising to find the best fit faster. Remember, that the error determination in the current implementation is restarted every time a better fit was found. The computation time therefore decreases in the case of the genetic code because the routine does not require that many restarts as working with a downhill simplex algorithm. The drawback, however, is, that the genetic code itself does not provide simple termination criteria or uncertainty calculation techniques, but since the χ^2 landscape is scanned extensively during the breeding of new individuals, it might be possible to use this knowledge to calculate the uncertainties.

5.1.3 Extended LTE grid for the hot subdwarfs

A grid calculated by Ulrich Heber provides a more extended parameter range as well as a larger wavelength coverage and better resolution, compared to the non-LTE *TLUSTY/SYNSPEC* grid used in this work. The parameters and their covered ranges are summarized in Table 5.1. This grid also considers line blanketing and includes metal lines. Unfortunately, this grid is not as regular as the non-LTE *TLUSTY/SYNSPEC* grid and, therefore, challenges the interpolation routine. Filling the holes in the grid for instance by interpolation between surrounding spectra would allow to also use this grid for spectral fitting.

One big advantage of the LTE grid is the wavelength coverage from 2700 Å - 12000 Å in constant 0.05 Å steps. This allows the use of all important lines mentioned in Tab. 1.2 in the fit - especially the CaII IR triplet which originates from the cool companion only and therefore provides much information. Furthermore, a large fraction of the hydrogen Paschen series is included, which originates from both stars. The helium abundance values are only

parameter	lower limit	stepsize	upper limit
λ [\AA]	2700	0.05	12000
T_{eff} [K]	9000	1000	50000
$\log g$ [cgs]	4	0.2-0.25	6.40
He/H	0.909	0.970, 0.990	0.999

Table 5.1: Parameters and the corresponding ranges covered by the grid calculated by Ulrich Heber. The helium abundance is given as overall percentage for four different abundances.

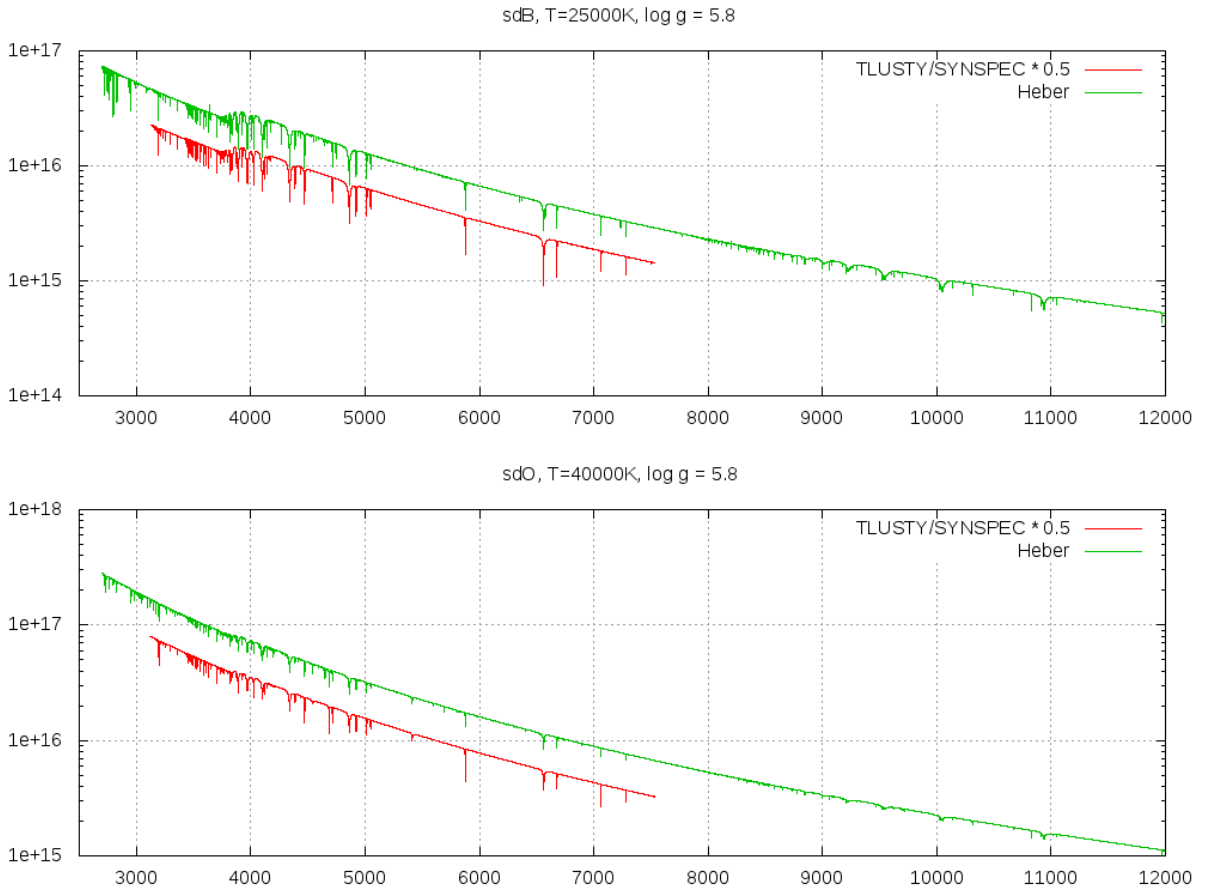


Figure 5.1: Comparison of sdB and sdO synthetic spectra from both available model grids. Note, that direct comparison is difficult, because of the different conventions for the helium abundance value. Furthermore, the LTE grid (green) includes metals in contrast to the *TLUSTY/SYNSPEC* grid.

sampled in 4 steps, which allows the grid to be small and handy. The overall size of the grid is only 5.6 GB, covering only solar metallicity up to now.

Fig. 5.1 shows the typical sdB and sdO spectra from both libraries. Of course, the spectra from the LTE grid provide much more features due to the metals being present in the synthetic atmosphere. Note, that a direct comparison of both grids is difficult due to the different conventions for the helium abundance value.

Comparing sdB to sdO spectra shows an interesting behaviour. sdB spectra typically show more intense lines, which makes fitting much easier. This is a general trend: the higher the temperature, the more difficult the fit. Therefore, the uncertainties for all inferred parameters of hotter stars ($T_{eff} \gtrsim 35000$ K) are expected to be larger than the ones of cooler ($T_{eff} \lesssim 35000$ K) stars. This was, in fact, already observed in Sec. 3.3.

5.1.4 Other possible improvements

In order to further increase precision a more sophisticated grid-interpolation may be used. Newton- or spline interpolation allows a smoother interpolation, but with the cost of a longer computing time.

In high-resolution spectra, other line broadening effects become important. One of the most prominent ones is the rotational broadening, which may easily be implemented. Applying another convolution with a rotational broadening profile in addition to the Gaussian profile for instrumental broadening may help to reproduce high-resolution data. Again, more computation time would be needed and another free parameter ($v \sin i$) would be introduced. An iterative way of fixing some of the parameters while fitting the others and alternating between them (as discussed in Sec. 5.1.1) would then probably be required.

A way to minimize the impact of the quality of the flux calibration may be the use of "spectral windows". Dividing the spectrum into smaller parts and allow the angular diameter θ to be fitted separately for each part may allow to correct for flux calibration flaws on-the-fly during the fit.

5.2 Conclusion

The aim of this project was the analysis of hot subdwarf composite spectra. Previous attempts met with limited success mainly constrained by limited models or long computation times. This thesis describes the development of a fast method for the decomposition of their spectra. Chapter 2 discusses the basic ideas and algorithms which were used to address this problem.

An observation is reproduced by fitting a linear combination of spectra from two different libraries to the observation. Spectra from both libraries have to be adapted to the observation by accounting for the instrumental broadening by convolving them with a Gaussian of the corresponding width. In order to find the best fitting combinations of the 8 free parameters a standard downhill simplex routine is used and implemented in the code. The free parameters are the temperatures and surface gravities for both, the subdwarf and the cool companion, as well as metallicity and mass for the cool companion and helium abundance for the subdwarf. An additional scaling parameter, corresponding to the angular diameter of a

star, allows the flux intensity to be fitted. The code avoids the use of external packages. Due to the specific aim of the project, optimizations can more easily be implemented in self-written code rather than in pre-written packages which consist in most cases of rather general code.

Test cases for the convolution and the fit routine itself were discussed. The convolution has to be as less time consuming as possible but should produce highly accurate results which means that a trade-off between calculation time and accuracy has to be found. The test of the fit routine with a mock binary spectrum and the examination of the determination of the uncertainties of the final parameters according to standard χ^2 statistics shows overall consistency. However, the surface gravities of both stars suffer a huge degree of degeneracy. All example spectra are corrected for reddening. The code is used to analyze high-resolution spectra of the well studied candidate PG1104+243 as well as low-resolution spectra of 5 sdB binaries. The parameters of PG1104+243 have been estimated by Vos et al. (2012) using SED fitting. Comparing the results achieved with this code to the values from literature shows general agreement but shifts towards higher gravities and temperatures for the cool companion. However, issues regarding the flux calibration are clearly visible in the spectrum and huge parts could not be used due to contamination with telluric lines. Low-resolution (~ 2.5 Å) spectra of 5 sdB binaries from the SDSS spectral database were analyzed with the code, which was the aim of the project. The wavelength and fibre dependent resolution of SDSS spectra are discussed and the effect is fully included in the code. Comparing the resulting atmospheric parameters to evolutionary tracks shows good agreement for three of them. Two candidates are shifted towards higher gravities (especially their cool companions). This may be caused by degeneracies and strong correlations between both surface gravities. Ideas to solve this issue and add further improvements to the code are discussed.

All in all, the existing code provides the tool needed to be able to disentangle binary star spectra in a fully automated way. The code accounts for reddening and known radial velocity as well as arbitrary resolution wavelength dependence. The computation times are reasonably fast. Because the implementation follows object oriented principles, it is also a good starting point for further improvements. Even though it has not been tested yet, due to easily exchangeable spectral libraries, the code should be able to disentangle all kinds of binaries in all spectral ranges. At the time being, the code provides all requirements to disentangle hot subdwarf binaries as outlined in Sec. 2.1. A combination with a photometric analysis of SEDs would be rewarding to constrain the parameters more strictly.

A C++ Code

A.1 Downhill Simplex Algorithm - The code

```
1 class simplexFit{
2
3     int _maxRestarts;
4     int _maxIterations;
5     double _ftol;                //typically 1e-4
6     double _chisq;
7     vector<double> _simplexSum;
8     std::vector< std::vector <double> > _simplex;
9     std::vector<double> _chisqVec;
10
11
12
13
14 int simplexFit::doFit() {
15
16
17 // First calculate chisquare at all simplex points
18 for (int k = 0; k < _simplex.size(); k++) {
19     double value = f(_simplex[k]);
20     _chisqVec.push_back(value);
21 }
22
23
24 for (cnt = 0; cnt < _maxIterations; cnt++) {
25
26     // Find highest, second highest and lowest chisquare
27
28     // Recompute Simplexsum
29     _simplexSum.clear();
30     simplexSum();
31
32     int inhi = 0;
33     int ihi = 0;
34     int ilo = 0;
35     float TINY = 1.0e-10;
36     double ndim = _simplex.size() - 1;
37     for (int i = 0; i < _simplex.size(); i++) {
38         if (_chisqVec[i] <= _chisqVec[ilo])
39             ilo = i;
40         if (_chisqVec[i] > _chisqVec[ihi]) {
```

```

41     inhi = ihi;
42     ihi = i;
43 } else if (_chisqVec[i] > _chisqVec[inhi] && i != ihi) {
44     inhi = i;
45 }
46 }
47 _chisq = _chisqVec[ilo];
48
49 //Compute tolerance and check whether limit is achieved
50 //criterion from Nelder & Mead 1965
51 double sum = 0;
52 double average = 0 ;
53 for (int i = 0; i < _simplex.size(); i++)
54     average += _chisqVec[i];
55 average /= _simplex.size();
56
57 for (int i = 0; i < _simplex.size(); i++)
58     sum += (_chisqVec[i] - average)*(_chisqVec[i] - average);
59 double rtol = sqrt(sum / _simplex.size());
60
61 int do_restart = 0;
62 if (rtol < _ftol) {
63     cout << "Fit converged! - rtol:" << rtol << "   ftol:" << _ftol
64         << "   Red.Chisquare:" << _chisqVec[ihi] / (_dof)
65         << "   Iterations:" << cnt << endl;
66         return 1;
67 }
68 }
69
70 //check whether factor is smaller than zero
71 for (int i = 0; i < _simplex.size(); i++) {
72     if (_simplex[i][3] < 0)
73         _simplex[i][3] = -_simplex[i][3];
74     if (_simplex[i][7] < 0)
75         _simplex[i][7] = -_simplex[i][7];
76 }
77
78 //Begin new Iteration. First extrapolate by a factor of -1 through the
79 //face of the simplex across from the high point, i.e. reflect the simplex
80 //from the high point.
81
82 //Gives a result better than the best point, so try an additional
83 //extrapolation by a factor 2.
84 if (chisq_try <= _chisqVec[ilo])
85     chisq_try = amotry(ihi, 2.0);
86
87 //The reflected point is worse than the second-highest, so look for an
88 //intermediate lower point, i.e. do a one dimensional contraction
89 else if (chisq_try >= _chisqVec[inhi]) {

```

```

88     double chisq_save = _chisqVec[ihi];
89     chisq_try = amotry(ihi, 0.5);
90     // Can't seem to get rid of that high point. Better contract around the
91     // lowest (best) point.
92     if (chisq_try >= chisq_save) {
93         for (int i = 0; i < _simplex.size(); i++) {
94             if (i != ilo) {
95                 for (int j = 0; j < ndim; j++)
96                     _simplex[i][j] = _simplexSum[j] = 0.5
97                     * (_simplex[i][j] + _simplex[ilo][j]);
98                 _chisqVec[i] = f(_simplexSum);
99             }
100         }
101     }
102 }
103
104 int cnt_old = cnt;
105 if (do_restart == 1) {
106     cnt = _maxIterations;
107 }
108
109 if (cnt == _maxIterations) {
110     printSimplex();
111     cout << "-----"
112     << endl;
113     f(_simplex[ilo]);
114 }
115 //Iteration End
116 }
117 }
118 printSimplex();
119 return 1;
120 }
121 }
122
123 double simplexFit::amotry(int ihi, float fac) {
124
125     int ndim = _simplex.size() - 1;
126     vector<double> ptry;
127
128     double fac1 = (1.0 - fac) / ndim;
129     double fac2 = fac1 - fac;
130     for (int j = 0; j < ndim; j++) {
131         ptry.push_back(_simplexSum[j] * fac1 - _simplex[ihi][j] * fac2);
132     }
133
134     double chisq_try = f(ptry);
135
136     //If chisquare at test-point lower: Replace everything in chisq_vec und
137     //simplex.

```

```

137  if (chisq_try < _chisqVec[ihi]) {
138      _chisqVec[ihi] = chisq_try;
139      for (int j = 0; j < ndim; j++) {
140          _simplexSum[j] += ptry[j] - _simplex[ihi][j];
141          _simplex[ihi][j] = ptry[j];
142      }
143  }
144
145  return chisq_try;
146 }
147
148 void simplexFit::simplexSum() {
149     //! This funktion updates the _simplexSum member variable of
150     simplex_fit.
151
152     vector<double> ssum;
153     for (int j = 0; j < _simplex[0].size(); j++) {
154         double value = 0;
155         for (int i = 0; i < _simplex.size(); i++)
156             value = value + _simplex[i][j];
157         ssum.push_back(value);
158     }
159     _simplexSum = ssum;
160 }
161
162
163 }

```

Listing A.1: Main part of the code for the simplex algorithm as used in the software, consisting of the three functions `int doFit()`, `double amotry(int, float)` and `void simplexSum()`. For reasons of clarity and comprehensibility, some housekeeping parts are omitted. All functions are member functions of the class `simplexFit`. The function `f(std::vector <double>)` returns the χ^2 for the given combination of parameters in the passed in `std::vector`. Some comments are from Press et al. (2007).

A.2 Numerical convolution

The code for convolving a spectrum to a constant FWHM $\Delta\lambda$ instrument is given below. For instruments with wavelength dependent $\Delta\lambda$, the code is slightly different. In principle, the calculation of the weights and the normalization (lines 27-51) are put inside the for-loop (line 69). This allows the width of the Gaussian for the convolution to be different at each pixel.

```

1  using namespace std;
2
3
4  double interpolate(double pos_to_interpolate ,
5      double position_next_lower_value , double next_lower_value ,
6      double position_next_higher_value , double next_higher_value) {

```

```

7  /// Interpolates between two Values linearly
8  double r = next_lower_value
9      + ((next_higher_value - next_lower_value)
10         / (position_next_higher_value - position_next_lower_value))
11         * (pos_to_interpolate - position_next_lower_value);
12  return r;
13 }
14
15
16
17 int main(){/// Convolve spectrum to wavelength scale
18 /// Only for long-slit! Echelle would require wavelength dependence of
19 sigma
20
21 double sigma_range = fwhm / sqrt(8 * log(2));
22
23 /// sampling rate around each pixel of the final convolution, the more, the
24 better, the slower. distributed in 3sigma range
25 int gnum = 81;
26
27 /// calculate weights depending on sigma
28 double weights[gnum], x_pos[gnum];
29 double incr = (double) 2 * 3 * (double) sigma_range / (double) (gnum - 1);
30 for (int i = 0; i < gnum; i++) {
31     weights[i] = exp(
32         -pow((i - (gnum / 2)) * incr, 2)
33         / (sqrt((2.0) * pow(sigma_range, 2) * 3.14159265359)));
34     x_pos[i] = (i - (gnum / 2)) * incr;
35 }
36
37     for (int i = 0; i < gnum; i++) {
38         weights[i] = exp(
39             -pow((i - (gnum / 2)) * incr, 2)
40             / ((2.0) * pow(sigma_range,
41 2)));
42         x_pos[i] = (i - (gnum / 2)) * incr;
43     }
44 /// Normalization
45 double sum = 0;
46 for (int i = 0; i < gnum; i++) {
47     sum += weights[i];
48 }
49 for (int i = 0; i < gnum; i++) {
50     weights[i] /= sum;
51 }
52
53
54 sum = 0;

```

```

55 for (int i = 0; i < _wlscale.size(); i++) {
56     sum += _flux[i];
57 }
58 for (int i = 0; i < _wlscale.size(); i++) {
59     _flux[i] /= sum;
60 }
61
62 // principal strategy: loop over output x-grid -> create auxiliary mini-
    // grid around each point and loop over it to numerically perform
    // integration
63 // numerical integration requires interpolation of _wlscale on x_pos
64
65 vector<double> final_spec;
66
67 int k_old = 0;
68
69 for (int i = 0; i < newWlscale.size(); i++) // loop over output x-grid
70     {
71
72     int k = k_old;
73     sum = 0; // initializes sum to zero
74     for (int j = gnum; j > 0; j--) // loop over auxiliary mini-grid
75     {
76
77         while (_wlscale[k] < newWlscale[i] + x_pos[j]
78             && k + 1 < _wlscale.size())
79             k++;
80
81         while (_wlscale[k-1] > newWlscale[i] + x_pos[j] && k > 0)
82             k--;
83
84
85         if (j == 0)
86             k_old = k;
87
88         if (k == 0)
89
90             sum += weights[j] * _flux[k]; // linearly interpolate between points
    // to the left (index k-1) and right (index k)
91         else
92             sum += interpolate(newWlscale[i] + x_pos[j], _wlscale[k - 1],
93                 _flux[k - 1], _wlscale[k], _flux[k]) * weights[j]; // linearly
    // interpolate between points to the left (index k) and right (index k+1)
94     }
95
96     final_spec.push_back(sum);
97 }
98
99 // Save convolved spectrum and replace wavelenghtscale
100 _flux.swap(final_spec);
101 _wlscale = newWlscale;

```

102 }

Listing A.2: Numerical convolution code for constant resolution used in this project. The method is adapted from an ISIS code written by Andreas Irrgang and slightly modified.

A.3 Golden section search

This method is capable to find the minimum in one dimensional minimization problems. It is very easy to implement, but less time efficient than more sophisticated algorithms. The function to minimize has to be monotonic and continuously defined. The description here is based on the illustration in Press et al. (2007).

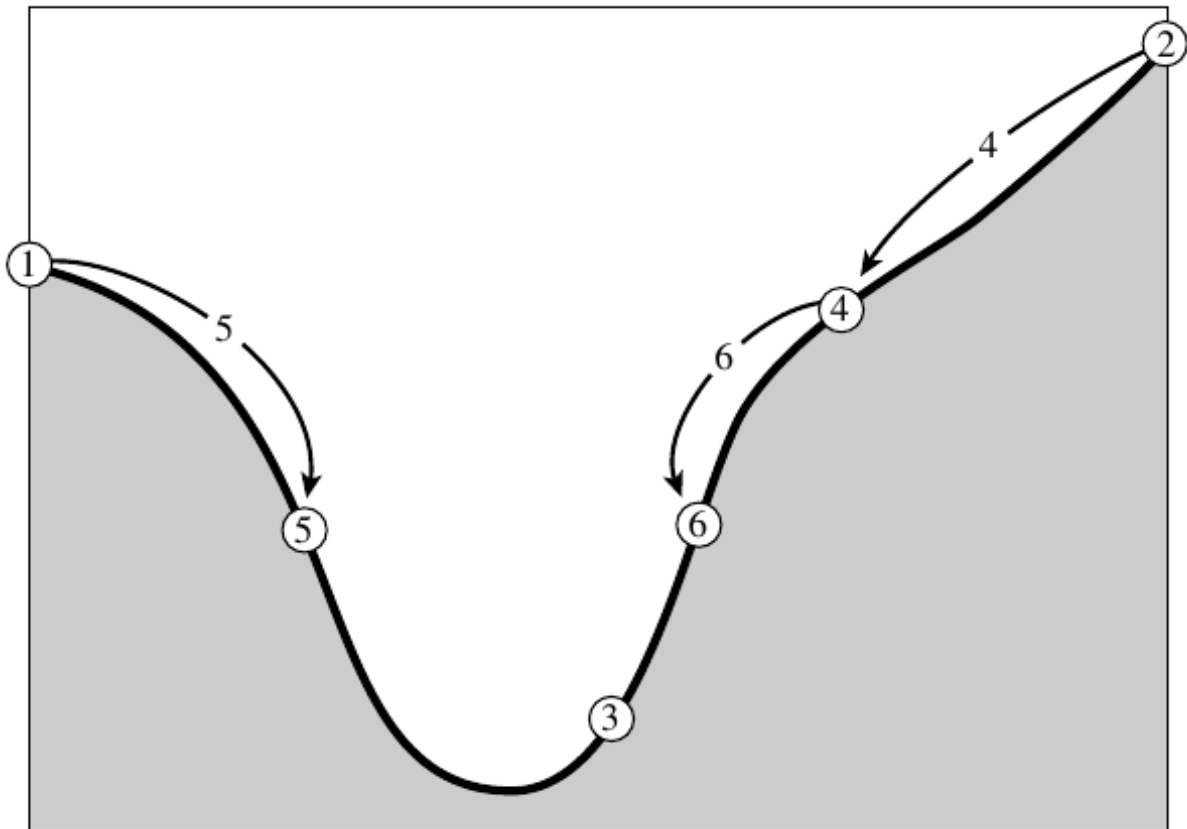


Figure A.1: Graphical illustration of the golden section search. From Press et al. (2007). See text for details.

The procedure is illustrated in Fig. A.1. The idea is, to provide 3 points which bracket the minimum at initialisation (1,3,2). Subsequently, the function is evaluated at a point in between the point with the highest function value and the mid-point in order to get rid of the highest point. In Fig. A.1 (1,3,4) are the bracketing points in this step. The next iterations result in a bracketing of the minimum by the points (5,3,4) and then (5,3,6). This

simple approach is repeated until the termination condition (given as a maximum distance between the points) is met.

One can show, that the optimal value for convergence is achieved if the point where the function is evaluated is given by the *Golden Section*¹ between the two neighbouring points. The convergence is linear: the bracketing of the minimum increases by a factor of 0.62 per iteration.

The code below illustrates the implementation of the Golden Section search in the code.

```

1 double parabola_fit::fit(std::vector<double> startvalues){
2 // Fitting the parameter a of the parabola, using golden section search,
3 // according to Numerical Recipes 2007
4
5 double tol = 1e-10;
6
7 double ax = startvalues[0];
8 double bx = startvalues[1];
9 double cx = startvalues[2];
10
11 const double R = 0.6180339, C = 1.0 - R;
12
13 double x1, x2;
14 double x0=ax;
15 double x3=cx;
16
17 if (abs(cx-bx) > abs(bx-ax)) {
18     x1=bx;
19     x2=bx+C*(cx-bx);
20 } else {
21     x2=bx;
22     x1=bx-C*(bx-ax);
23 }
24
25 double f1=golden_fit_fun(x1);
26 double f2=golden_fit_fun(x2);
27
28 double cnt = 0;
29 while (fabs(x3-x0) > tol*(fabs(x1)+fabs(x2)) && cnt < 10000){
30     if (f2 < f1) {
31         x0=x1;
32         x1=x2;
33         x2=R*x2+C*x3;
34         f1=f2;
35         f2=golden_fit_fun(x2);
36     } else {
37         x3=x2;
38         x2=x1;
39         x1=R*x1+C*x0;
40         f2=f1;
41         f1=golden_fit_fun(x1);

```

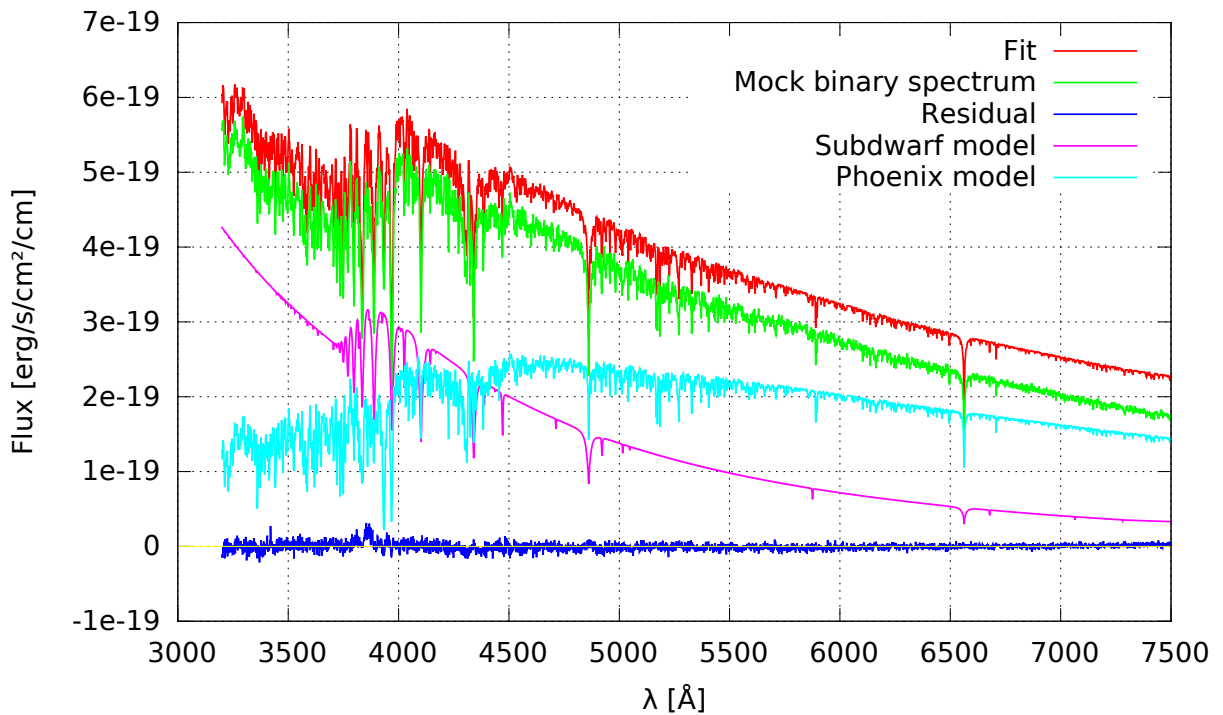
¹The *Golden Section* or *Golden Ratio* is a ratio which is regarded to be aesthetic. The discovery dates back to even before Euklid (300 B.C.). It is defined by $\frac{a}{b} = \frac{a+b}{a}$, corresponding a ratio of 0.618% and 0.382%.

```
39     }
40         cnt++;
41     }
42
43     double xmin, fmin;
44     if (f1 < f2) {
45         xmin=x1;
46         fmin=f1;
47     } else {
48         xmin=x2;
49         fmin=f2;
50     }
51     std::cout << "Best fit =" << xmin << std::endl;
52
53     return xmin;
54 }
```

Listing A.3: Golden Section search C++ code. `golden_fit_fun(x)` calls the function evaluation at point `x`. For reasons of clarity and comprehensibility, some housekeeping parts are omitted.

B Data Analysis

B.1 Fit in χ^2 line for Example 1



Cool companion				Hot subdwarf			
T_{eff} [K]	$\log g$ [dex]	Fe/H [dex]	m [M_{\odot}]	T_{eff} [K]	$\log g$ [dex]	He/H [dex]	Θ [1×10^{-18}]
5863.49	4.46287	-0.000775841	0.955142	23586.7	5.45715	-1.50769	6.99375e

Figure B.1: Fit for the high χ^2 region in the χ^2 lines for the surface gravity in Fig. 3.5. $\log g$ of the companion was fixed to 4.46287. The best fit for the other parameters is given in the table below the plot. The surface ratio is 20.0561, $\chi^2_{red} = 1.86785$. A deviation is clearly seen in the region close to the Balmer jump and also in the balmer lines. The reason for this remains unclear. See text for discussion.

B.2 χ^2 lines of Example 2 for $S/N = 75$

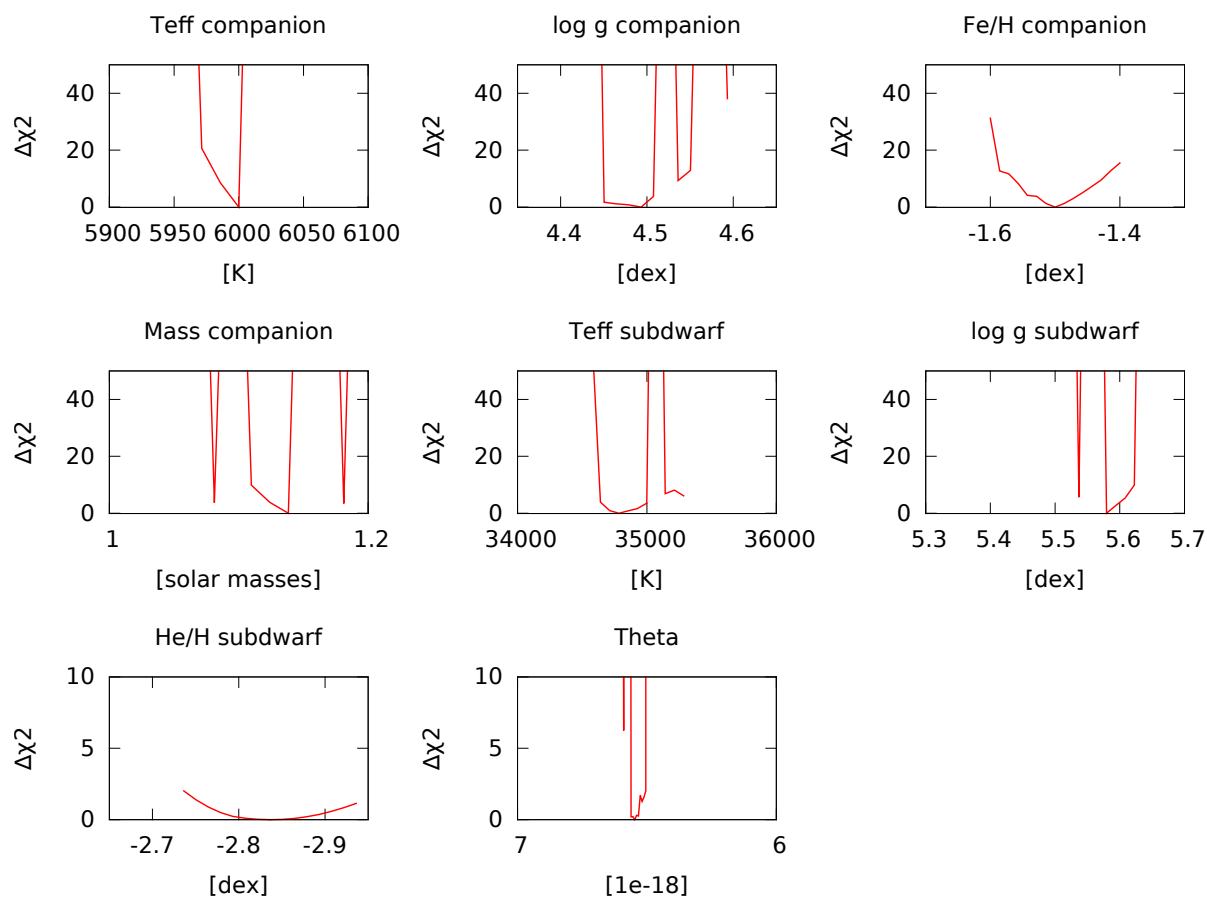


Figure B.2: $\Delta\chi^2$ single parameter lines around the best fit for Example 2. Some of the parameters show a highly complicated pattern in their $\Delta\chi^2$ line with two local minima.

B.3 χ^2 line of candidate SDSS J135057+080110

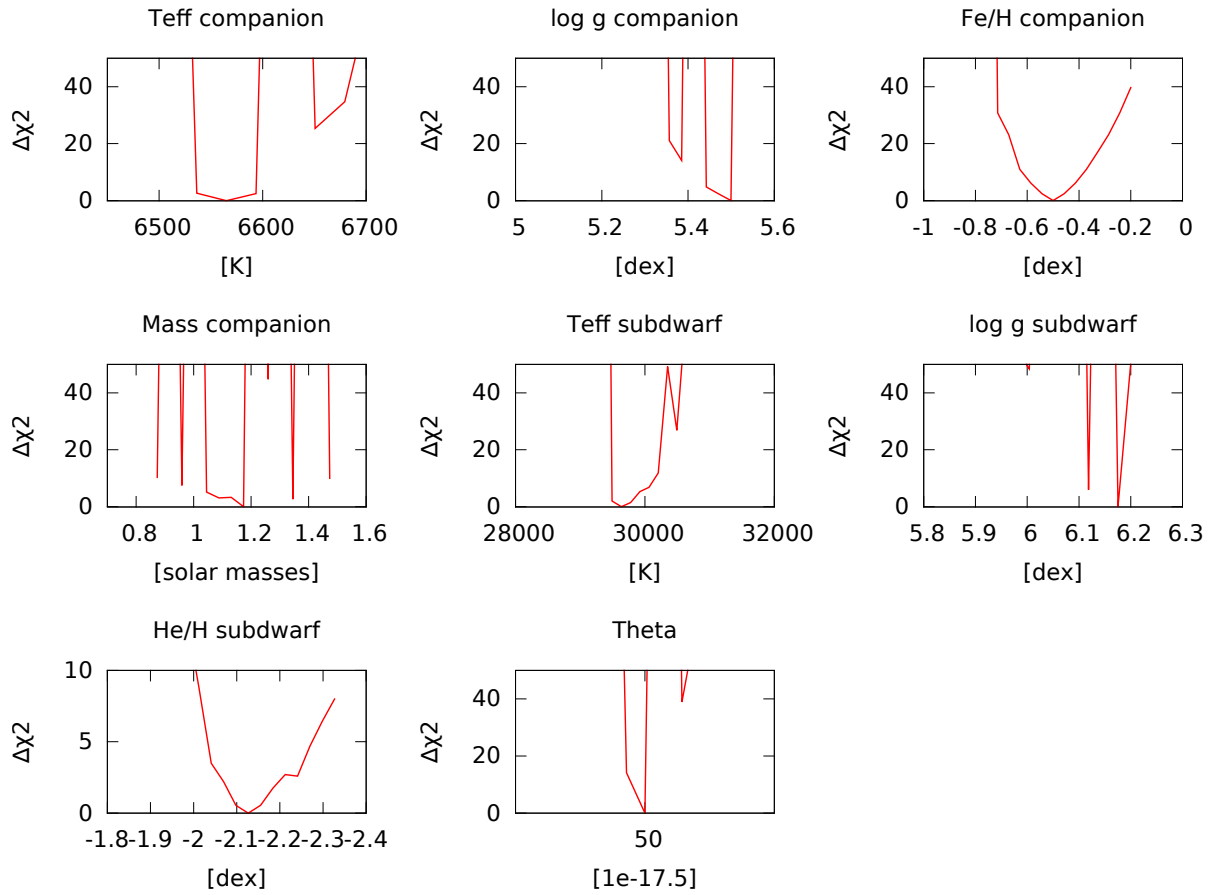


Figure B.3: $\Delta\chi^2$ single parameter lines around the best fit for candidate SDSS J135057+080110. Some of the parameters show a highly complicated pattern in their $\Delta\chi^2$ line with several local minima.

B.4 Spectral Fits

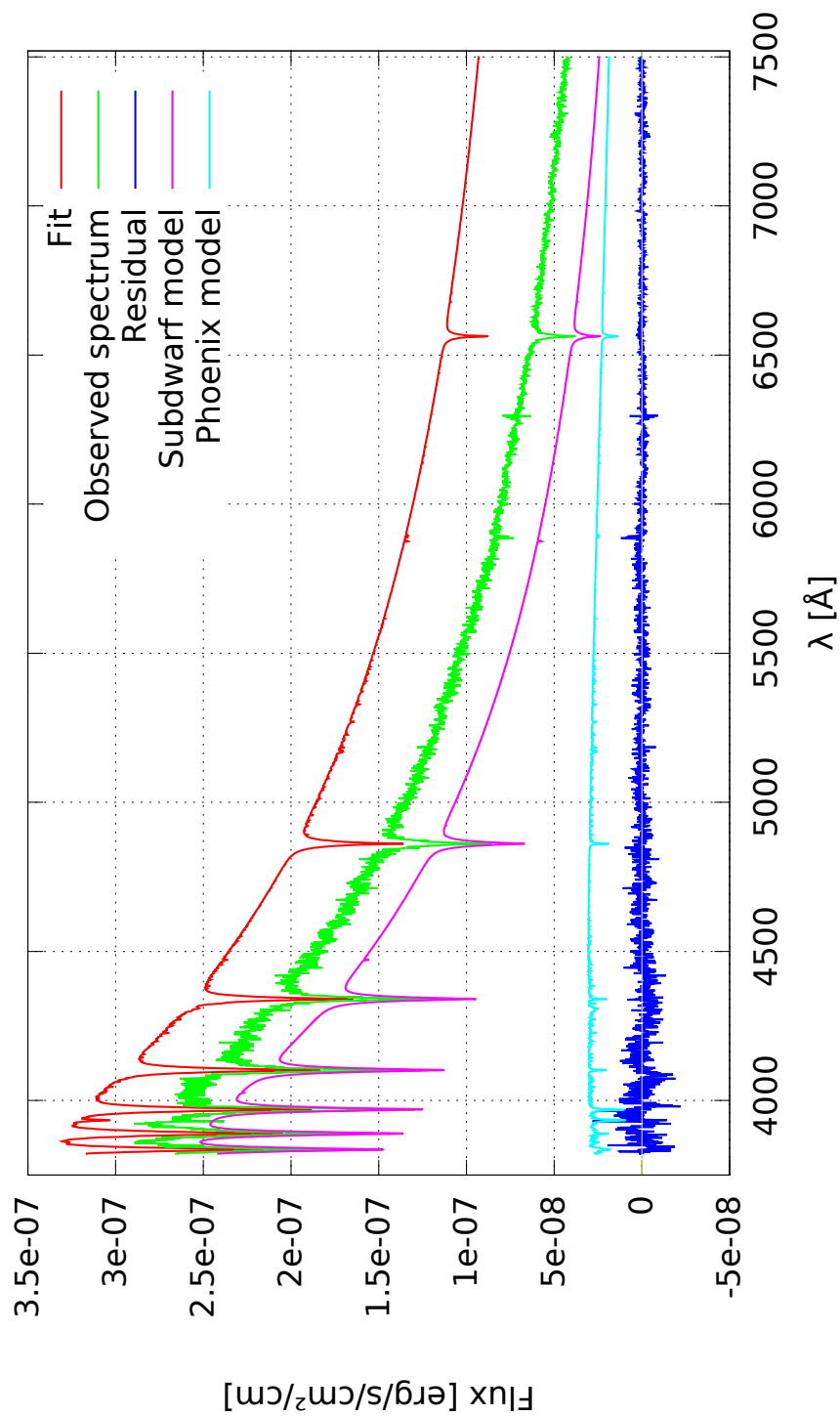


Figure B.4: Fully automatized spectral fit for candidate SDSS J083350+110104.

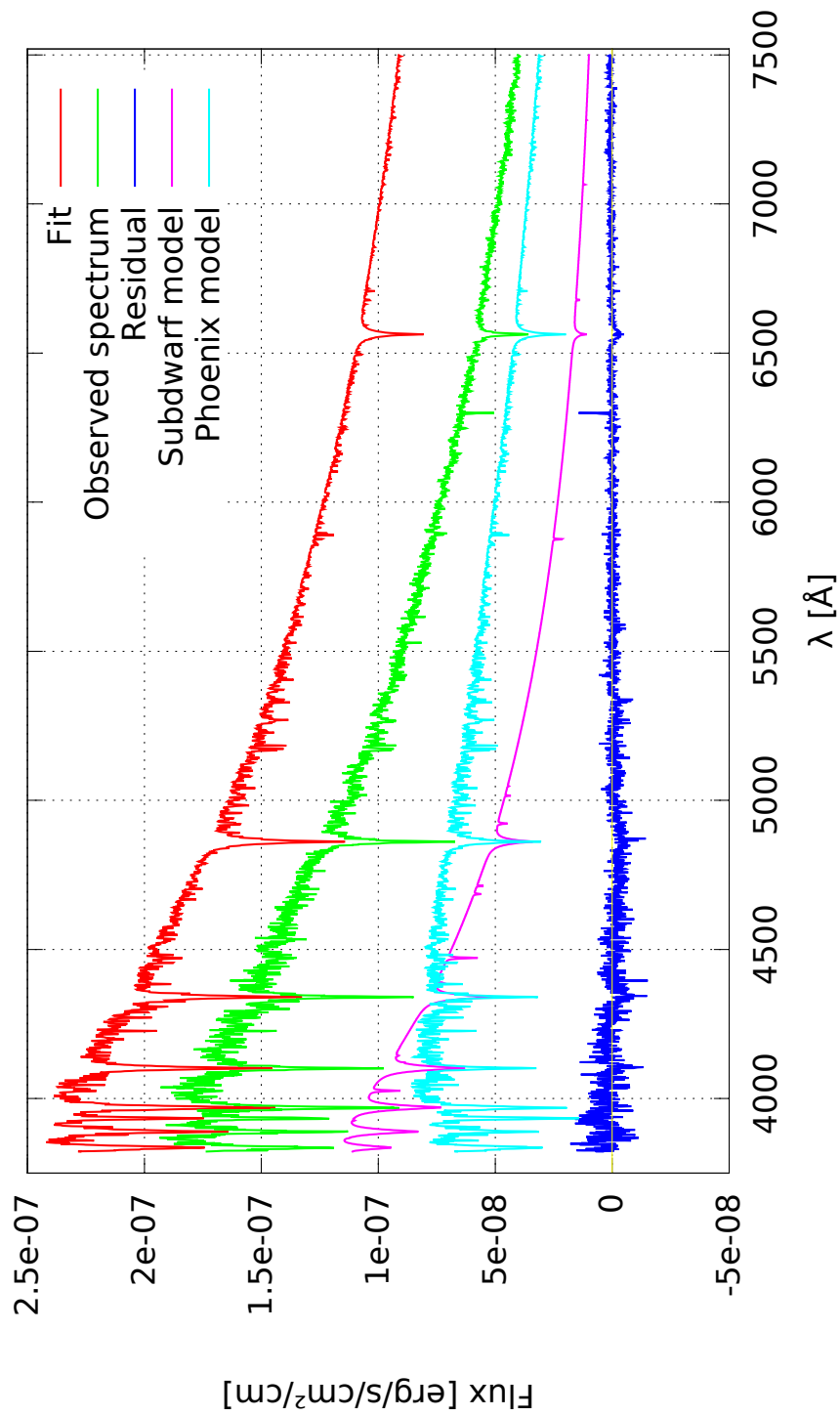


Figure B.5: Fully automatized spectral fit for candidate SDSS J100046+025408.

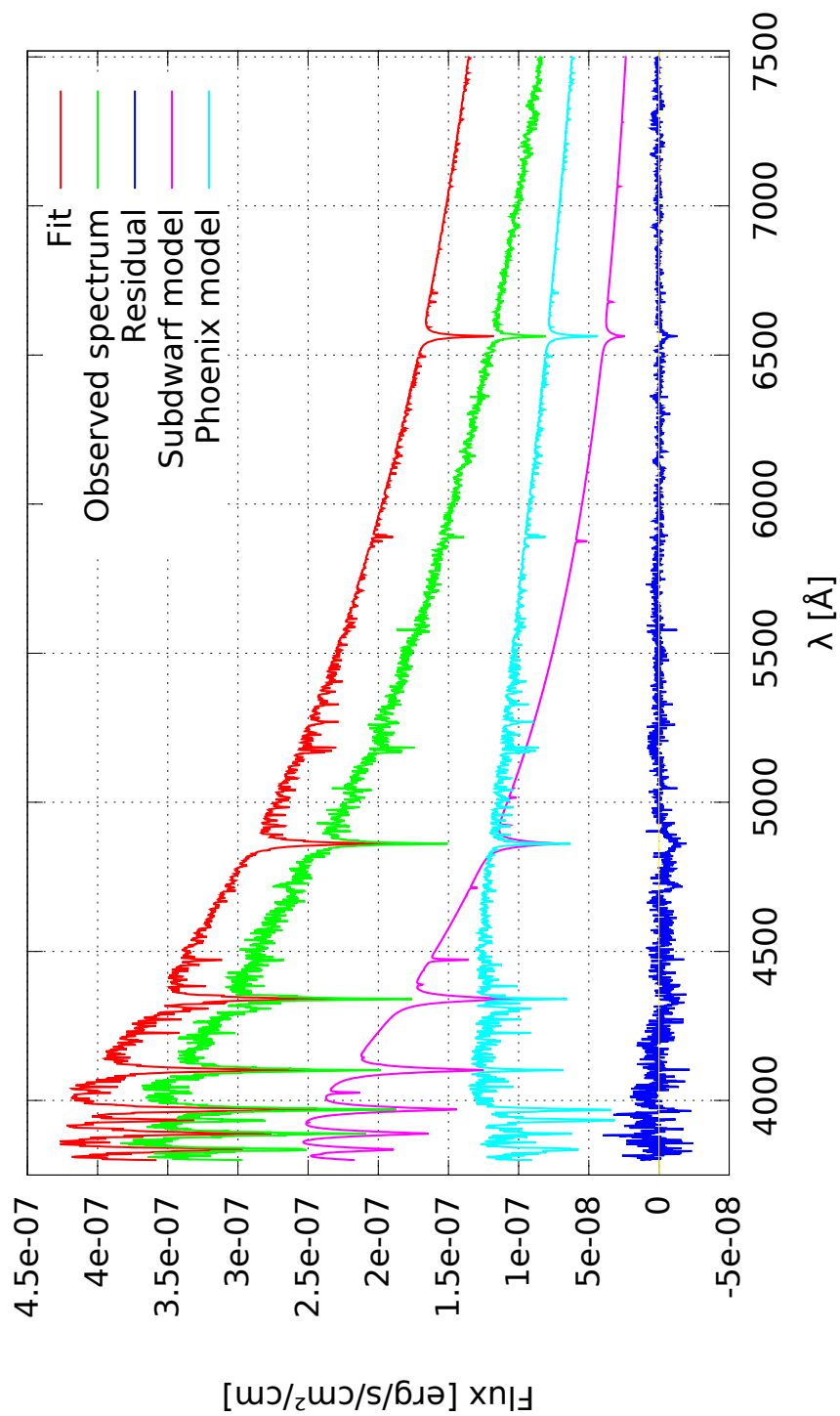


Figure B.6: Fully automatized spectral fit for candidate SDSS J135057+080110.

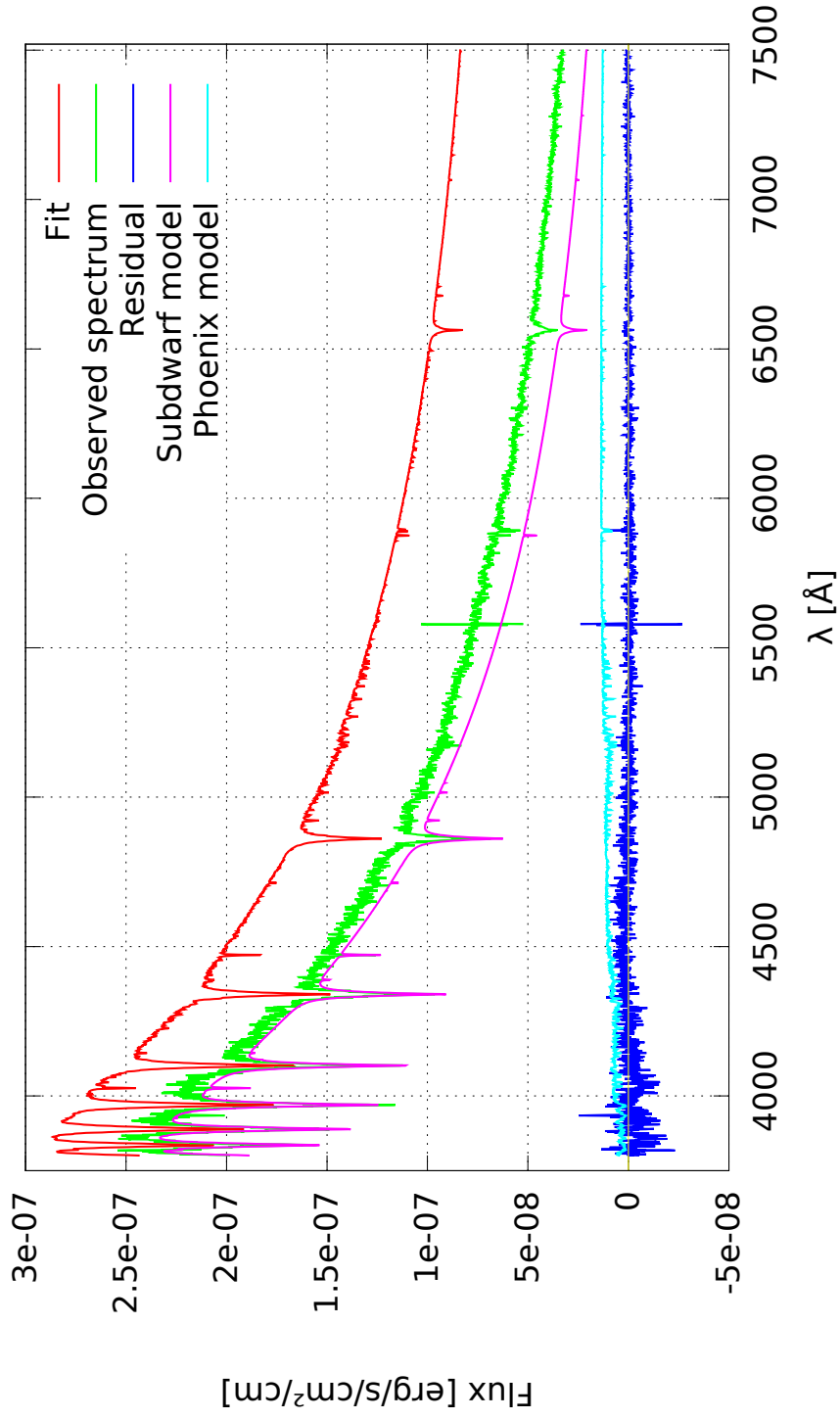


Figure B.7: Fully automatized spectral fit for candidate SDSS J215054+131651.

List of Figures

1.1	Spectral energy distribution for for different black body temperatures . . .	1
1.2	Low resolution spectrum of Vega	2
1.3	HRD	5
1.4	Comparison between HRD and Kiel diagram	6
1.5	Stellar evolution in the HRD	7
1.6	Sample of hot subdwarfs in a Kiel-diagram	8
1.7	Binary evolution channels	10
1.8	Spectral energy distribution of a sdO + G5III star (model spectra)	14
1.9	Sample spectrum from SDSS	16
2.1	Illustration of how the composite spectrum is produced	20
2.2	Interpolation in one dimension	23
2.3	Interpolation in three dimensions	24
2.4	Flowchart of the downhill simplex algorithm	29
2.5	Possible simplex movemenths	31
2.6	Cumulative probability distribution functions of the χ^2 distribution	33
2.7	Interstellar extinction curve	35
2.8	The effect of interstellar extinction on a solar-like spectrum	36
2.9	Flowchart of the binfit-code	38
3.1	Convolution of two Gaussian functions	42
3.2	Phoenix model spectrum convolved to different FWHM.	43
3.3	Spectrum and fit for Example 1	45
3.4	Error estimation based on synthetic spectra with artificial S/N 1	46
3.5	$\Delta\chi^2_{red}$ single parameter lines around the best fit for Example 1	48
3.6	Spectrum and fit for Example 2	49
3.7	Error estimation based on synthetic spectra with artificial S/N 2	51
3.8	$\Delta\chi^2$ single parameter lines around the best fit for Example 2	52
3.9	$\Delta\chi^2_{red}$ maps for Example 1	54
4.1	Spectral fit for candidate PG1104+243	58
4.2	Spectral fit for candidate PG1104+243	58
4.3	Color-color-diagram of the sample	61
4.4	Wavelength dependence of the resolution of SDSS spectra	62
4.5	Spectral fit for candidate SDSS J161943+240716	63
4.6	Comparison of different evolution tracks for hot sdB stars	64

4.7	Kiel diagram with five SDSS candidates and evolutionary tracks	66
4.8	Comparison of different evolution tracks for hot sdB stars	67
5.1	Comparison of sdB and sdO synthetic spectra from different model grids	72
A.1	Graphical illustration of the golden section search	82
B.1	High chi-square fit for Example 1	85
B.2	$\Delta\chi^2$ single parameter lines around the best fit for Example 2	86
B.3	$\Delta\chi^2$ single parameter lines around the best fit for SDSS J135057+080110	87
B.4	Spectral fit for candidate SDSS J083350+110104	88
B.5	Spectral fit for candidate SDSS J100046+025408	89
B.6	Spectral fit for candidate SDSS J135057+080110	90
B.7	Spectral fit for candidate SDSS J215054+131651	91

List of Tables

1.1	Spectral classification of hot subdwarfs	6
1.2	Important spectral lines in sd + G/F binaries	15
1.3	Technical specifications of BOSS and SDSS spectrograph	17
2.1	Parameter ranges of the <i>TLUSTY/SYNSPEC</i> subdwarf grid	21
2.2	Parameter ranges of <i>PHOENIX</i> grid	22
2.3	Free parameters	27
3.1	Parameters for mock binary spectrum, Example 1	44
3.2	χ^2_{red} of all fits for Example 1	45
3.3	Parameters for synthetic binary spectrum, Example 2	49
3.4	χ^2_{red} of all fits for Example 2	50
4.1	Orbital and atmospheric parameters for PG1104+243 from Vos et al. (2012)	56
4.2	Fit results for PG1104+243	59
4.3	Input values for the fit routine for five SDSS candidates	64
4.4	Fit results for five SDSS-candidates	65
5.1	Parameter ranges of the LTE subdwarf grid	72

Bibliography

- Barlow B.N., Wade R.A., Liss S.E., et al., 2012, ApJ758, 58
- Bloemen S., Hu H., Aerts C., et al., 2014, A&A569, A123
- Brown T.M., Sweigart A.V., Lanz T., et al., 2001, ApJ562, 368
- Castellani M., Castellani V., 1993, ApJ407, 649
- Castelli F., Kurucz R.L., 2004, ArXiv Astrophysics e-prints
- Chabrier G., Baraffe I., 1997, A&A327, 1039
- Chen X., Han Z., Deca J., Podsiadlowski P., 2013, MNRAS434, 186
- Ciddor P.E., 1996, Appl. Opt.35, 1566
- Copperwheat C.M., Morales-Rueda L., Marsh T.R., et al., 2011, MNRAS415, 1381
- Dorman B., Rood R.T., O'Connell R.W., 1993, ApJ419, 596
- Drilling J.S., Jeffery C.S., Heber U., et al., 2013, A&A551, A31
- Ekström S., Georgy C., Eggenberger P., et al., 2012, A&A537, A146
- Fitzpatrick E.L., 1999, PASP111, 63
- Fitzpatrick E.L., Massa D., 1990, ApJS72, 163
- Geier S., Hirsch H., Tillich A., et al., 2011, A&A530, A28
- Geier S., Kupfer T., Heber U., et al., 2015, A&A577, A26
- Girven J., Gänsicke B.T., Steeghs D., Koester D., 2011, MNRAS417, 1210
- Green R.F., Schmidt M., Liebert J., 1986, ApJS61, 305
- Greenstein J.L., Sargent A.I., 1974, ApJS28, 157
- Han Z., Podsiadlowski P., Lynas-Gray A.E., 2007, MNRAS380, 1098
- Han Z., Podsiadlowski P., Maxted P.F.L., et al., 2002, MNRAS336, 449

- Heber U., 2009, ARA&A47, 211
- Heber U., 2016, ArXiv e-prints
- Heber U., Hunger K., 1984, The Messenger 35, 29
- Hubeny I., Lanz T., 1995, ApJ439, 875
- Hubeny I., Lanz T., 2011, Synspec: General Spectrum Synthesis Program, Astrophysics Source Code Library
- Humason M.L., Zwicky F., 1947, ApJ105, 85
- Hunger K., Heber U., 1987, Evolution of Hot Subdwarfs - An Empirical Approach. In: Planetary and Proto-Planetary Nebulae: From IRAS to ISO, Vol. 135. Astrophysics and Space Science Library Springer Netherlands, p.137
- Husser T.O., Wende-von Berg S., Dreizler S., et al., 2013, A&A553, A6
- Johnson H.L., Morgan W.W., 1953, ApJ117, 313
- Kim S.S., Lee M.G., 2007, PASP119, 1449
- Kreuzer S., 2013, Bachelorsthesis, A search for HVS candidates via simulation of trajectories
- Lee K.G., Hennawi J.F., Spergel D.N., et al., 2015, ApJ799, 196
- Lisker T., Heber U., Napiwotzki R., et al., 2005, A&A430, 223
- Maxted P.F.L., Heber U., Marsh T.R., North R.C., 2001, MNRAS326, 1391
- Miller Bertolami M.M., Althaus L.G., Unglaub K., Weiss A., 2008, A&A491, 253
- Moehler S., Modigliani A., Freudling W., et al., 2014, A&A568, A9
- Morales-Rueda L., Maxted P.F.L., Marsh T.R., et al., 2003, MNRAS338, 752
- Nelder J.A., Mead R., 1965, Computer Journal 7, 308
- Németh P., Kawka A., Vennes S., 2012, MNRAS427, 2180
- Nemeth P., Östensen R., Tremblay P., Hubeny I., 2014, In: van Grootel V., Green E., Fontaine G., Charpinet S. (eds.) 6th Meeting on Hot Subdwarf Stars and Related Objects, Vol. 481. Astronomical Society of the Pacific Conference Series, p. 95
- Németh P., Ziegerer E., Irrgang A., et al., 2016, ApJ821, L13
- Perryman M.A.C., de Boer K.S., Gilmore G., et al., 2001, A&A369, 339

- Podsiadlowski P., Han Z., Lynas-Gray A.E., Brown D., 2008, In: Heber U., Jeffery C.S., Napiwotzki R. (eds.) Hot Subdwarf Stars and Related Objects, Vol. 392. Astronomical Society of the Pacific Conference Series, p. 15
- Press W.H., Teukolsky S.A., Vetterling W.T., Flannery B.P., 2007, Numerical Recipes 3rd Edition: The Art of Scientific Computing, Cambridge University Press, New York, NY, USA, 3 edition
- Raskin G., van Winckel H., Hensberge H., et al., 2011, A&A526, A69
- Schlafly E.F., Finkbeiner D.P., 2011, ApJ737, 103
- Schlegel D.J., Finkbeiner D.P., Davis M., 1998, ApJ500, 525
- Serenelli A., Weiss A., 2005, A&A442, 1041
- Stroeer A., Heber U., Lisker T., et al., 2007, A&A462, 269
- Tailo M., D'Antona F., Vesperini E., et al., 2015, Nature523, 318
- Vos J., Østensen R.H., Degroote P., et al., 2012, A&A548, A6
- Vos J., Østensen R.H., Marchant P., Van Winckel H., 2015, A&A579, A49
- Vos J., Østensen R.H., Németh P., et al., 2013, A&A559, A54
- Wagner R., , Beach Cities Robotics
- Webbink R.F., 1984, ApJ277, 355
- Zhang Y.Y., Deng L.C., Liu C., et al., 2013, AJ146, 34

Acknowledgements

There are many people without whom this work would not have been possible.

First of all, I would like to thank my supervisor Ulrich Heber who was always there and open for any question or need from my side. He gave me the opportunity to work on a project adapted to my personal interests throughout the last years and I appreciate the freedom and independence during work and the opportunity to participate in international conferences.

Furthermore, I would like to thank Andreas Irrgang for the hours of discussion and advices. My sincere thanks also go to Peter Németh who provided me with tips and supported me wherever he could. Also, Eva Ziegerer was always there to answer spontaneous questions of any type.

The whole stellar crew at the observatory participated in discussions to tackle problems during the development of the code. Amongst them and previously not mentioned Christian Heuser, Marilyn Latour, and Markus Schindewolf.

Thanks also to all the others who contributed to the good atmosphere at the observatory. It is a lovely place to work and with the good climate in the office and at the entire observatory it was much easier to gather new creativity.

Furthermore, I would like to thank my friends and family for their support.

This masterthesis contains observations made with the Mercator Telescope, operated on the island of La Palma by the Flemish Community, at the Spanish Observatorio del Roque de los Muchachos of the Instituto de Astrofísica de Canarias.

This masterthesis contains observations obtained with the HERMES spectrograph, which is supported by the Research Foundation - Flanders (FWO), Belgium, the Research Council of KU Leuven, Belgium, the Fonds National de la Recherche Scientifique (F.R.S.-FNRS), Belgium, the Royal Observatory of Belgium, the Observatoire de Genève, Switzerland and the Thüringer Landessternwarte Tautenburg, Germany.

Erklärung

Hiermit erkläre ich, diese Masterarbeit in Eigenarbeit angefertigt zu haben, sofern nicht explizit in Text oder Referenzen vermerkt. Diese Arbeit ist der Universität Erlangen-Nürnberg als Voraussetzung für den Erhalt des Abschlusses *Master of Science* vorgelegt worden. Ich erkläre, dass diese Arbeit weder partiell noch als Ganzes für den Erhalt eines anderweitigen Abschlusses verwendet wurde und wird.

Erlangen,
Ort, Datum

Simon Kreuzer